Electronic Thesis and Dissertation Repository

10-9-2019 2:00 PM

A Framework for Evaluating Cortical Architectural Anomalies in Temporal Lobe Epilepsy Patients

Hossein Rajali
The University of Western Ontario

Supervisor
Khan, Ali
The University of Western Ontario

Graduate Program in Biomedical Engineering
A thesis submitted in partial fulfillment of the requirements for the degree in Master of Engineering Science
© Hossein Rajali 2019

Abstract

Focal cortical dysplasia (FCD) are localized regions of malformed cerebral cortex that are frequently associated with drug-resistant epilepsy. Currently, there is a lack of research towards providing quantitative methods for characterizing minor abnormalities in cortical architecture, hindering efforts to determine whether removal affects surgical outcome, and define potential imaging correlates. In our work, we have developed a tool to extract relevant features associated with cortical architectural abnormalities that can deal with artifacts including cortical layer distortions and morphological differences caused by cortical folding effects, and processing artifacts due to improper sectioning. This framework was applied to detect abnormalities across multiple subjects and slides using unsupervised anomaly detection algorithm. Our results suggest that the technique is able to identify anomalies that correspond to visually-identifiable histological abnormalities. The frequency of abnormalities was found to differ among patients; however, the clinical significance of these findings is yet to be investigated.

Lay Summary

Drug-resistant epilepsy occurs in over 30% of epilepsy patients, with many patients undergoing surgical treatment to alleviate their seizure activity. Focal cortical dysplasia (FCD) is a common pathology associated with drug-resistant epilepsy and is mainly characterized by the presence of abnormal brain layering. However, FCD is challenging to diagnose and treat since lesions are not often seen with clinical imaging protocols. Furthermore, minor cortical architectural abnormalities are seen in many temporal lobe epilepsy cases, however, their significance is not well understood because of the challenges in objectively quantifying these abnormalities. The goal of this research is to develop analysis tools for histopathology of resected brain tissue to objectively and quantitatively evaluate cortical abnormalities in epilepsy patients. Quantitative evaluation of cortical architecture in histology samples would complement specialists in the detection of subtle epileptogenic lesions, reducing inter-rater variability and ultimately providing a more accurate reference for in-vivo diagnostic techniques.

A major challenge in analyzing cortical histology to quantitatively describe cortical architecture is that the layering of the brain can be distorted in different parts of the sample. This is caused by mainly two sources of variability: displacement of the brain layering due to the complex geometry of the brain, and out-of-plane sampling problems when the section is not perpendicular to the brain surface. These alterations can cause issues for computer-aided analysis, as many algorithms have difficulty in handling these artifacts.

In this study, we summarize our digitized tissue samples into relevant features that describe the cortical architecture. The result of the summarized features showed sensitivity to changes commonly associated with FCD pathology. Additionally, we implemented a method to extract relevant layering information computationally and applied computational techniques to align the displaced data across multiple slides and subjects. Furthermore, we apply a machine learning technique to identify and eliminate the processing artifacts presented in the data due to out-of-plane sampling problems. We then applied an outlier detection algorithm to test whether outliers in the data represent abnormal tissue in the brain. Our results suggest that anomalies

in the summarized image features resemble abnormalities in the tissue samples.

Whenever there is a will there's a way.

Acknowledgments

It is imperative first to acknowledge the person that made this all possible, Dr. Ali Khan. Thank you for your guidance, mentorship and inspiration throughout my time here at Western! Ali, thank you for your open-door policy, I've pushed the limits of "no question is a bad question" during our meetings. Your wisdom and technical expertise were essential components for my professional development and completion of my thesis. You have shown me the qualities of a great leader. I will aim to emulate your focus and drive, creativity, empathy, and your attention to detail in my future endeavours.

To my advisory committee: Dr. Ingrid Johnsrude, and Dr. Lena Palaniyappan, I would like to acknowledge your guidance and advice throughout the last two years.

To Jordan Dekraker, I cannot thank you enough for your keen interest and leadership in my research. Jordan, you have been a great role model, and I have learned so much from you! I am so grateful that both our research interests crossed while in graduate school, and I will cherish the stories we shared at the grad club and our talks about cutting edge AI/hippocampal research. Thank you for helping me strive for greatness, during my time at Western, you've given me advice that I will cherish forever. To Uzair Hussian, I cannot thank you enough for the mentorship and friendship throughout my time here at Western. I am grateful for your guidance and will miss our "start-up" and our "side-hustle" discussions. You were a friend since day one, and I am very thankful! To Jason Kai, my "Mac homie," thank you for showing me hard work pays off, your work ethic and the perseverance you display are inspiring. Your advice, friendship and support was invaluable! To Dimuthu Hemachandra, you've kept my Facebook newsfeed updated with the latest memes, thank you. I will cherish our trips to Tim-Hortons, which was probably 3-4 times a day. You were always there to provide sound advice and offered endless support, wisdom, perspective, and coffee - thank you. To G.O.F (Roy Hasst), your intricate figure making is inspiring, thank you. You have taught me the qualities required to be a great defensive soccer player which involved eliminating the competition, I will miss losing games with you. To Loxlan, you've been there to provide sound advice and

support, your wisdom of life will be cherished. To Tristan Kuhn, you have taught me it is possible to stay focus for the complete 9 hours of the working day, your focus and hard work are motivating. Our time fixing the 3D printer will not be forgotten. To Sudesna Chakraborty, you have taught me to go outside my comfort zone and buy coffee from Starbucks, I will cherish our discussion to and from the UCC. A special thank you to the Khan and VASST lab - past and present - I feel fortunate to call each of you, my colleague and friend.

To the "Doctor of Gains" - T.D., and Gabriel, we have kept each other honest motivated and resilient during our time at Western. I "hugely" appreciate knowing you were always there whenever I needed a "spot" and were always vehemently in my corner to support my "sets". Without the "Doctor of Gains," there would be no gains only loses.

To Quincy Izabela Sofowara, I cannot thank you enough for the unconditional love, tremendous support and inspiration to follow my dreams. Quincy, you have continuously offered a listening ear during times of difficulty and managed to provide endless support and encouragement to push me closer towards my goals. I am extremely thankful for having my "partner in crime" by my side throughout this journey!

Finally, my deepest gratitude goes towards my family and friends outside of Western. Despite being too busy at times, you have supported and encouraged me, provided me with love and friendship whenever we reconnect. The help, support and encouragement you have provided goes beyond my time here at Western, Thank you!

Contents

List of Figures

List of Tables

List of Abbreviations, Symbols, and Nomenclature

Terminology

AED	Anti-Epileptic Medication
ATL	Anterior temporal lobectomy
CAD	Computer Assisted Diagnosis
CSF	Cerebralspinal fluid
CWM	Cortex-White Matter
FCD	Focal Cortical Dysplasia
GM	Grey Matter
ILAE	International League Against Epilepsy
MCD	Malformation of Cortical Development
ML	Machine Learning
mTLE	Mesial Temporal Lobe Epilepsy
PCA	Principal Component Analysis
WM	White Matter
SAH	Selective amygdalohippocampetomy
SVM	Support Vector Machine
TLE	Temporal Lobe Epilepsy

Medical Imaging Terminology

CT	Computed Tomography
EEG	Electroencephalogram
MRI	Magnetic Resonance Imaging
PET	positron emission tomography
SPECT	single photon emission computerized tomography

Chapter 1

Introduction

1.1 Epilepsy

1.1.1 Introduction to Epilepsy

Epilepsy is a neurological disease characterized by abnormal neuronal electrical activity which is associated with recurrent seizures [1, 2]. Specifically, a seizure is defined as a sudden, uncontrolled electrical disturbance in the brain. A diagnosis of epilepsy is often recognized when a patient has two or more unprovoked seizures episodes. Seizures are caused by an imbalance of inhibitory and excitatory neural signalling, causing excessive neuronal electrical activity in a confined or general region of the brain. There is a wide range of types of seizures, and the manifestations will depend on the particular type of seizure disorder. The International League Against Epilepsy (ILAE) classification has categorized seizures into two groups, partial (focal) seizures and generalized seizures [3, 2]. Focal seizures are seizures that consistently arise from a confined localized region in the brain, resulting in a specific uncontrolled action, with or without loss of or alteration in consciousness. Focal seizures are further characterized by whether awareness is retained (focal aware) or impaired (focal impaired awareness). In addition, the presence of motor movements during the onset of seizure can further characterize the focal seizures. Generalized seizures affect both hemispheres often from the onset of a

seizure, and are sub-categorized by the presence of convulsive movements. Epilepsy is one of the most common neurological disorders affecting 1% of Canadians and more than 65 million people worldwide. [4, 5]. The highest number of newly diagnosed cases are found in seniors and young children, but the disease can begin at any age.

The first line of treatment for newly diagnosed patients are anti-epileptic drugs (AEDs). However, the ability to control and eliminate seizures remains highly limited. In approximately 30 percent of cases, patients have intractable epilepsy as they are drug-resistant to medication despite multiple trials of AEDs [6, 7]. A prognosis of epilepsy, especially those with drug-resistant epilepsy, is associated with a decrease in quality of life due to high levels of social stigmatization and imposed restrictions [8], increase risk in suicide [9], as well as an increase in psychiatric co-morbidity [10], and decrease in life expectancy [11]. This devastating neurological disease places a huge burden on patients, family and friends, as well as the health care services due to the additional costs and need for more complicated interventions such as surgery in drug-resistant cases [12, 13].

Temporal lobe epilepsies (TLE) represent the most common form of focal epilepsy and are among the most frequent medically intractable [14]. Temporal lobe epilepsy is defined as epilepsies in which seizures originate from mesial or lateral structures of the temporal lobe. Surgery may have a role in the treatment of both mesial and lateral temporal lobe epilepsies in drug-resistant patients [14]. When there is a localized seizure focus, found through clinical imaging, patients become eligible for surgical excision of the affected brain region in order to achieve seizure control [15, 16]. In the case of temporal lobe epilepsy, an anterior temporal lobectomy is an effective treatment, resulting in seizure freedom for 60-80 percent of patients [17, 18, 19]. A major factor in surgical success is correct identification and resection of the entire seizure focus, which is challenging in subtle cases due to the limitations in clinical neuroimaging [20].

1.1.2 Temporal Lobe Anatomy and Function

The temporal lobe is one of the four lobes of the brain among the frontal (blue), parietal (yellow) and the occipital lobe (red), and lies at the base of the skull beneath the lateral sulcus or Sylvian fissure as shown in Figure 1.1.
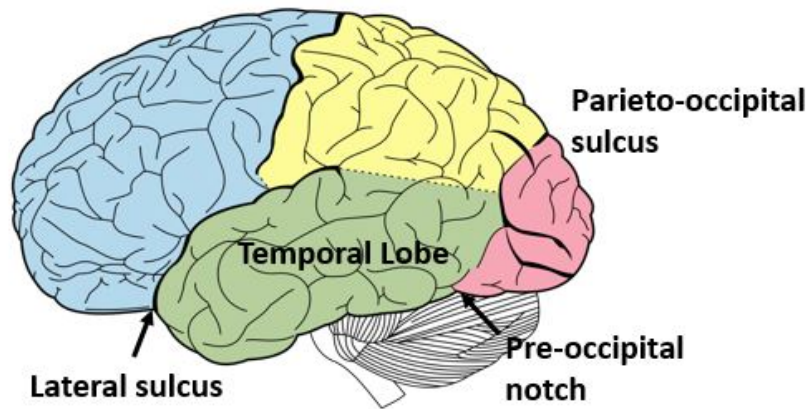
Figure 1.1: Location of temporal lobe within the cerebral cortex and anatomical landmarks defining temporal lobe boundaries. Modied from Henry Grays anatomy: Figure 728. Licensed under Public domain via Wikimedia Commons

The lateral component of the temporal lobe comprises of the temporal neocortex which is responsible for speech perception and language comprehension, as well as auditory, visual and olfactory senses [21]. The mesial temporal lobe structures involve the limbic structures which consist of the hippocampus and other nearby deep structures. The hippocampus receives highly processed sensory information from disparate regions of the brain and is responsible for consolidating working memory into long-term declarative memory (facts and experiences) [21]. Furthermore, the hippocampus is involved in many other aspects of cognition beyond navigation and declarative memory, including for example emotional regulation [22], imagining the future [23], and perceptual processing [24]. Figure 1.2 highlights the deep structures found within the medial temporal lobe.
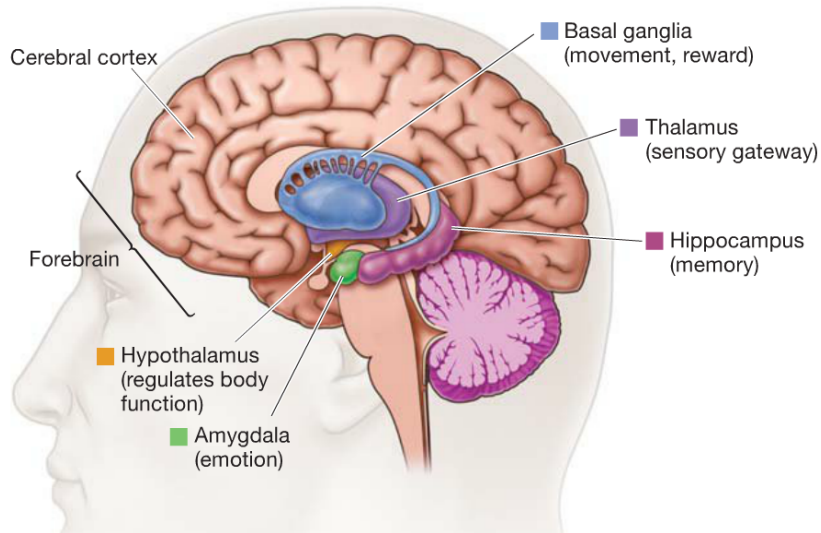
Figure 1.2: Deep brain structures and high level function

1.1.3 Neocortical Architecture

The cerebral cortex is the convoluted outer surface of the cerebrum and is composed of grey matter. The grey matter is made up of neurons and other neuronal cells, which are the basic functional units of the nervous system (Figure 1.3). These cells are responsible for receiving and transmitting information through electrical signals. Neurons are typically composed of three parts: dendrites, the soma or cell body, and axon. Respectively, the three components of the neuron allow these cells to receive signals from other neurons, integrate incoming signals, and transmit or communicate signals to target cells, such as other neurons. The other types of cell types found within the cortex are glial cells which function primarily to support neurons.

The cortical grey matter is arranged in layers, or laminae, with each layer having distinct densities and types of neurons. The neuronal cell bodies found within each layer may also differ in size and shape. For example, layers II and IV have high density with mostly smaller granular neurons, and layer III and V have a lower density with mostly larger pyramidal neurons. Brodmann, a German scientist in the early 20th century, was the first to describe that the properties of the layers differed from one cortical region to another. Individual layers exhibit distinct cellular compositions and distributions [25], developmental trajectories [26], and functional roles [27]. The six cortical layers are numbered from the pial (outer surface) to the white
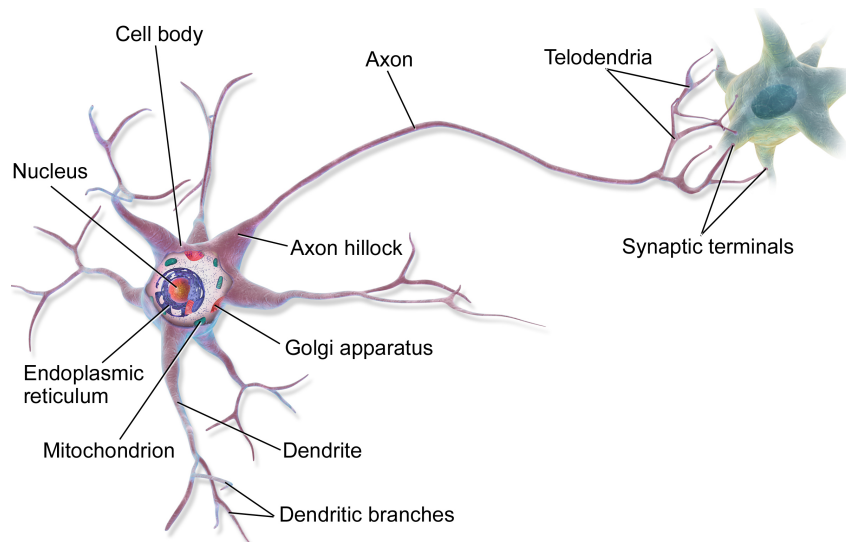
Figure 1.3: Diagram of a neuron. Adapted from the Blausen Gallery, 2013. Licensed under the Creative Commons Attribution 3.0 Unported license

matter (inner surface), as seen in Figure 1.4. Overall, the 2-3 mm thick cortex consists of the following 6 layers: Layer I, or the molecular layer, which is sparsely populated by neuronal cell bodies; Layer II, the external granular layer, a relatively thin layer which consist of numerous small, densely packed neurons; Layer III, the external pyramidal layer, which is composed of mid-sized pyramidal nerve cells; Layer IV, also known as the internal granular layer, that is composed of densely populated granular cells, and is the most densely packed layer; Layer V, also known as the internal pyramidal layer, includes large pyramidal neurons; and layer VI, the polymorphic layer or multiform layer, this layer contains a mix of small polymorphic and fusiform neurons [28, 29].

As mentioned previously, the cortical layers have specific functional roles, as reflected by the inputs they receive (afferents), and the sites to which they project their axons (efferents). In general, layers I, II, and IV are primarily input layers, that receive their inputs from the thalamus and other regions of the cortex. Whereas, layers III and V contain mostly efferent fibres that project signals to the brain stem, spinal cord and other cortical regions. Layer VI has mostly efferent fibres that project to the thalamus. The disruption of the cortical architecture or the structure of the cortex can affect the functional activities of the layers, which can give rise to epilepsy and other functional pathologies [3, 30, 31].
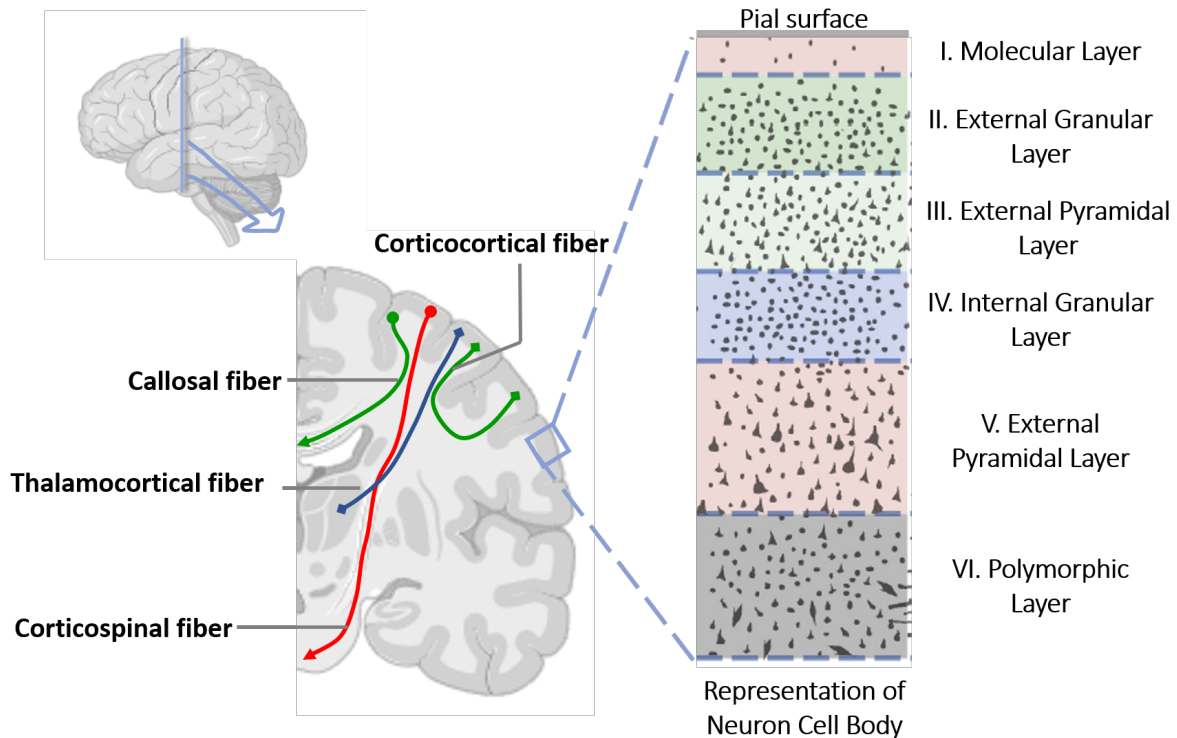
Figure 1.4: Coronal section through the cortex showing the major types of fibers projecting to and from the cerebral cortex. Illustration on the right shows the six cortical layers as they appear after staining for cell bodies. Image created with ©BioRender - biorender.com

1.1.4   Neuropathology of Temporal Lobe Epilepsy

Pathological findings in surgical resections from patients with temporal lobe epilepsy include a wide range of diagnostic possibilities, which can originate from either genetic or acquired factors. These include conditions such as hippocampal sclerosis, congenital lesions, tumours, ischemic lesions, traumatic injuries, and inflammatory lesions [32]. Many of these pathological findings are complex and challenging to assess due to the presence of multiple types of lesions and the historical lack of quantitative characterization. In addition, there is an ongoing debate about whether the presence of dual pathologies (i.e., hippocampus sclerosis and associated microscopic cortical architectural abnormalities) is a significant factor for surgical outcome. With early studies stating the presence of hippocampus sclerosis and associated microscopic abnormalities leads to a higher risk of seizure recurrence [33, 34], while newer studies suggest that patients have a favourable outcome when both pathologies are removed [35, 36, 37]. The

lack of research towards characterizing minor abnormalities in cortical architecture hinders the ability to determine whether removal of the minor architectural abnormalities affects surgical outcomes. Better classification of the range of such pathologies can lead to improved detection of lesions which can be used to assess surgical predictive outcomes and improve in-vivo characterization. Therefore in this work, we will focus on providing a quantitative method for characterizing lesional epilepsy due to malformations of cortical development.

Malformation of Cortical Development

Cortical development (corticogenesis) is the dynamic process in which the cerebral cortex is formed through a series of complex morphogenetic events [38]. Corticogenesis starts with the development and growth of the nervous system and is followed by the proliferation of neurons. Neuronal cells will then undergo migration towards their final locations in one of the six layers of the cortex. Finally, the neurons will take on specific functional roles during the differentiation stage. Malformations of cortical development (MCD) are brain abnormalities resulting from the disruption in the normal processes in cortical development. Typically the disruptions occur in stages during neurogenesis and migration. The disruption of cortical development can result in abnormal cortical structure and neuronal morphologies. Ultimately this may disrupt neuronal circuitry and predispose patients to a variety of clinical consequences, epilepsy being the most common outcome [38].

Focal Cortical Dysplasia

Focal cortical dysplasia (FCD) is a common form of MCD and is the leading cause of drug-resistant epilepsy in both children and adults [39]. FCD was first termed by Taylor et al. (1971) to describe localized regions of malformed cerebral cortex in surgical specimens from patients with epilepsy. Since then, FCD has been defined as a range of cortical abnormalities each with specific histopathological features [40]. As a result, the ILAE has created a three-tier classification system to distinguish the range of FCD variants [41, 3]. The broad range of FCD variants

includes a wide range of characteristic deformities including disrupted cortical architecture, cortical lamination, radial organization, and presence of abnormal neuronal morphology.

According to the ILAE three-tier classification system, FCD type I are isolated lesions presented with abnormal cortical layering or lamination. FCD type Ia variant are lesions with radial disorganization characterized by the presence of microcolumns, defined in regions containing more than eight neurons aligned in the vertical direction. FCD type Ib consist of loss of the six-layered tangential architecture of the cortex, resulting in blurring between boundaries of the layers. Furthermore, FCD type Ic is abnormalities consisting of both abnormal radial (FCD type Ia) and tangential cortical lamination (FCD type Ib). FCD type II variant are isolated lesions characterized by the presence of cortical dyslamination in addition to dysmorphic neurons without (Type IIa) or with the presence of balloon cells (Type IIb). The hallmark feature that differentiates FCD type II variant from the other variants is the presence of dysmorphic neurons, defined as neurons with: significantly larger cell bodies, malorientations, and abnormal presence of Nissl substance and neurofilament proteins. FCD Type III refers to cortical lamination abnormalities in addition to the presence of a principal lesion. These include lesions that are associated with: hippocampal sclerosis (FCD Type IIIa), tumours (FCD Type IIIb), vascular deformations (FCD Type IIIc), and lesions acquired during early life (FCD Type IIId).

Currently, there is a lack of research towards providing objective, quantitative methods for characterizing FCD in epilepsy. Since specimens with FCD present a higher degree of complexity, there is a need for quantitative methods that can differentiate between the FCD variants and objectively apply the ILAE classification scheme. In addition, such quantitative methods can be incorporated into the ILAE classification scheme in order to increase the sensitivity and specificity in routine microscopic diagnosis. In a previous study by Muhlebner and colleagues, specific morphological features were evaluated and highlighted for FCD subgroups to improve the lack of quantitative measurements in the proposed ILAE criteria [42]. In particular, Muhlebner and associates evaluated cortical thickness, neuronal cell densities, and size and

highlighted relative changes in these parameters in the different FCD subgroups compared to age and location-matched controls. Although their work highlights relevant parameters for the detection of FCD variants, further work is needed to provide an automated method capable of characterizing and analyzing whole sections of cortical tissue.

1.1.5 Diagnostic techniques for Pre-Surgical Planning in Epilepsy

Surgery can have tremendous outcomes for TLE patients providing seizure freedom to 60-80 percent of eligible drug-resistant patients [17, 18, 19]. However, potential candidates with drug-resistant epilepsy that consider surgery must undergo an extensive evaluation to determine that the surgical procedure will be an effective treatment in controlling seizures without unacceptable adverse side effects [16, 15]. In order to properly evaluate patients, details of the medical history, blood tests, neuropsychological test, EEG tests, nuclear imaging and brain imaging scans such as PET and MRI are often needed. This provides clinicians with information about the electrical activity of the brain, what the brain looks like and possible causes of seizures. Therefore, diagnostic and pre-surgical evaluation is a crucial first step in determining eligibility and accurate planning of surgical intervention.

EEG Role in Pre-Surgical Planning

Electroencephalography (EEG) is a technique used for measuring neuronal electrical activity in the brain using electrodes attached to the scalp. In general, neurons are excitable cells which generate time-varying electrical currents when activated. EEG detects the voltage fluctuations from ionic currents in the activated neurons. Although, EEG is incapable of recording electrical activity from individual neurons, since neurons are microscopic, and their signal is very faint the recording is still possible since the recorded signal is from the summed activity of many neurons firing in synchrony [43, 44]. The signal from this modality is known to have a high temporal resolution (on the order of milliseconds), making, EEG a vital non-invasive tool for analyzing the temporal dynamics of the brain [45]. EEG is commonly analyzed as

temporal waveforms over multiple channels and is evaluated based on the power of rhythms, frequency changes, latency and amplitude fluctuations of the peaks and troughs during a stimulus or event [46]. In particular, the onset of clinical seizure activity can be characterized by a sudden change of frequency, sudden loss or increase in voltage, or presence of ultra-low or ultra-high frequencies [47]. The primary purposes of EEG recordings in epilepsy are to confirm the presence of a seizure, the type of seizure, location, and whether seizures are focal or generalized. These findings can help determine a clinical course of action, including specifying the type of AEDs and determining whether the patient is a candidate for surgery. Other neuroimaging modalities, such as MRI, potentially help to identify the extent and exact location of the seizure focus. The main limitation of EEG is its poor spatial resolution (centimetres) and that this modality does not provide a direct method of localizing the exact location of seizure focus [46]. In addition, EEG is limited to measuring electrical activity near the surface of the scalp and does not provide information from deeper structures of the brain.

Another method for evaluating the neuronal activity for pre-surgical evaluation is intracranial EEG (iEEG). The techniques involved include surgical insertion of subdural electrodes in suspected cortical regions and/or insertion of depth electrodes to evaluate deeper brain structures. Compared to standard EEG modality iEEG can provide additional electrographic evidence for seizure localization, as electrodes are placed closer to the suspected region of interest. The implantation of subdural or deep electrodes is indicated when a patient is being considered for surgery, and the readings of scalp EEG have been inconclusive. Although iEEG methods are relatively safe, they must be balanced against the potential surgical complications such as hematoma, infection, malignant cerebral edema, and brain compression from intracranial electrodes [48, 49]. When consistent findings from the analysis of MRI, EEG, and neuropsychology provide conclusive evidence of lesion focus, surgery is performed without intracranial EEG [49].

Neuroimaging Role in Pre-Surgical Planning

In order to properly evaluate patients, imaging modalities such as magnetic resonance imaging (MRI), Computerized tomography (CT), positron emission tomography (PET), and single-photon emission computerized tomography (SPECT) scans may be potentially required for the pre-operative planning of epilepsy surgery. Among the variety of imaging modalities used magnetic resonance imaging has proven to be the most clinically useful in the diagnostic process in lesional epilepsy, leading to a greater understanding of structural abnormalities found within patients and increased surgical success [50].

Nuclear magnetic resonance (NMR), now referred to as MRI, was first introduced in 1946 [51, 52], at the time the medical value was not realized until in-vitro rat tumours showed different NMR characteristics in 1971 [53, 54]. MR imaging is now one of the most common non-invasive imaging modalities for visualizing anatomical structural details, especially in neurology. The fundamental principle behind MRI is based on the magnetic properties of atomic nuclei, which are exploited through strong magnetic fields in addition to radio frequencies to generate images that are not only anatomical but also reflect physiological status [54]. The main advantages MRI provides compared to other imaging modalities, such as CT, is that MR provides high contrast between tissue types, especially in the brain. Furthermore, the tissue contrast in MRI can be exaggerated to highlight specific structures, such as tumours or lesions, by modulating the method of acquiring the MR image, specifically the pulse sequence used to generate these images. This makes MRI techniques very useful compared to other imaging modalities such as CT which provides very little contrast between tissue types in the brain. Secondly, MRI is a non-invasive technique that provides the highest spatial resolution among other methods such as PET and SPECT, whose spatial resolution is lacking and is invasive due to their exposure to ionizing radiation. Details about other imaging modalities used for diagnostics of epilepsy such as CT, PET, SPECT, and others are outside of the scope of this project but have a valuable contribution in both diagnostics and pre-operative planning.

MRI has revolutionized the pre-operative evaluation of drug-resistant epilepsy by allowing

reliable detection of lesions related to seizure onset, leading to increased rates of surgical success. In fact, several studies have shown that a reliable predictor for favourable post-surgical outcome is the complete resection of seizure focus as detected by MRI [55, 56, 57, 58, 59]. Despite MRI ability to often accurately identify lesions related to seizure onset, in more than 30% of patient lesions are undetected based on clinical imaging protocols [60, 61] with histological evaluation revealing subtle lesions or dual pathologies undetected by MRI - mainly dysplasias and rarely subtle isolated gliosis [62, 63]. Sensitivity can be increased by the use of dedicated acquisition protocols such as quantitative MRI sequences and image processing techniques, such as T2 relaxometry mapping, diffusion tensor imaging (DTI), and voxel-based morphometry which can provide correlation with neocortical pathology that is absent with clinical MRI [64]. For example, Cantor-Rivera et al. [65] showed that with the use of quantitative multi-parametric imaging the identification of TLE patients can be improved from 81% to 88.9%. In addition, with the advancement in artificial intelligence and machine learning, detection of structural abnormalities in epilepsy has become increasingly sensitive. Dev et al. [66] utilized MR imaging and convolutional neural networks, a form of deep learning, to detect FCD lesions. In their study, they were able to obtain an 82.5% detection rate in their proposed model. The continued development of new imaging modalities and computational techniques aimed at better identifying the lesional epilepsies will enable surgical treatment and improved outcomes in an increasing number of patients. The advent of higher-field magnets at ($\geq$ 3T) has improved the obtainable resolutions and image quality (i.e. signal-to-noise and contrast-to-noise). Such advancement in high-resolution MRI has made it possible to identify increasing numbers of patients with lesional epilepsy, as there is evidence that structural abnormalities extend beyond obtainable resolution in standard clinical MR protocol at 1.5T [67, 68, 69]. However, with the new advances in MRI technology, imaging modalities, and computational techniques, there is an increasing need to evaluate performance with ground truth annotations. Histology can provide accurate ground truth information to test the validity of the MRI techniques in identifying disease-related tissue alterations, such as epilepsy and other neurological disorders [70].

1.1.6   Epilepsy Surgery

Even with the continuous improvements to pharmacotherapy with the introduction of new anti-epileptic medications, the problem of medically refractory epilepsy has not yet been solved [71, 72]. Currently, surgery is the standard of care in the majority of drug-resistant focal epilepsy cases. In a randomized controlled trial, it was shown that surgery is a superior treatment compared to prolonged medical therapy [73]. Ultimately, surgery has proven to be an effective treatment option for drug-resistant patients providing $60 - 80 \%$ success rate in which surgically treated patients become seizure-free [17, 18, 19]. Temporal lobe resections are a relatively safe medical procedure with almost zero mortality rate, and with the continuous advances in pre-surgical assessment and a broad range of available surgical techniques, these procedures are becoming even safer and more efficient [74, 75]. There are two standard surgical procedures used in the treatment of drug-resistant TLE (Figure 1.5), anterior temporal lobectomy (ATL) and selective amygdalohippocampetomy (SAH).
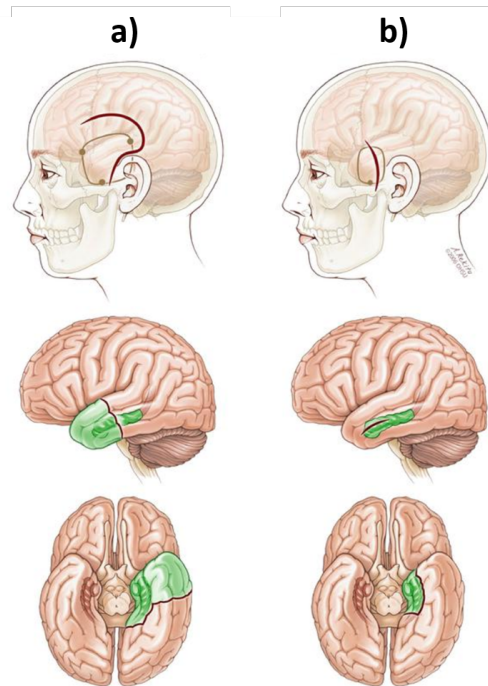
Figure 1.5: The standard temporal lobe surgeries showing the performed craniotomy (first row), and the target tissue (second and third row). **a)** anterior temporal lobectomy (ATL) **b)** selective amydalohippocampectomy (SAH). Adapted from the creative commons attribution license from epilepsy research and treatment 2012, Selective Amygdalohippocampectomy, Spencer D. and Burchiel k., © 2012.

The former, ATL, is the most common surgical approach in treating adolescents and adults with medically intractable TLE [76, 77]. The procedure involves complete resection, or equivalently 3.0-5.0 cm, of the anterior portion of the temporal lobe including the mesial structures, the hippocampus and amygdala. In lesional epilepsy, preservation of the mesial structures may be indicated in cases with discrete temporal lesions without indication of mesial involvement. In contrast, during SAH, the amygdala and hippocampus are removed while preserving the surrounding neocortex.

Although complications are uncommon, there are still risks associated with temporal resective surgery. These risks can be broken down into three groups: surgical, neurological and psychological complications [74]. Among the three, a surgical complication such as infections, postoperative stroke, and cerebral spinal fluid leakage are the most common complications. Neurological complications include visual field deficits on the contralateral side of surgery, cranial ischemic changes, and cranial nerve paresis or palsy. In addition, common cognitive or physiological complications include both verbal and visual memory loss, speech difficulties, emotional changes, as well as the development of depression and anxiety disorders [74]. Accurate pre-operative planning is a critical step for both preventing surgical complications and surgical success.

Surgical success remains sub-optimal, despite the current advanced imaging techniques used to localize epileptic lesions. Poor surgical outcomes, which is defined as early seizure recurrence, are suspected to be mainly due to inadequate removal of epileptic lesions, due to the inability to clearly identify lesions pre-operatively. In fact, studies have shown that a reliable predictor in surgical success is the accurate localization of epileptic lesions as detected in MRI prior to surgery [55]. In another study, surgical removal of focal dysplasia lesion resulted in 92% seizure freedom, when resection was complete according to MRI [49]. However, a significant challenge in epilepsy surgery is the development of novel techniques that are capable of localizing the epileptogenic focus, especially in subtle cases in which current MRI is unable to detect structural abnormalities (MRI Negative). In order to develop new in-vivo techniques for

detecting epileptic abnormalities in epilepsy, it is required that these techniques be thoroughly validated by correlating with histology of excised tissue following surgery.

1.2   Histopathology

Histopathology is the microscopic examination of diseased tissue. Histopathology refers to the examination of a biopsy or a resected specimen by a pathologist. Pathological findings in surgical resections from patients with TLE include a wide range of diagnostic possibilities, some of which defy specific diagnosis [78]. The careful examination of resected tissue from TLE patients can enhance our understanding of the underlying pathology of TLE and ultimately lead to better management and diagnostic strategies [32]. Quantification and characterization of specimens can aid in the detection of the wide range of pathologies in TLE with higher sensitivity and can provide a quantitative measure of lesion severity.

1.2.1   Tissue Preparation

Microscopic analysis of tissue requires the correct preparation of very thin, high quality sections, or slices, that are appropriately stained to demonstrate normal and abnormal structures of interest. In the following sections, the necessary preparations required before examinations are outline in detail, which can be summarized in the following steps:

1. Fixation
2. Wax Infiltration and Embedding
3. Sectioning
4. Staining

Fixation

Fresh tissue is very delicate and can be easily distorted and damaged. Preserving and stabilizing tissue, by fixation is a critical step in the preparation of biological tissue before other

processing occurs. Tissue fixation is the process of chemically preserving biological tissue from natural decay in addition to maintaining cell and other tissue structure throughout preparation steps. The standard fixation process involves placing tissue in a liquid fixative, such as formaldehyde This will slowly penetrate tissue causing chemical and physical changes that harden and preserve the tissue and protect it from subsequent processing steps. The liquid fixative, usually formalin, is carefully balanced and buffered in order to reduce shrinkage, swelling, and other unwanted artifacts.

Wax Infiltration and Embedding

After the specimen is fixed and dehydrated, it is required to be embedded in a material that has appropriate physical properties which will solidify and allow thin slices or sections to be cut from the specimen. Paraffin wax is the most common wax infiltration and embedding material for this process. Once the wax infiltration process is completed, the specimens are enclosed in a block mould and are moulded using the paraffin wax. Note that the specimens are carefully oriented into a block mould as the orientation will determine the plane of section, an important consideration in both diagnostic and research histology.

Sectioning

Once the specimens are embedded, the paraffin blocks are sectioned in thinly sliced sections. The microtome is an apparatus used to section the tissue embedded paraffin blocks with micron level precision. There are a number of factors that affect the quality of section such as: blade material, blade shape, cutting speed, blade angle, and others. Sections cut under non-optimal conditions will result in a number of artifacts such as tearing, out of plane section, folding. The sectioned slices are then mounted onto a microscope slide.

Staining

Prior to staining, tissue structures may be colorless or transparent, the staining process provides enhanced contrast to tissue structures of interest. There are various types of stains, each are specialized to highlight certain tissue structures with the presence of a specific reactive compound. For instance, stains may be used to define and examine bulk tissue such as muscle fibers, cell populations, or organelles within cells [79]. For example, the NeuN antibody stain reacts with neuronal proteins, a compound found in abundant in the nuclei and cytoplasm of most neurons in the nervous system, thus enhancing contrast between the neuronal cell bodies and other tissue structures.

Digitization

Upon completion of staining tissue structures, the 2D slides are evaluated by a pathologist to provide an appropriate diagnosis. Typically, the pathological report will be made by the pathologist directly using the stained slides and light microscope, however, it is becoming common practice to convert slides to a digitized form where it can be visualized, stored, and evaluated digitally. Digitize slides, or digital pathology can improve accessibility, allows teleconsultations from specialized pathologists, and provides an accessible method for sharing slides for research purposes. With digitized slides, it is possible to develop computer-aided diagnosis (CAD) systems, such that pathologist can be guided to regions of interest based on objective quantitative criteria, potentially increasing sensitivity and reducing workload and inter-observer variation [80]. As such, digital pathology has the potential to improve the exchange between pathologists and research colleagues, which can lead to better treatment options or interventions for patients.

1.2.2 Image Artifacts

Ideally, tissue preparation preserves the natural structure and morphology that closely represents the tissue in-vivo. However, during the tissue preparation process there may be an unwanted presence of foreign substances or alteration in tissue details which can result in confusion and lead to incorrect interpretations [81]. These changes are broadly referred to as artifacts. Artifacts in histological sections can result from any of the steps in the tissue processing pipeline, and therefore are difficult to avoid. Common artifacts encountered include tissue shrinkage due to prolonged fixation, tissue tearing due to sub-optimal handling, and color inconsistencies from improper staining. Figure 1.6 illustrates examples of common artifacts encountered in histopathology. The presence of artifacts can result in clinical misinterpretations leading to poor diagnostic accuracy [81]. In addition, certain artifacts can cause issues for computer-aided analysis, as many modern algorithms have difficulty handling these artifacts. Thus artifacts must be considered and potentially corrected for before analysis can be done.

Tissue folding   **Tissue tearing**   **Obliquely section region**

NeuN stain color inconsistency.
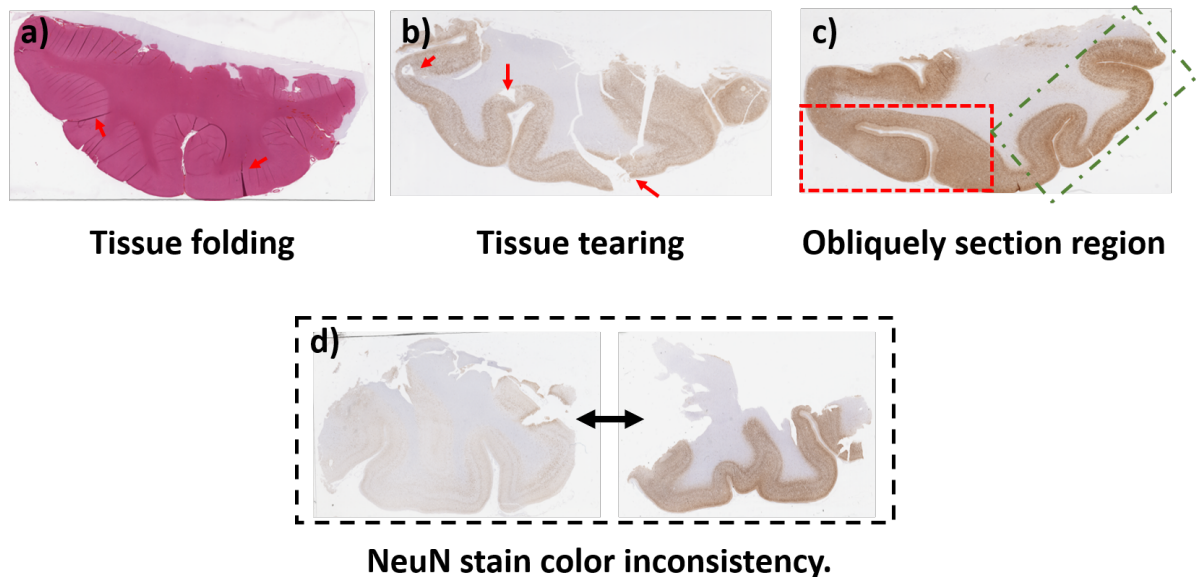
Figure 1.6: Common examples of histopathology artifacts. **a)** tissue folding artifact due to improper slide mounting **b)** Tissue tearing due to poor slicing or tissue handling. **c)** obliquely sliced region (red) compared to ideal sectioning (green) due to poor slicing. **d)** color inconsistencies from improper staining.

1.3   Techniques for Cortical Laminae Modeling

Irregularities in microstructure in the different layers of the cortex are seen in several neuro-logical disorders. For example, malformations of cortical development can lead to focal areas of abnormal neuronal architecture, which can result in epilepsy, and, in some instances mental retardation [82, 83]. Furthermore, evidence from previous research suggests that neurological disorders such as major depressive disorder (MDD) [31], and schizophrenia [84] are associated with abnormalities in intracortical myelin content. The irregularities in the cortical architecture are often associated with deformities in cortical cytoarchitecture. However, to analyze layer architecture or function, it is desirable to define a suitable coordinate system which allows sampling of cortical laminae. In this section, we introduce and evaluate the different techniques and models used to analyze and sample the cortical laminae, often referred to as cortical laminae models. These models can be represented as a three-dimensional coordinate system, where each point represents the image intensity at a specified depth along the cortex (i) and location along the cortical ribbon (j). From depth isocontours, cortical profiles can be constructed that transverse the cortex, which describes the laminae at a specified location along the cortical ribbon. An illustration of the derived profiles is shown in Figure 1.7. Current methods to model the cortical laminae thus far include manual techniques, equidistance, equipotential, and the equivolume model, which will be discussed in the sections below.

Cortical laminae can be generated with manual and computational techniques which involve sophisticated mathematical modelling. For example, Schleicher et al., 1998, derived cortical laminae by manually tracing drawn streamlines that orthogonally traversed the border between the grey-CSF surface and borders between grey-white matter surface [85]. In their study, Schleicher and associates used the manually defined profiles on stained cortical sections, quantifying the differences in mean profiles of a sliding window to provide an observer-independent detection of distinct architectural boundaries.

In more recent work, the equipotential model, or Laplace method, has been used extensively for evaluating the architecture of two-dimensional histological sections. For instance,
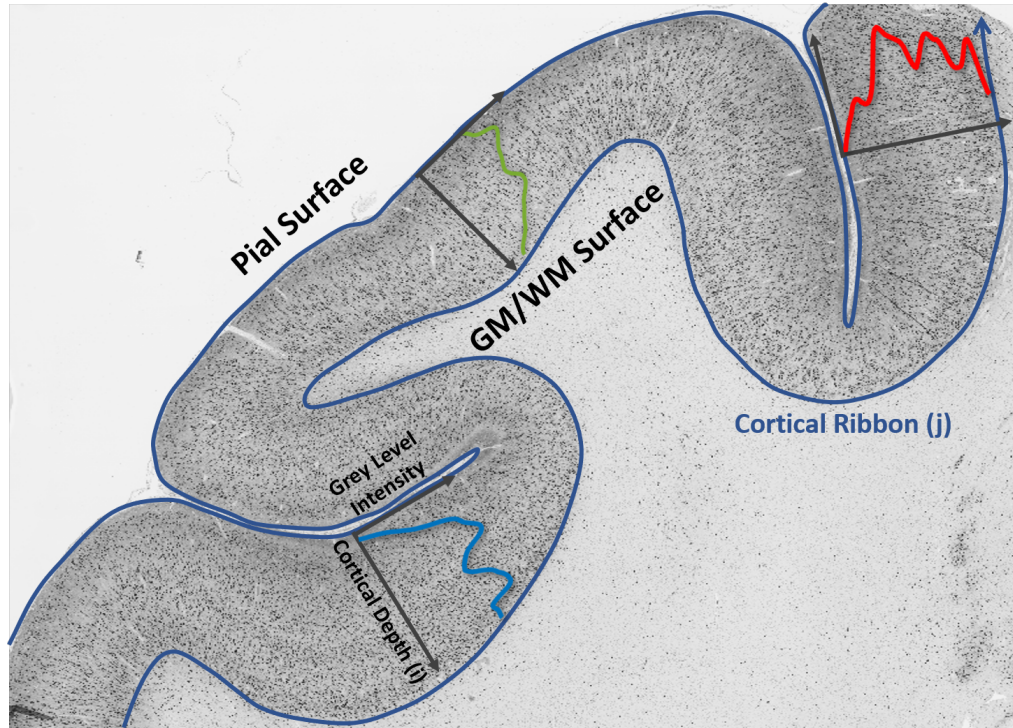
Figure 1.7: NeuN stained image illustrating examples in which profiles were sampled along the cortical depth (i) at specific locations along the cortical ribbon (j).

the more recent work of Schleicher et al., 2005, used Laplace profiles to provide a more automated method for observer-independent detection of cytoarchitectural boundaries [86]. The equipotential model has also been used to study neurotransmitter receptor laminar distribution patterns [87], and also for myeloarchitectonic parcellation studies [88]. Briefly, the equipotential model solves the Laplace equation (Eq.1.2) between the gray and white matter boundaries.

$$\nabla^2 \phi = \frac{\partial^2 \phi}{\partial x^2} + \frac{\partial^2 \phi}{\partial y^2} + \frac{\partial^2 \phi}{\partial z^2} \tag{1.1}$$

$$\nabla^2 \phi = 0 \tag{1.2}$$

Solutions of this partial differential equation have to fulfill the constraint that the sum of the (unmixed) second partial derivatives is zero. The main reason the equipotential model is used for sampling cortical laminae is that this model provides a one-to-one correspondence between the cortical boundary surfaces, derived profiles terminate perpendicularly at boundary surface

and profiles do not intersect. Despite the desirable properties of the Laplace method, a major limitation is that laminar mapping procedures are sensitive to smooth or gradual changes as caused by cortical folding [89]. However, corrections of layer widths and density for folding effects can increase the sensitivity in mapping procedures and reduce false positive detections [86].

The effects induced by the complex structure and folding pattern of the cortex makes analyzing cortical laminae challenging. This was first described in 1929 by a German scientist Bok [90] who was interested in the relationship between cortical folds and layer geometry. Through his research, it was shown that cortical folding caused gradual changes in the layering of the cortex. More specifically, Bok showed that relative location and width of the layers was dependent on the curvature of the cortex [90], an illustration is shown in Figure 1.8. In addition to layer geometry variations, von Economo and Koskinas (1925) described changes in cell shape due to cortical folding [25]. Due to the complex relationship between curvature and layer geometry, computational methods that analyze cortical laminae must take into account the inherent distortions caused by the folding of the cortex [85, 89].
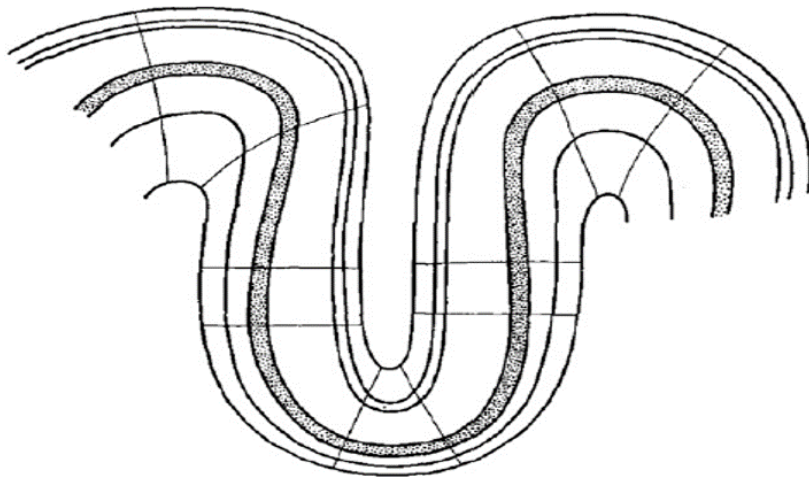
Figure 1.8: Sketch from Bok (1929) depicting the six cytoarchitechtonic layers and their relationship with curvature. Reprint figure adopted from Bok. 1929. *License agreement found in Appendix A.*

In high-resolution data (e.g., 0.5 mm or better), sampling laminae using equidistance and equipotential model will lead to misclassification of layers in regions of high curvature. To

remedy the anatomically incorrect sampling, the equivolume model leverages anatomical observations about how laminae become displaced due to the curvature and account for these inherent anatomical biases [89]. However, a major limitation of the equivolume model is the need for high-resolution 3D data, which limits the modelling to 3D neuroimaging studies. Despite histological sections offering a high spatial resolution to examine laminar architecture, they are often restricted by being 2D, and therefore are limited to the 2D cortical laminae models (e.g., equipotential and equidistance models).

1.4   Unsupervised Machine Learning

Machine learning (ML) is a tool that provides systems with the ability to learn and improve from experience without being explicitly programmed. To accomplish the process of learning, ML models are provided examples from which they extract patterns in data and make informed decisions in the future based on the samples provided. When a pattern has been correctly identified, or a model has been trained, the algorithm can be used to make individual predictions. In past research, ML methods have been applied to the identification of Alzheimer's disease [91, 92], schizophrenia [93, 94] and epilepsy [95, 65]. Similarly, ML algorithms can be used to identify pathologies in the resected tissue of TLE patients.

In general, ML methods are often categorized as supervised or unsupervised. The main difference between the two types is that supervised learning is performed using ground truth information of the data. In other words, in supervised machine learning both inputs and desired outputs (ground truth) are provided to the algorithm, to learn how to estimate the outputs given new unseen inputs. In supervised learning, the task of approximating a mapping function from input variables to discrete output variables is known as classification, whereas, regression refers to algorithms that map to continuous outputs. Common supervised algorithms include naive Bayes, support vector machines, and neural networks. In contrast, in unsupervised learning, the goal is to learn the inherent structure or hidden pattern of the data when provided with inputs

and no outputs. Common examples of unsupervised learning algorithms include clustering analysis, principal component analysis, and self-organizing maps. In this section, we will explore clustering techniques in detail. These are a set of unsupervised classification methods that can create meaningful groups or classes by directly processing data, without any previous knowledge or hypothesis about the groups that may be present. Also, we will describe in detail other unsupervised learning methods, such as principal component analysis and unsupervised anomaly detection.

1.4.1 Feature Space

The input to many of the ML algorithms is a **n** dimensional set of features that describe and summarize the data. A feature can be defined as an individual quantifiable property of an object being observed. Choosing informative, discriminating, independent features is a crucial step in effectively grouping a data-set into meaningful distinct clusters [96]. A cluster can be defined as a collection of objects which will have high similarity between them and are dissimilar to the objects belonging to other clusters. Figure 1.9 illustrates the importance of carefully choosing a feature set that helps differentiate groups of objects. With a good feature set, the spatial distance in the feature space clearly separates groups of interest, as shown in Figure 1.9 A). There are different categories of clustering methods that will classify clusters within a data set, including partitioning clustering, hierarchical clustering, density-based clustering.
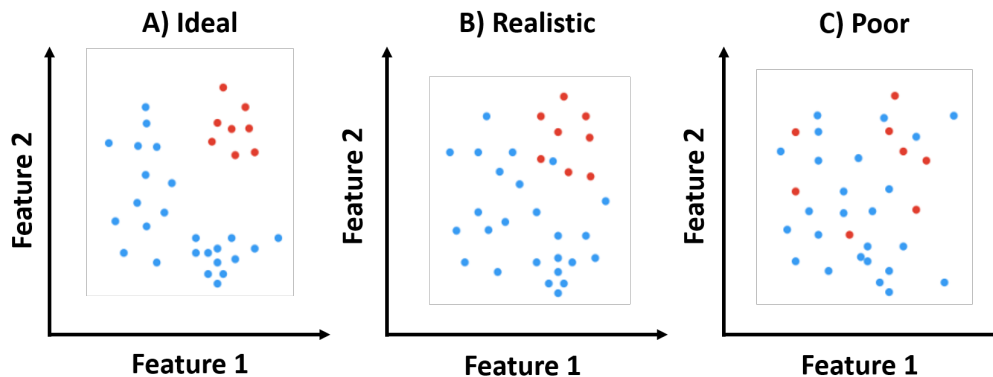
Figure 1.9: Examples of (n=2) dimensional feature space in A) ideal, realistic and poor scenario for a 2 class classification problem. Class 1 and 2 is represented in blue and red respectively.

1.4.2 Clustering Algorithms

K-means Clustering

Partitioning clustering is a clustering technique that subdivides a data set into a set of K groups, where K is the number of groups pre-specified by the user. A popular partitioning clustering method is K-means clustering [97], in which each cluster is represented by the average of the data points belonging to the cluster. The K-means algorithm is an iterative algorithm which starts by randomly defining K centroids in the feature space. The iterative steps of K-means algorithm include:

1. Assigning each data point to the nearest corresponding centroid based on euclidean distance.

2. Recalculating centroids by computing the mean of all the data points within each cluster.

This procedure is repeated until there is no or very little change in the computed centroid values. The K-means algorithm expects to find K clusters in the data; the algorithm will find specified clusters even when none exist. Therefore, it is crucial to validate the results of the K-means algorithm. A limitation to consider when applying K-means algorithm is due to the initial randomly chosen centroids, which means that starting at an undesirable location is possible. As a result, the iterative process may lead to some unlikely solution. To ensure that the solution is most probable, the K-means algorithm is repeated a few times to reach a reasonable solution. Another weak point to consider is the distance measure that the K-means algorithm uses (Euclidean Distance). When the variables or features used are significantly different in scale, the distances become dominated by the elements with the largest scale. Thus, it is crucial to normalize features before applying the K-means algorithm. Another problem that may arise is due to redundant information in the data or correlations between features. Typically, correlations between features can be removed using techniques such as principal component analysis (PCA), which is explained in detail in a later section.

Hierarchical Clustering

Hierarchical clustering (also known as Agglomerative clustering) is an algorithm that links similar objects, by a distance measure, into groups. These algorithms start by treating each observation as its own cluster. The algorithm iteratively proceeds by:

1. Identifying two clusters that are closest together.
2. Merges the two identified clusters into a single cluster.

This iterative process continues until the algorithm reaches K distinct clusters, where K is the distinct number of clusters specified by users. In addition to specifying K, an important parameter to specify is where distances are computed between two clusters. For example, distances can be computed between the two most similar parts of a cluster (single-linkages), the two least similar, or boundary observations (complete linkage), or the center of clusters (average-linkage). Compared to the K-means algorithm, agglomerative algorithms do not scale well to large data sets and require additional hyper-parameters to work effectively.

Density-Based Clustering

Density-based clustering is another unsupervised clustering algorithm tool that works by detecting areas where points are concentrated and where points are empty or sparse. Furthermore, areas of the feature space with insufficient density or extremely sparse set of points are points that are labelled as noise or outliers, that is, points characterized by unusual values. These classes of algorithms are more complex and require more running time than, for example, K-means clustering, however, they are capable of automatically guessing the number of clusters and grouping clusters of any arbitrary shape. There are several density-based clustering tools, among the three DBSCAN [98] is the most popular method.

DBSCAN uses a specified distance, search distance, to separate dense clusters from sparser noise. A cluster is defined as a maximal set of density-connected points. It relies on the idea that clusters are dense, it starts by exploring the feature space in every direction, within the

specified search distance, and marks a cluster boundary when points fall out of the specified search density. The main limitation of DBSCAN is that this algorithm requires two parameters to be defined, and is sensitive to the setting of parameters [99]. Thus, defining suitable values for these parameters may take several trials before reasonable results can be found.

1.4.3 Dimensionality Reduction

A common problem that may arise when choosing features is due to the correlation between variables, causing redundant information in selected features. In addition to eliminating redundant information, discarding irrelevant, and noisy data can prevent poor predictive or clustering performance [96].

Principal component analysis (PCA) is a statistical technique that uses an orthogonal transformation to transform a large number of (possibly) noisy and redundant variables into a smaller number of linearly uncorrelated variables, called principal components, with a minimum loss of information. The components determined from PCA are orthogonal to one another (i.e., uncorrelated), and each component contains compressed information from the original set of variables. The PCA transformation is defined in such a way that the first principal component accounts for as much of the variability in the data as possible, and each succeeding component accounts for as much of the remaining variability as possible under the constraint that the principal components are orthogonal to one another. Thus, the first two principal components obtained from PCA are the most informative in terms of variance, while the last two components are the most residual. The later principal components that contain minimal variance represent noise or redundancies from the original data, and therefore, are ignored. The dimensions of the original data-set are reduced by representing the data by a reduced number of components obtained by PCA that explain the majority of the explained variance. An example of a two-dimensional data set is represented by its principal components is shown in Figure 1.10. The results of PCA are typically discussed in terms of components scores and loadings. Components scores are the transformed variable values corresponding to a data point. While
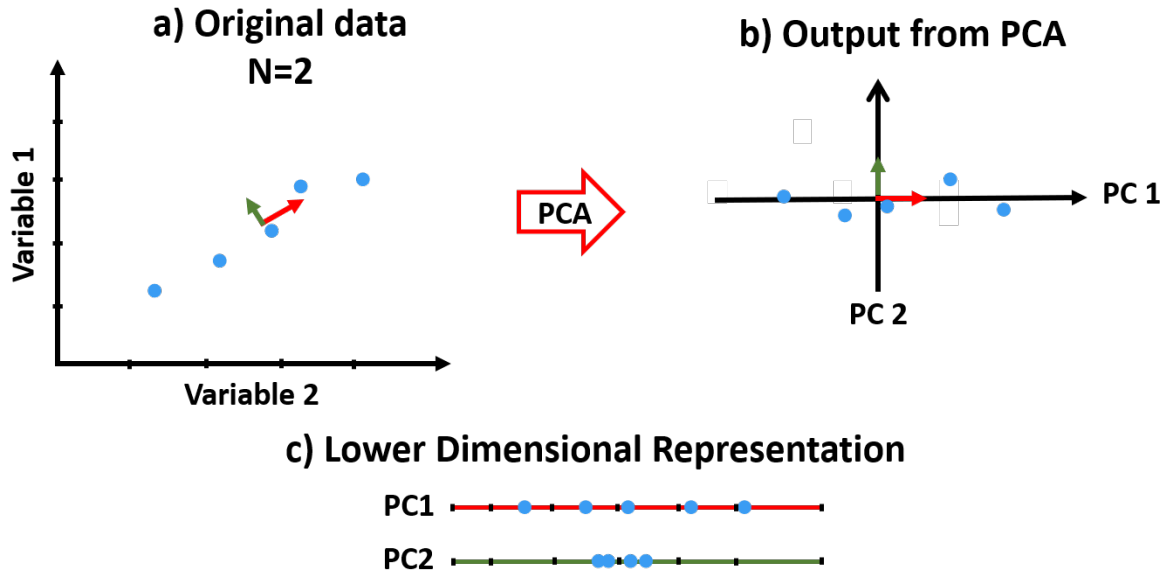
Figure 1.10: Two-dimension example of PCA: a) Original data with dimension of 2 b) Output from PCA c) Lower representation of data projected onto Principal Component (PC) 1 and 2. From the illustration in c), it is clear that PC 1 explains most of the explained variation and dropping PC2 can be justified since it contributes an insignificant amount of the data variation.

the loadings are the weights by which each variable should be multiplied to get the component score.

1.4.4 Anomaly Detection

In certain cases, data sets tend to be limited in the number of positive cases that can be obtained. Therefore there tends to be a high imbalance between positive and negative samples. Ultimately this poses difficulties for learning algorithms, as there is a bias towards one group. Anomaly detection algorithms can leverage a highly biased data-set and detect suspicious or rare observations. As a general definition, anomaly or outlier detection is the process of detecting a small fraction of data that differs from the global pattern defined by the data set. The goal of the anomaly detector is to identify unusual samples in the data set, without prior information of the anomaly, other than a low probability of occurrence. In unsupervised anomaly detection, a general assumption that is made is that the majority of the instances in the data are normal and the normal instances follow a pattern defined by the data-set.

Abnormal observations in data can sometimes have more significant meaning than a systematic error. For example, anomalies in medical image analysis can represent pathologies found in tissues. Most anomaly detection research in the medical field is focused on studying tissue prone to certain types of cancer with low screening detection, such as breast and brain cancers. A recent example of anomaly detection techniques being used in the medical domain is highlighted by Wei et al., 2018 [100]. In their work, they utilize a patch-based method to detect malignant tumours in breast tissue. In general, these studies rely on the assumption that the abnormal tissue is structurally distinct from the surrounding healthy tissue and the structural differences can be picked up by the imaging modality.

1.5   Research Question

Currently, there is a lack of objective or quantitative methods for defining FCD pathology, and qualitative ratings by pathologists can be highly variable, especially for subtle lesions, and require time-consuming annotations by trained specialists. The goal of this research is to develop image analysis and machine learning techniques for histopathological examination of resected brain tissue to objectively quantify and evaluate cortical tissue in temporal lobe epilepsy patients. This can provide quantitative data for MRI-histology comparison studies and can also improve current histopathology workflows. Also, with the combination of image processing and machine learning tools, histological data can be studied quantitatively to expand our understanding of the biological variability between normal and dysplastic cortex.

A major challenge in analyzing cortical histology slides to quantify epilepsy lesions is that the laminae can be distorted in different parts of the sample. This is caused by mainly two sources of variability: displacement of laminae in regions of high curvature (e.g. gyral peaks of sulcal depths), and out-of-plane sampling problems when the histological plane is not perpendicular to the cortical mantle. Pathologists generally address the latter problem by only examining the tissue that appears thinnest (most likely to be sampled perpendicularly).

However, this excludes a large amount of tissue that could be analyzed if accurate identification of these regions could be made. The former problem, the displacement of laminae at gyral peaks or sulcal depths, was first noted by Bok [90]. For example, laminae near the pial surface boundary tend to be stretched thin near gyral peaks and squeezed thicker at sulcal depths, and vice versa for laminae at the white matter boundary.

We hypothesize that with the correct histological image features that summarize and describe the epilepsy lesions, an unsupervised model can differentiate the subtle abnormalities in cortical architecture from the surrounding healthy tissue in the resected histological data. However, a general assumption is required to achieve this hypothesis. Specifically, it is assumed that the normal instances (i.e. healthy tissue) form a distinct pattern defined by the selected histological features, and pathological tissue is deviant from this defined pattern. A significant source of variability that can affect the classification of these two groups come from inherent anatomical biases as well as other artifacts. Therefore, a crucial step in differentiating the subtle abnormalities in cortical architecture is to eliminate or reduce the variability due to the aforementioned distortions and biases.

In this study, we investigate two approaches for correcting the non-pathological distortions and develop a technique to generate laminar profiles that are spatially-normalized to a common reference. We show that by performing these corrections, the laminar correspondence can be achieved across regions of the cortex, within and between subjects. Furthermore, we applied unsupervised clustering to eliminate processing artifacts, such as out-of-plane slicing and to reduce variability due to morphological differences. We then perform unsupervised anomaly detection on the normalized data to identify regions of abnormal architecture across subjects and slides.

1.6 Thesis Objectives

The overall goal of this thesis was to create a tool to quantitatively classify layer specific anomalies in 2D histological brain slices. This objective can be broken into three sub-objectives as follows:

1. Create a coordinate system for the cortical laminae in 2D histology.

2. Eliminate variability due to inherent anatomical biases as well as other artifacts affecting classification.

3. Select histological image features that are associated with epilepsy lesions and apply unsupervised learning to examine whether subtle abnormalities in cortical architecture can be detected quantitatively.
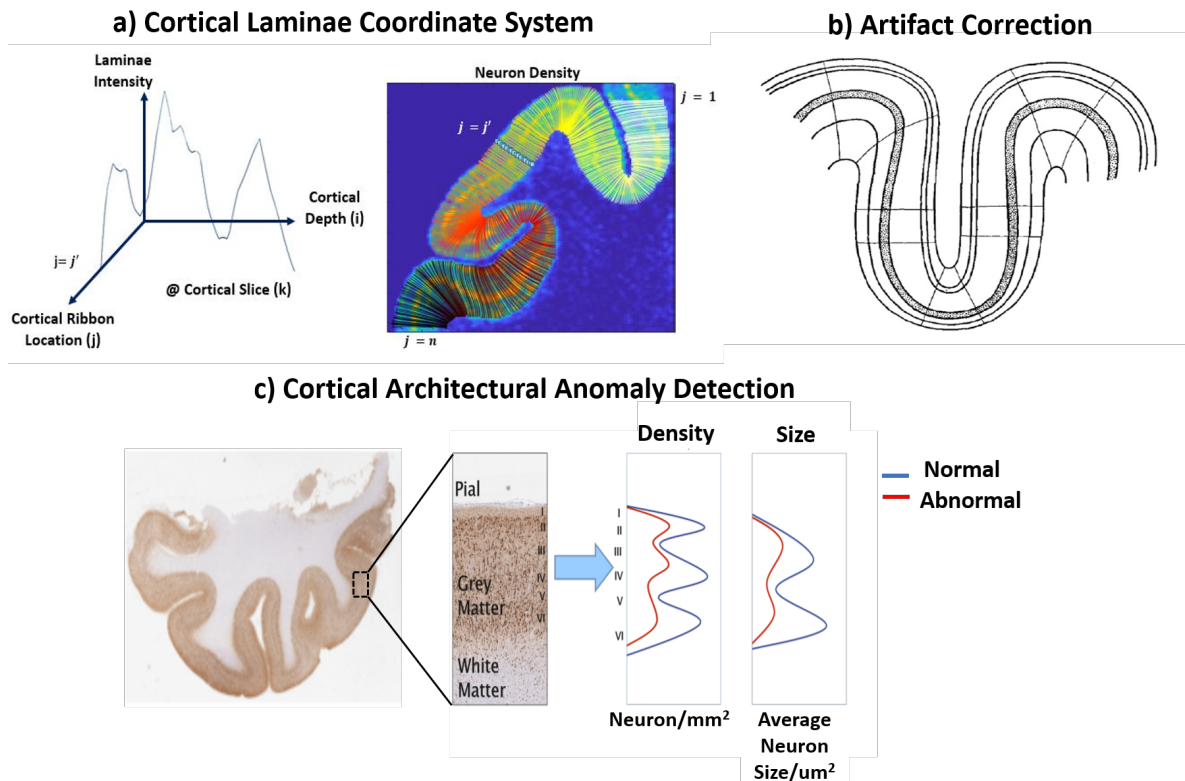
Figure 1.11: Overview of objectives illustrating: **a)** Example of cortical laminae coordinate system. **b)** inherent artifacts present within cortical data **c)** A overview of the cortical architectural anomaly detection

Chapter 2

Method

We began with whole slide images of brain obtained from resected tissue of patients suffering from medically intractable TLE. We then performed neuron cell body segmentation to extract microscale feature maps that describe and summarize information from our high-resolution histological images, using a patch-based analysis. Subsequently, we extracted profiles which were obtained using equipotential cortical laminae modelling. We then corrected for the cortical layer distortion by applying a technique that leverages anatomical observation about how laminae become displaced in addition to an iterative warping technique to normalize profiles across subjects to a common reference. Furthermore, we applied unsupervised clustering to eliminate processing artifacts and to reduce variability due to morphological differences. The methods for correcting the mentioned distortions and biases in histological slides are summarized and described in detail in the following sections. Finally, we applied an unsupervised anomaly detection algorithm within defined sub-regions to identify anomalous data, which was hypothesized to represent pathological tissue.
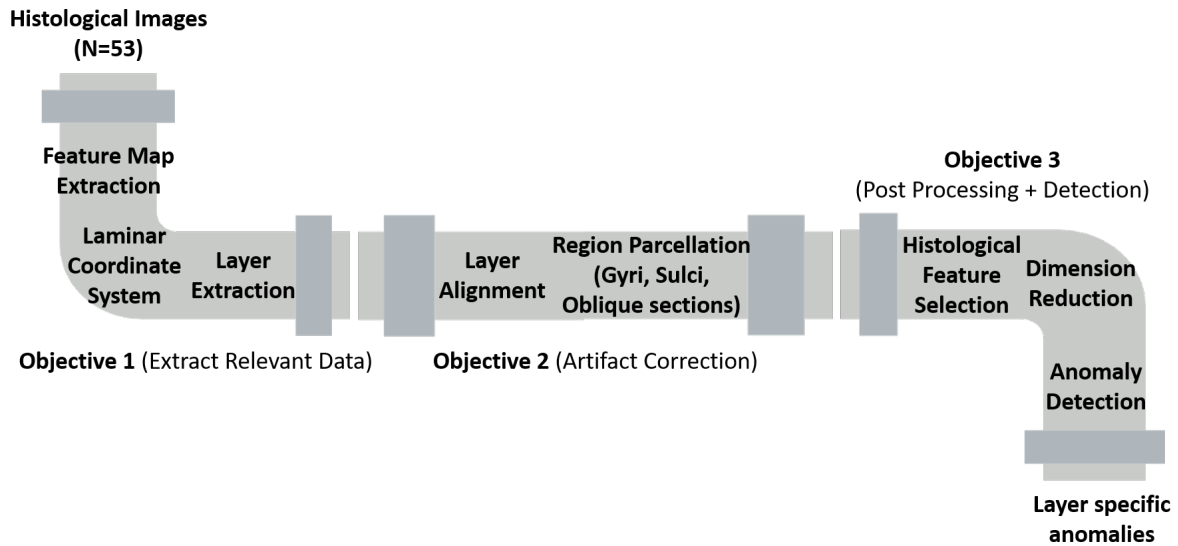
Figure 2.1: Pipeline outlining the main steps and workflow

2.1 Recruitment, Image Acquisition & Histological Processing

Patients suffering from intractable epilepsy who were approved for anterior temporal lobe lobectomy (ATL) at University Hospital, were recruited in an ongoing study at Robarts Research Institute. The study cohort included 90 temporal lobe patients who underwent epilepsy surgery and the resection of two specimens, temporal neocortex and hippocampus. Within this cohort, a subset of 27 patients was selected for analysis in this study. Inclusion of these subjects was determined based on the availability of minimally artifact-free NeuN stained neocortical slides. In addition, this cohort included patients with wide range of verified pathology. This project was cleared by the Health Sciences Research Ethics Board of Western University, and informed consent was obtained from all patients prior to their participation in the study. Table 2.1 summarizes the relevant patient data, including the sex, age, seizure origin, neocortical pathological findings and MRI findings for our cohort.
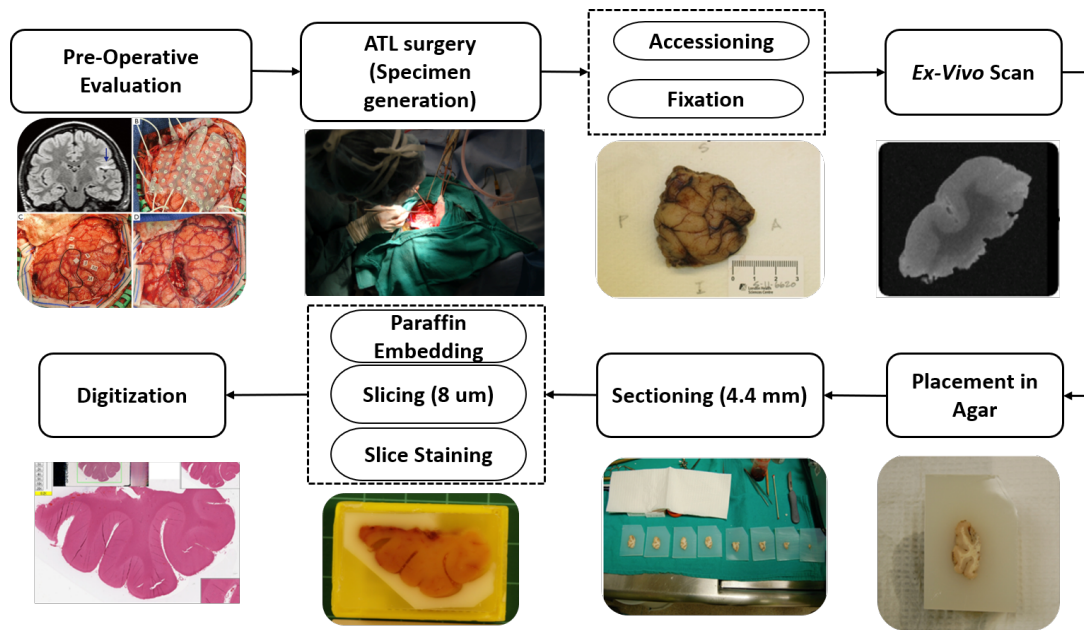
Figure 2.2: Overview of the histological processing and data generation.

2.1.1 Histological Preparation

Histological processing was performed on tissue samples obtained from the surgically resected temporal lobe of patients with temporal lobe epilepsy (TLE). Following surgery, specimens underwent accessioning and grossing at the Department of Pathology at the Univerisity Hospital of London Health Sciences Centre, in addition, these specimens were also cut through the coronal plane into two equal halves, anterior and posterior. The halved specimens were then embedded in agar for stabilization and were sectioned into 4.4mm pieces in the anterior to posterior direction, using a standard deli slicer (Globe Food Equipment Company, Dayton, OH, USA). Coronal, 8-um thick sections of formalin-fixed, paraffin-embedded tissue were then processed with a NeuN staining. Following staining, the resulting histology slides were digitized on a ScanScope GL (Aperio Technologies, Vista, CA, USA) bright-field slide scanning system in BigTIFF file format, using a pixel resolution of 0.5 um. For example, the image resolution for a typical slide is 86,030 x 44,791 pixels which correspond to metric dimensions of approximately 172 x 90 mm (a portion of an image is shown in Figure 2.3 a)). A detailed overview of the histological processing is described in Figure 2.1.

2.2   Histological Quantification

We pre-processed the high-resolution histology images by performing automated segmentation of neurons in 100μm x100μm patches and generating summary feature maps that are relevant in the detection of FCD lesions. This effectively provides images down-sampled by 200 times where each pixel contains neuronal information derived from the high-resolution images, as shown in Figure 2.3 b).

2.2.1   Neuron Segmentation

Briefly, image segmentation is the process of dividing a digital image into meaningful regions or segments, often based on the characteristics of the pixels in the image. Image segmentation could involve separating foreground from background, or clustering regions of pixels based on similarities in colour or shape. Segments of interest are separated from the background and each other using a variety of segmentation techniques. A common application of image segmentation in medical imaging is to detect and label pixels in an image that represents a pathology in a patient's brain or used to detect specific cell types such as neurons.

There are many challenges in accurately and efficiently detecting and segmenting cells in a histology specimen. For example, the 2D representation of a 3-D tissue sample imposes difficulties in detecting cell bodies due to artifacts that result from the sectioning process. This includes partially imaged cell bodies, imaging of cells at non-optimal angles and damage to cell bodies due to the preparation processing. In addition, image noise and other artifacts can result in additional errors and difficulties. Therefore careful considerations are necessary for detecting and segmenting cells in histological images. We have adopted validated work from [101]. Their segmentation and detection method involved a two-step process in which the NeuN stained images undergo colour deconvolution, to separate individual colours within the slide, followed by a marker-based watershed segmentation technique. The segmentation results were compared with the ground truth by calculating the amount of area overlap measured by

the Dice coefficient. The Dice coefficient varies between 0 and 1, higher coefficients indicate better agreement between the segmentation result and ground truth. On average, the mean dice similarity coefficient was reported at 0.77, which falls within an acceptable range as defined by [102].

2.2.2   Feature Map Extraction

Choosing informative, discriminating, independent features that summarize information from the original high-resolution images is a crucial precursor to effectively being able to evaluate the architecture and irregularities of neural tissue (Figure 3.1-3.2). In this section, we describe chosen features that are commonly used to describe the pathologies found within cortical tissue.

Following segmentation, each image was divided into 100μm x 100μm overlapping patches. For each 100μm x 100μm patch, histopathologic features were extracted, and maps of each feature were generated for each slide. Each feature map described and summarized the relevant characteristics of the high-resolution histological image. The relevant features used for FCD detection included: Neuron density, shown in Figure 2.3 b), which is obtained from the number of neurons within a patch. Clinically neuron density may significantly decrease within an area with pathology. In addition, Neuron size feature maps were obtained by determining the average size of individual neurons within a patch. Specifically, the size of the neuron was defined by the number of pixels a single neuron defined. In epilepsy, abnormally large neurons can be indicative of balloon cells, which are present in several subtypes of FCD. Furthermore, eccentricity, a metric used to measure the shape of the neuron cell body, was computed for each neuron within a patch. Specifically, this metric quantified the degree of circularity of cell bodies. Eccentricity was calculated as a ratio of the foci of an ellipse (neuron) and its major axis and is a scalar between 0 and 1. Eccentricity feature maps are indicative of neuron morphology and may be able to assess FCD in epilepsy. In this work, we define neuron density, size, and eccentricity as quantitative microscopic features.
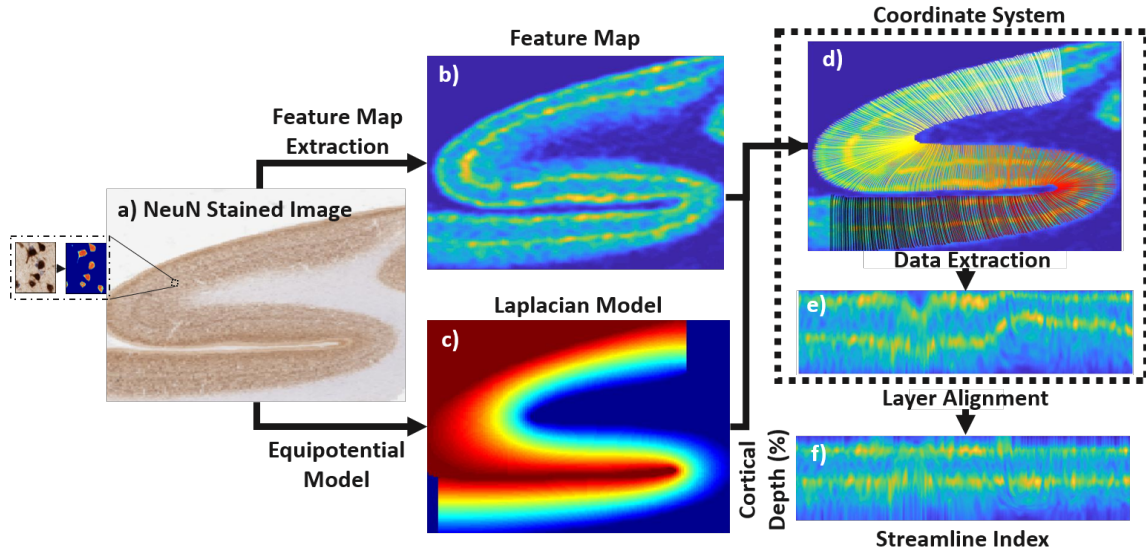
Figure 2.3: General approach of the proposed cortical laminar alignment. **a)** NeuN stained image **b)** Neuron density feature map **c)** Solved Laplacian with the domain being grey matter, and boundary conditions being the pia and CWM junction **d)** Streamlines derived from equi-potential model, laid on top of the feature map. **e)** Uncorrected profiles sampled from the feature map **f)** Spectral aligned profiles using Correlation Optimized warping (COW)

2.3 Cortical Coordinate Extraction

The procedure for extracting profiles of cortical laminae is based on creating a coordinate system that allows sampling along the cortical depth from the pial to cortex-white matter (CWM) junction and along the length of cortical tissue being examined. For this, streamlines were generated across a Laplacian solution (Figure 2.3 c) with the domain as the cortex and boundary conditions as pia and CWM junction. We performed the cortical segmentation using a semi-automated approach. However, this task can be further automated when we apply the technique to a larger set of subjects and slides. Streamlines were kept in sequential order from one edge of the cortical ribbon to the other, and each profile was resampled to a normalized depth to have 1000 vertices.

2.3.1 Semi-automated Cortical Segmentation

We created a semi-automated segmentation approach, using Qupath software [103], to obtain cortical segmentation's required from our equipotential model. The model used to train the

segmentation algorithm was a random forest (RF) classifier, which used 6640 random training samples from a variety of subjects and slides. Training samples are defined as 5x5 tiled instances of the 20um down-sampled image, as shown in Figure 2.4 a and Figure 2.4 b. These samples came from all three regions: grey, white matter, and background. The trained classifier was used to create segmentation prediction from the down-sampled 20um NeuN stained image. Specifically, the algorithm created a 5x5 grid from which we extracted common statistical measures such as mean, median, variance, max, min from each unsmoothed and smoothed colour space images. The colour space images included the three components in Red, Green, Blue (RGB) space and the three components from Hue, Saturation, and Brightness (HSV) space. The smoothing kernel size used to smooth the colour space images was a full-width half maximum (FWHM) of 50 pixels. An example of the feature map is shown in Figure 2.4 c, and in total, there were 60 feature maps used in this model. The classifier used the aforementioned features to train on and predict the class of each pixel; an example of the prediction result is shown in Figure 2.4 d. Since the equipotential model is sensitive to the boundary conditions we then manually corrected for any mistakes made by the classifier — corrections were made using ITK-snap toolbox.
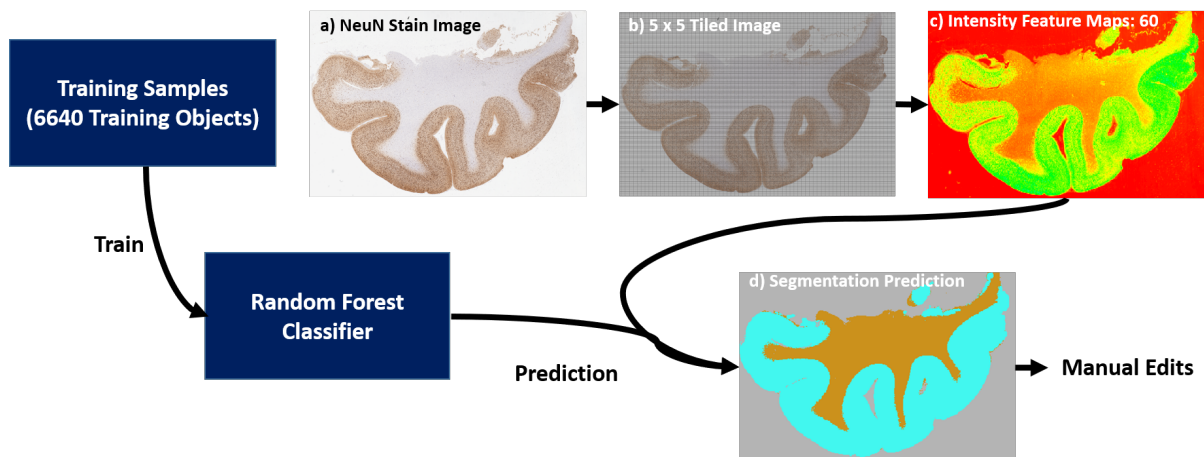
Figure 2.4: Overview of semi-automated cortical segmentation procedure **a)** Down sampled NeuN stained image (20um x 20um) **b)** 5x5 pixel tiled image overlayed on top of 20um NeuN stained image. **c)** Example of Intensity feature used to train random forest classifer **d)** Example of segmentation prediction

2.3.2 Laplacian Cortical Laminae Model

In order to analyze layer architecture or function, it is desirable to define a suitable coordinate system that allows sampling of cortical laminae. The equipotential model, or the Laplacian model, can account for the unambiguous mapping between the cortical boundaries in highly convoluted and variable cortical environments. Due to the ability to account for highly folded morphology, the Laplacian model has been used extensively in research, especially when calculating neocortical thickness. In principal, the technique generates a scalar field, or gradient, between the defined boundary conditions (often referred to as source and sink). Here, we defined the source as the pial-background boundary and the sink as the grey matter-white matter surface. The Laplacian solution provides a smooth gradient from the defined boundary conditions. Streamlines can be generated from the gradient of the Laplacian solution and can be used to sample cortical profiles and accurate cortical thickness measures. To solve the Laplacian equation, we used a modified version of the open-source software from the following git repository: `https://github.com/jordandekraker/HippUnfolding/tree/master/tools/Laplace_solver`. An example of solved Laplacian on a cortical slide is shown in Figure 2.3 c).

2.3.3 Sampling cortical profiles

The streamlines (Figure 2.3d) were used to sample intensities from the given feature maps, producing a 2D image vertically indexed by cortical depth (Figure 2.3e). Prior to extracting the profiles, each feature map was smoothed by a 3x3 averaging filter to reduce noise [4]. The unfiltered images caused periodic variations [104] and local changes in neighbouring tissue. Due to the differences in cortical thickness and thus differences in streamline length, each profile was standardized to encompass 1000 values corresponding to the cortical depth from 0% to 100%. This was done by resampling the data evenly using linear interpolation.

2.3.4 Macroscopic Features

In addition to extracting cortical profiles, the streamlines generated from the equipotential models were used to extract macroscopic cortical features which are defined here as the cortical thickness and local curvature and are obtained for each streamline. Cortical thickness was defined as the pathlength along a streamline Eq.2.1 and can be useful in identifying cortical regions that are sampled poorly. Note that x and y refer to the coordinates along a single streamline.

$$Pathlength = \sum_{i=1}^{n-1} |P_i - P_{i+1}| \tag{2.1}$$

$$|P_i - P_{(i+1)}| = \sqrt{(x_i - x_{i+1})^2 + (y_i - y_{i+1})^2} \tag{2.2}$$

In order to estimate curvature, it is required that we must first identify a 2D curve that models the shape of the histological sample. This was done by identifying the 2D curve at 50% depth along with the cortical tissue. Due to the potentially distorted cortical surface, curvature values can be difficult to estimate directly from the noisy 2D curves. To overcome this difficulty, we smoothed our extracted curves using a moving averaging filter. Once we obtained our smooth curves, we applied the classical definition of curvature, described in Eq.2.3. Note x and y in Eq.2.3 refer to the coordinates along the defined 2D curve.

$$\kappa = \frac{x'y'' - y'x''}{\sqrt[3]{(x')^2 + (y')^2}} \tag{2.3}$$

Both curvature and thickness values were smoothed by a moving averaging, and median filter to eliminate abrupt local variability.

2.4 Cortical Layer Correction

The 2D cortical profiles shown in Figure 1e provide an image representation, namely an equipotential modelling of the cortex, that is meant to account for the complex folding of

the cortex. This approach was popularized with 3D cortical thickness analyses [105] since it provides a smooth mapping between the pial and white surfaces. Ideally, the Laplacian streamlines define cortical columns, and cortical laminae can be defined from the rows in these images. However, these rows are distorted due to the aforementioned issues with out-of-plane sampling and anatomical differences between gyral and sulcal regions of cortex.

2.4.1 Iso-Area Correction

The seminal paper by Bok [90] explained the observed laminar differences in gyral and sulcal peaks as conservation of volume within each lamina. An equi-volume, or 'iso-volume,' approach was proposed more recently [89] to correct for these differences in high-resolution 3D imaging data. In the current work, we develop an equivalent 2D or 'iso-area' implementation in which equipotential derived profiles are resampled at equal areas instead of equal volumes. We computed estimates of the area along the profile by examining adjacent streamlines, then shifted the profile vertices based on the cumulative area along the profile. The profiles were then reparameterized evenly to 1000 vertices. Prior to resampling the profiles at equal areas, we normalized the total area along each streamline and performed Gaussian smoothing of the shifting function across vertices in order to avoid abrupt changes between neighbouring profiles. When applying the iso-area model, we effectively stretch and compress the profiles in a way that counters the curvature dependent variability seen in gyral and sulcal regions.

2.4.2 Iterative Warping Correction

After iso-area correction, distortions in the layers can remain due to histological sampling that varies across the slide, or from cytoarchitectural differences that exist between brain areas. One approach to this problem is to perform a transformation to each vertical profile, effectively bringing all the columns into alignment. Methods for spectral alignment used in nuclear magnetic resonance aim to achieve an analogous goal, that is, correcting for shifts and warps in NMR spectra (1-D profiles) [106]. We adopted a commonly used technique in this do-

main, correlation optimized warping (COW) [107]. This alignment algorithm stretches and compresses segments of the profiles, using piecewise interpolation, in order to maximize the overall Pearson correlation coefficient between profiles and the chosen reference. Specifically, the sample and reference profile are split into segments, of length **m**, and the boundaries of the segment are allowed to be stretched or compressed a certain number of data points in either direction – the local flexibility of alignment or slack size **t**. The slack size and segment length are two parameters that were required by the COW algorithm and were set through trial and error. The optimal alignment is found by finding the optimal combination of warped segments using Pearson correction and our reference as our cost function.
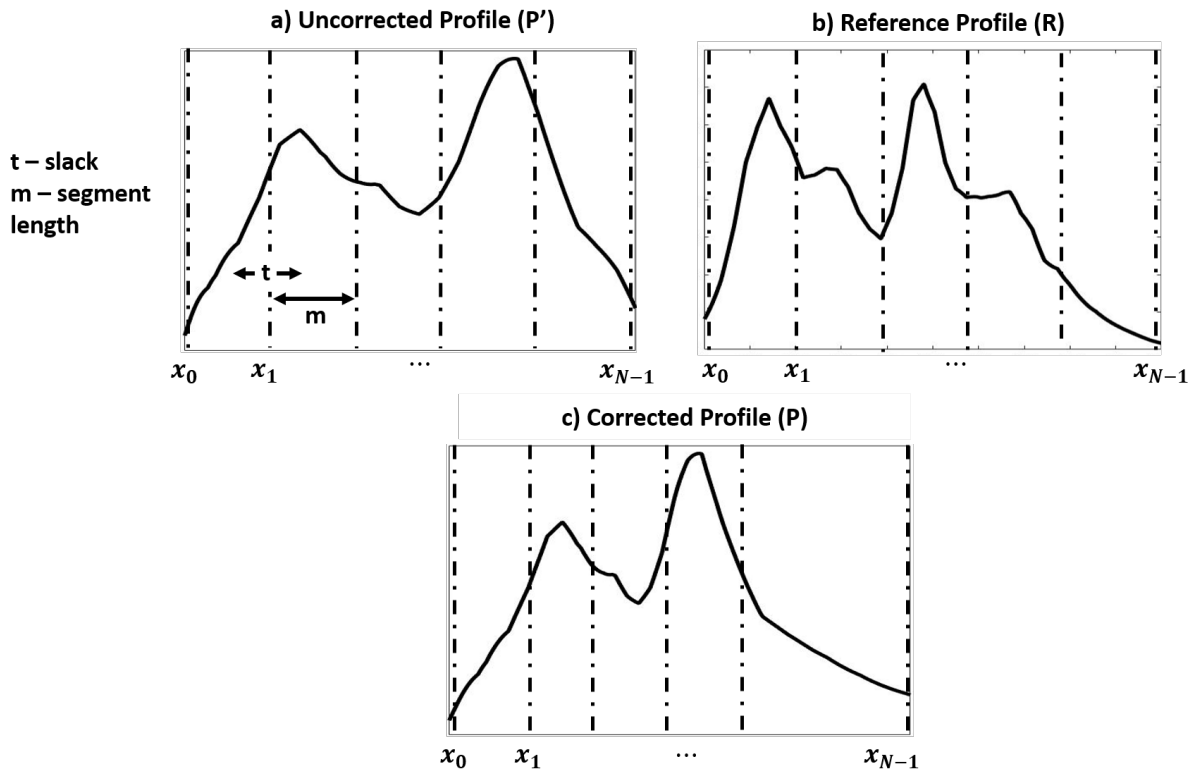
Figure 2.5: Example image describing the correlation optimized warping (COW) algorithm . **a)** Uncorrected profile **b)** Reference profile chosen from the data set. **c)** Aligned profile after a single iteration of COW. Note **t** represents the amount of allowable stretching or compressing and **m** represents the length of segments. Dotted lines represent the boundaries of the segments before (a-b) and after correction (c).

We developed an iterative approach for defining the reference, initialized by the profile with the minimum average Euclidean distance from all other density profiles. With each further iteration, we performed COW to align all profiles to the existing reference, then averaged those

aligned profiles to obtain a new reference profile. We iterated until the change in the average reference profile met a predefined threshold of 0.01 or 10 iterations (this typically occurs after 2 to 5 iterations). Prior to applying each transformation obtained from the COW registration, we smoothed each transformation with neighbouring profiles using a Gaussian filter in order to avoid abrupt changes between neighbouring profiles. An example of the corrected profiles is shown in Figure 2.3f. In order to increase the correspondence of layers between subjects and slides, the data were normalized to a common reference. This was done by concatenating the data across subjects and slides and applying our iterative reference-based warping correction to the iso-area corrected slides. An overview of this process is shown in Figure 2.6.
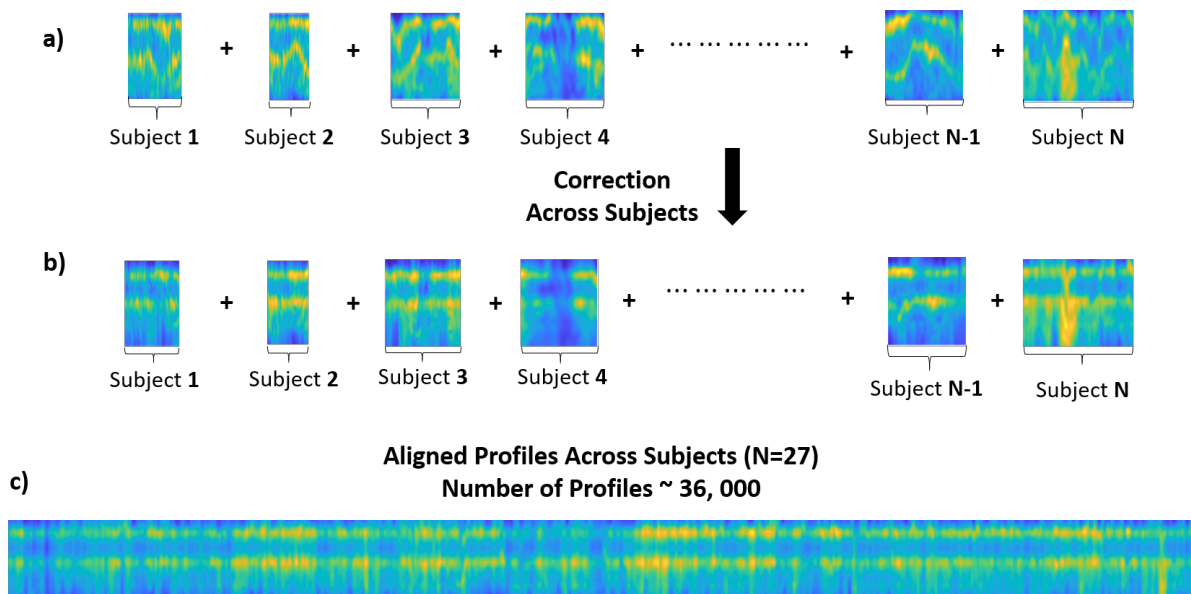
Figure 2.6: Overview of alignment correction across multiple slides and subjects. **a)** Concatenated uncorrected neuron density profiles across subjects **b)** iterative reference based registration applied to profiles using Correlation Optimized Warping (COW) **c)** Aligned profiles across all subjects and slides

2.5   Validation of Cortical Layer Alignment

For qualitative validation, we performed the proposed alignment approach on 4 slides from 3 subjects and evaluated our ability to align the cortical gray matter effectively. The qualitative assessment was evaluated by assessing the average profiles and the degree of variation before and after correction. In general, distortions or misalignment in the data contribute to a greater

variance in the average profiles; this ultimately leads to smoothing of characteristic profile shape features, such as smoothing of peaks corresponding to layers with high-density neurons or large average neuron size. Ideally, the average profile from the neuron density feature map, if aligned, will have two peaks, which correspond to the highly-dense granular neuronal layers II, IV. In addition, we also expect layers III and V to have peaks in the average profile corresponding to the neuron size feature map. A depiction of the cortical layers is shown in Figure 2.7 a) which shows the expected trajectory along the cortical layer for both neuron density and size (Figure 2.7 b-c).
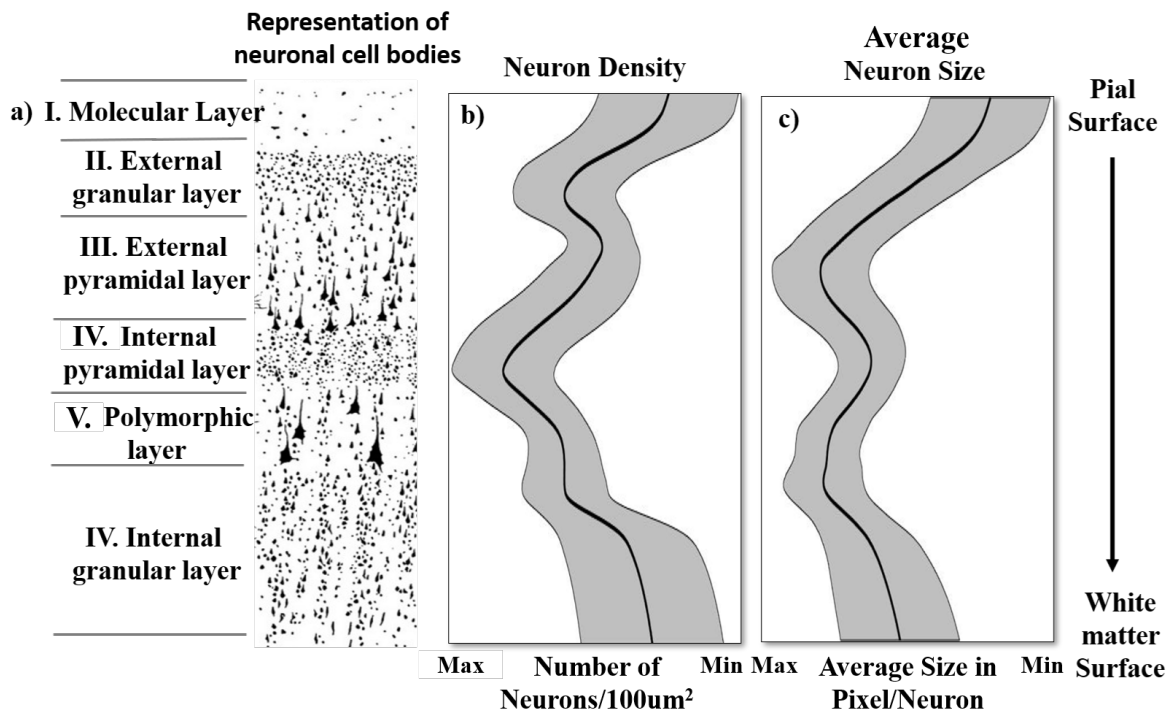
Figure 2.7: **a)** Representation of neuronal cell bodies along cortical layers. **b)** Average neuron density profile **c)** Average neuron size profile. Density and size profiles obtained from average across subjects.

To evaluate the cortical layer alignment quantitatively, we binned the profiles across subjects into three groups based on their cortical thickness measures, which can be a measure of the quality of sectioning. Specifically, we grouped the profiles into low, medium and high thickness groups. These groups were defined from the mean and standard deviation of the cortical thickness measure. Specifically, medium thickness profiles were defined as profiles with thickness within two standard deviations from the mean thickness. Whereas, high and

low thickness profiles were defined as profiles with thickness measure above and below two standard deviations from the mean respectively. We then calculated the Euclidean distance between the average profile in each bin and individual profile across subjects before and after the cortical layer correction. In general, a decreased Euclidean distance between the average and individual profile is indicative of better alignment (refer to section 3.2.3 Figure 3.9).

2.6   Morphological Clustering

We used the macroscopic features derived from our coordinate system and applied unsupervised clustering to eliminate processing artifacts and identify sub-regions that differ in cell morphology. The following section defines the specific inherent anatomical biases and processing artifacts seen within the data and provides a solution for accounting for this source of variability.

Effects induced by cortical folding: Another major challenge in analyzing high resolution cortical histological data is that there are differences in cell morphology across the gyri, sulci, and straight cortex regions [25] due to the effects induced by the cortical folding. These differences in cell morphology can affect both the density feature maps and other features that quantify cell morphology. Ultimately these differences, when not accounted for, can result in poor comparative analysis in downstream processing.

Cutting effects: In addition, the angle of sectioning relative to the cortical mantle affects the observed structural architecture, and thus, non-optimal sections must not be interpreted as structural features of the tissue shown. The pathologist typically ignores these areas where sectioning is cut obliquely as they distort the laminar pattern and provide less reliable information. A common solution is to optimize the sampling scheme to reduce or eliminate this artifact, however, due to the anisotropic nature of the cortex even with optimized sectioning areas within the sample may still result in obliquely sectioned regions. Many of the features used to describe and summarize our histological data greatly vary if the orientation of the plane

of sectioning changes and, thus, are sensitive to deviations from optimal sectioning.

One solution is to identify the different sub-regions (gyri, sulci, straight cortex, and oblique section regions) such that analysis downstream can be contained within an individual region of interest. In order to identify such sub-regions, it is required to choose suitable quantifiable metrics that accurately divide the data into such regions. Figure 2.8 depicts the typical
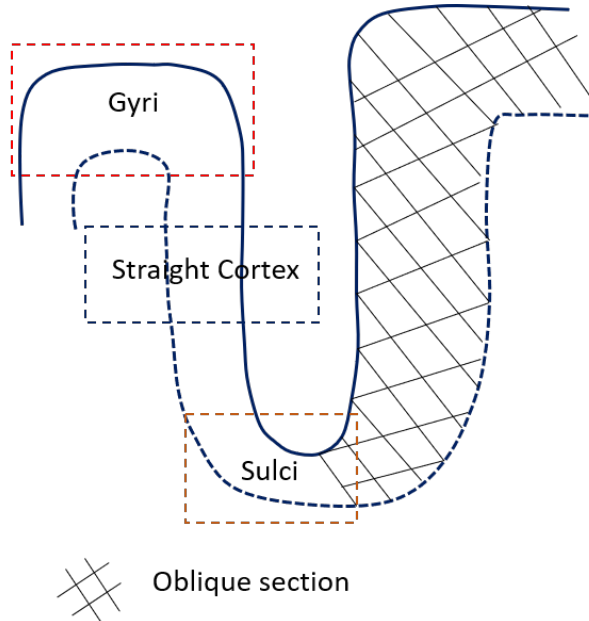
Figure 2.8: Depiction of typical cortical morphology in a 2D histological slice.

morphology of a 2D cortical slide. From this figure, it is clear that thickness and curvature are suitable metrics to subdivide the mentioned sub-regions. Specifically, when observing the overall low power morphology of the cortex, there are a few obvious trends such as:

1. The gyri regions are relatively thick and have high negative curvature. Whereas, the sulcus is a relatively thin piece of cortex with high positive curvature

2. The area between the sulcus and gyrus, namely the straight segments of cortex, has low curvature with thicker cortex at the sulci, and thinner than at gyri.

3. The oblique sectioned regions typically have the greatest cortical thickness with no bound on curvature.

Therefore, to achieve this goal, we used cortical thickness and curvature (Figure 2.9 b) and k means cluster (k=4) to cluster the data appropriately (Figure 2.9 c, d). Figure 2.9 depicts an overview of this process.
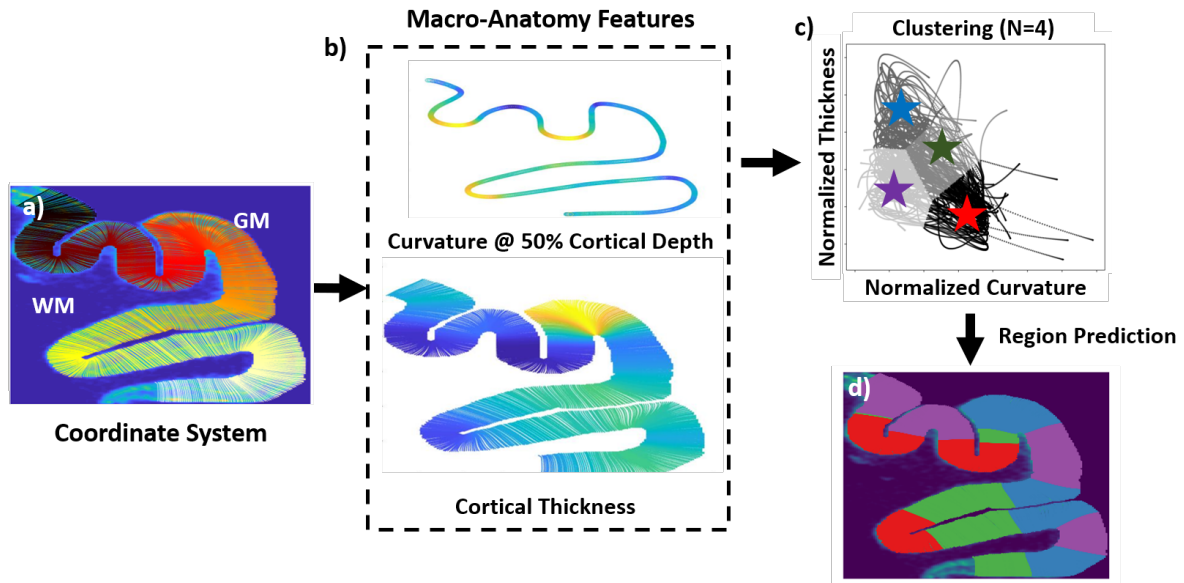
Figure 2.9: Morphological Clustering pipeline: **a)** examples of equi-potential streamlines used to derive morphological metrics **b)** Derived macro-anatomy features, namely cortical curvature and thickness **c)** K means clustering result on morphological data across subjects, this sub-figure depicts the normalized data **d)** Result of clustering as a segmentation.

2.7 Dimension Reduction

The procedure for accurately grouping (clustering) data is based on finding the smallest subset of relevant features that can exaggerate differences between the groups within the data set. Here we have chosen histological features that are associated with cortical lesions; these included the following: neuron density, size, and eccentricity. We obtained these feature maps across all subjects and using the coordinate system we obtained profiles which described the laminar specific data from each map. Once the profiles from each feature map across subjects were normalized to a common reference, we extracted quantifiable metrics that describe profile shape using a set of 10 features and applied principal component analysis to reduce and eliminate redundancies in the feature set.

2.7.1 Profile Shape Feature Extraction

Differences in the shape of neuronal profiles can be a feature of dysplasia. Profile shape was quantified using a set of 10 attributes extracted from each profile and its absolute derivative. The attributes extracted from each profile included the mean amplitude and the first four central moments around the mean (the mean, standard deviation, skewness and kurtosis). The selection of these 10 attributes that describe a profile shape was derived using a heuristic approach from Schleicher et. al [85]. In total there are 30 attributes 10 from a profile of each feature map. The individual 10 attributes were normalized, using z-score normalization, across subjects in order to maintain equal weight to each attribute. Figure 2.10 illustrates the profile feature extraction.
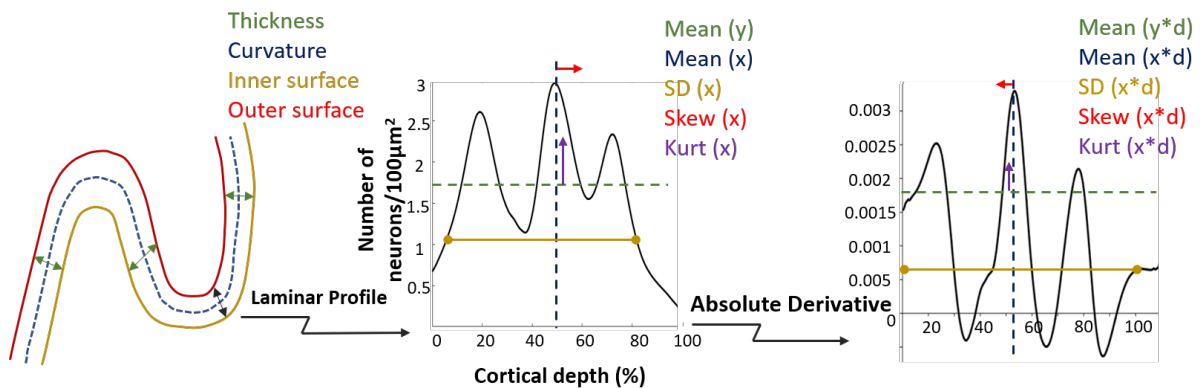
Figure 2.10: Density Profile attribute extraction example illustrating the features extracted from an individual profile which describe the profile shape. Note there are 30 extracted attributes, 10 from a profile of each feature map. These attributes were extracted across all streamlines.

2.7.2 Principal Component Analysis

After extracting profile shape attributes, it was noticed that there were correlations between attributes within feature maps but also between them. Correlations between variables in a multivariate analysis can result in poor predictive or clustering performance. Therefore, we applied principal component analysis (PCA) to eliminate the redundancies found within our data. PCA summarizes the variation in correlated multivariate attributes to a set of non-correlated components, where each component is a linear combination of the original variables or features. The

goal of PCA is to reduce the dimensionality by extracting the smallest number of components that account for most of the variations within the original dataset. In this study, we choose a number of principal components that provided a total of 95% of the variation in the original data (Figure 2.11). This resulted in 10 principal components, whereas the original number of attributes was 30. The remaining principal components that made up 5% of the variation were discarded as they form the most residual part of the data and most likely represent noise and redundancies.
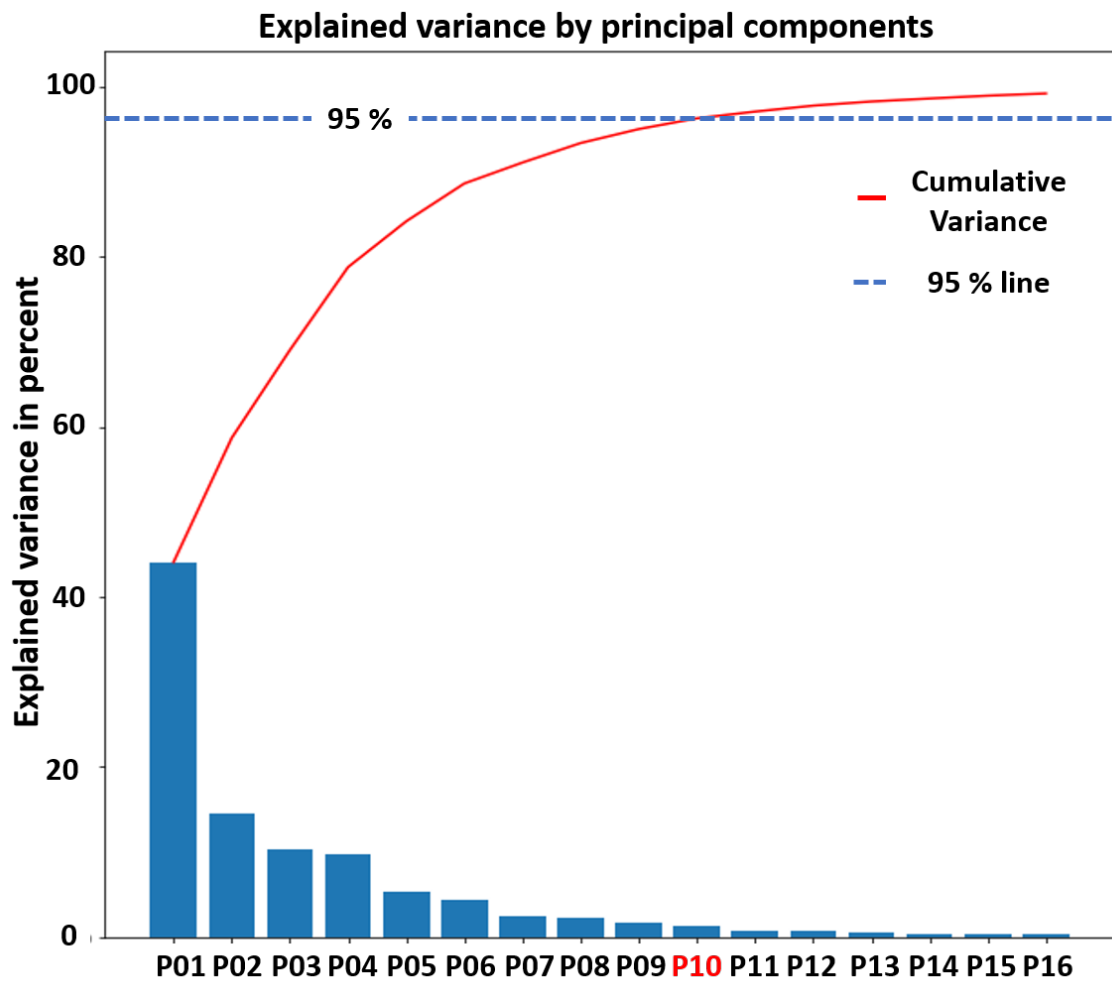
Figure 2.11: Explained variance by principal components. The x-axis represents the principal components listed in order by the percentage of variance they explain. The y-axis shows both the explained variance from the individual principal component as the blue column and the cumulative variance in the red curve.

2.8   Cortical Architectural Specific Anomaly Detection

In general, anomaly detection algorithms are a class of algorithms used to identify rare or suspicious observations. There are two assumptions required when employing these models. Firstly, the majority of the samples within a data-set are normal (i.e. highly biased data-set). In other words, the resected neocortical tissue we are studying contains sparse abnormalities. Secondly, the normal instances form a distinct pattern defined by the attributes selected, while pathologies will be deviate from this pattern. Since the data is normalized to a common reference and many of the artifacts and inherent biases in the data are accounted for, deviant observations are likely to come from areas of abnormal tissue.

We have adopted a commonly used model in the machine learning domain, isolation forest. The isolation forest model effectively attempts to isolate each point in the data through a series of random partitioning. The isolation forest model isolates observations by selecting an attribute at random and then randomly selecting a split value between the defined maximum and minimum values of the selected attribute. In each iteration the maximum or minimum values are updated, this random partitioning is repeated until the point of interest is isolated. The general assumption made by the algorithm is that random partitioning of data would require fewer divisions for data points that are deviant (i.e. outliers) from the normal pattern defined by the data-set. Whereas, normal data points require many random partitions in order to isolate as they are seen within dense regions in the data space. The number of partitions required to isolate a point can be treated as a distance measure which can be used to calculate an anomaly score. As with other outlier detection methods, the anomaly score is required to decide normal observations from anomalies. The isolation forest model was used to detect whether an observed profile across subjects was normal versus abnormal. Each profile was described by 10 principal components as described in the section above. Abnormal profiles were defined as regions in which the cytoarchitecture are deviant from the majority of the data (i.e. normal data). We applied this anomaly detection algorithm to each parcellated region as described in the Morphological Clustering section and evaluated the detected anomalies.

SubjID	Sex	Age	Surgery Side	Neocortical Histopathology	Neo FCD	Hippocampus Histopathology	MRI: MTS	MRI: FCD	MRI: Other
15	F	40	R	GM	-	MTS	R	-	parieto-occipital porencephaly
16	F	25	L	GO	-	G	N	-	-
21	M	20	L	GM	-	MTS	L	-	-
22	M	18	R	GM	-	G	R*	-	-
24	F	48	L	G	-	MTS	LR	-	-
27	F	41	R	G	-	G	R	-	-
31	M	31	R	GM	-	normal	-	-	-
32	F	49	R	G	-	MTS	R	R temporal lobe FCD *	blurred temporal pole
33	F	32	L	G	-	MTS	L	-	-
34	F	56	R	GO	-	G	-	-	-
35	F	43	R	G	-	MTS	R	-	-
36	M	39	R	GF	FCD 1b	G	-	-	polymicrogyria bi-lateral perisylvian*
37	M	23	L	GMEF	FCD 1a	GME	-	-	normal
40	M	34	L	GM	-	MTS	L	-	-
41	F	20	R	GM	-	MTS	R	-	-
43	F	33	R	G	-	MTS	R	-	-
46	F	58	R	G	-	MTS	R*	-	-
51	M	58	R	GO	-	G	-	-	-
58	F	28	-	-	-	-	L	-	-
66	M	53	L	G	-	MTS, O	L	-	-
70	M	21	L	GM	-	G	-	-	normal
78	F	21	R	G	-	GM	-	R amygdala FCD *	-
79	M	27	R	FO	FCD 3a/b	MTS	-	-	R.T. DNET*
81	M	18	L	GMEO	-	G	-	FCD	R. T. arachnoid cyst
83	M	42	L	G	-	G, MTS*	L	-	-
84	F	28	R	GMEO	-	GE	-	-	normal
85	M	21	L	GE	-	GE	-	-	normal

Table 2.1: Summary of demographics and clinical data including sex, age, handedness, seizure origin, histopathological and MRI findings in the neocortex and hippocampus. histopathology abbreviations are as follows: **G**-gliosis, **M**-minor architectural abnormality, **E**-electrode scar, **F**-FCD, **O**-other

Chapter 3

Results

3.1   Histological Quantification of Cortical Architecture

Feature maps describing neuron cell density, cell size, and eccentricity were obtained across multiple subjects and slides (N= 53 slides). Figure 3.1 illustrates an example of the NeuN stained image and the corresponding extracted features. In total, there were 27 patients selected for analysis in this study. Inclusion of these subjects was determined based on the availability of histology with few or no processing artefacts. The extracted feature maps were generated from the high-resolution NeuN stained images using the automated neuron segmentation results and a patch-based analysis. From each 100μm x 100μm patch summarized measurements were obtained. For example, the neuron density feature map (Figure 3.1 b) represents the number of neurons found within each 100μm x 100μm patch, yellow regions represent high neuronal density, whereas blue represents low neuronal density.

Figure 3.1 c) shows the obtained average neuron cell size feature map summarized from the 100μm x 100μm patch-based analysis across a whole slide example. Notably, areas with high neuronal density (layers II and IV) which also are known to have low average neurons size are seen in examples in Figure 3.1 b) and Figure 3.1 c), as high and low-intensity regions respectively. This suggests that the features selected can accurately summarize and depict the
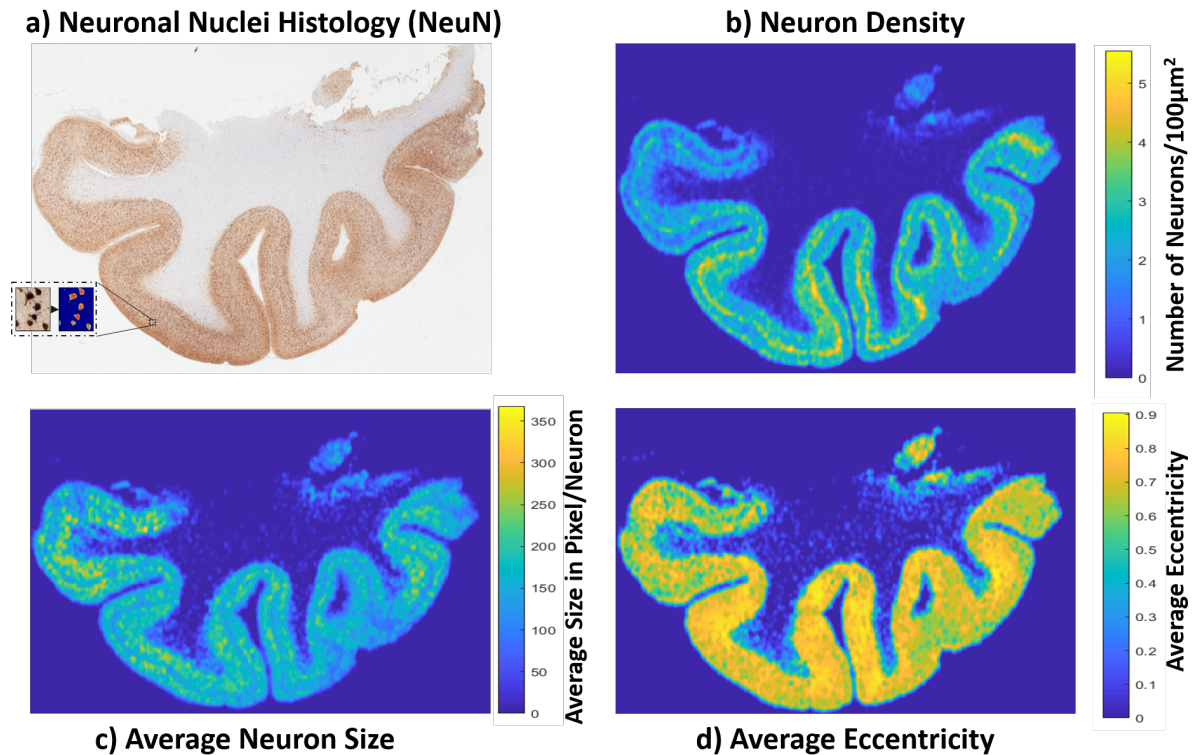
Figure 3.1: Example of feature maps generated from **a)** Neuronal Nuclei stained image for **b)** Neuron Density **c)** Neuron cell size, and **d)** Eccentricity. Feature maps were generated from averaged values within 100μm patch.

cortical layers. Eccentricity maps, which summarize the average circularity of neuron cell bodies with the 100μm patches are illustrated in Figure 3.1 d). The eccentricity maps are represented as a scalar between 0 and 1 for each neuron, 0 representing a perfectly circular neuron and 1 representing an ellipse.

The central theme illustrated in Figure 3.2 when comparing the NeuN stained image to the extracted feature maps, is that the extracted features are sensitive to the changes in cortical architecture. In particular, Figure 3.2 illustrates slide examples in which there are subtle and drastic cortical architectural deformities, which can be seen in the extracted features. Examples include the presence of vasculature (Figure 3.2a), substantial and subtle focal reduction of neuronal density (Figure 3.2b-c) compared to the surrounding tissue, and presence of obliquely sectioned cortical region (Figure 3.2d).
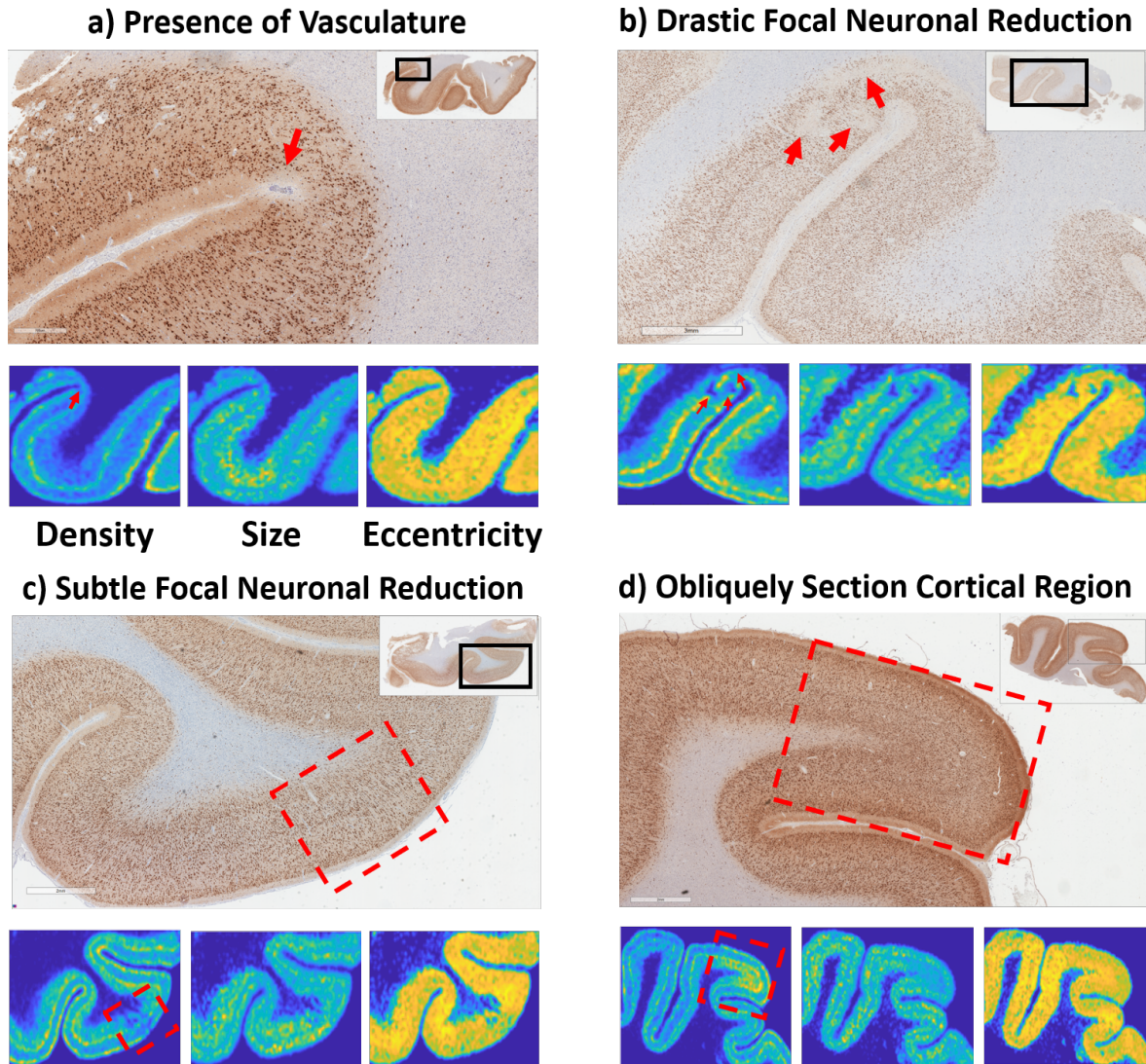
Figure 3.2: Examples of cortical slide with **a)** presence of vasculature, **b)** Drastic focal neuronal reduction highlighted with red arrows, **c)** Subtle focal neuronal reduction **d)** obliquely sectioned cortical regions. Extracted feature maps are shown on the bottom of each example, illustrating how the extracted features summarize and represent these subtle and gross changes in cortical architecture.

3.2 Cortical Coordinate Extraction

3.2.1 Laplacian Derived Coordinate System

From the Laplacian solution, we derived radial streamlines that were used to define a coordinate system suitable for sampling cortical laminae. In particular, the defined coordinate system allows sampling along the cortical depth from the pia to CWM junction and along the length of cortical tissue being examined. Figure 3.3 a-c) shows examples across three subjects of the

equi-potential derived streamlines overlaid on top of the density feature maps. These stream-
lines can be represented as a three-dimensional coordinate system, Figure 3.3 d) shows an
example of the extracted profiles from the example in Figure 3.3 c). The colour of the stream-
lines in Figure 3.3 represents the ordering of the streamlines, where white streamlines indicate
the beginning of the cortical ribbon and black represents the end.
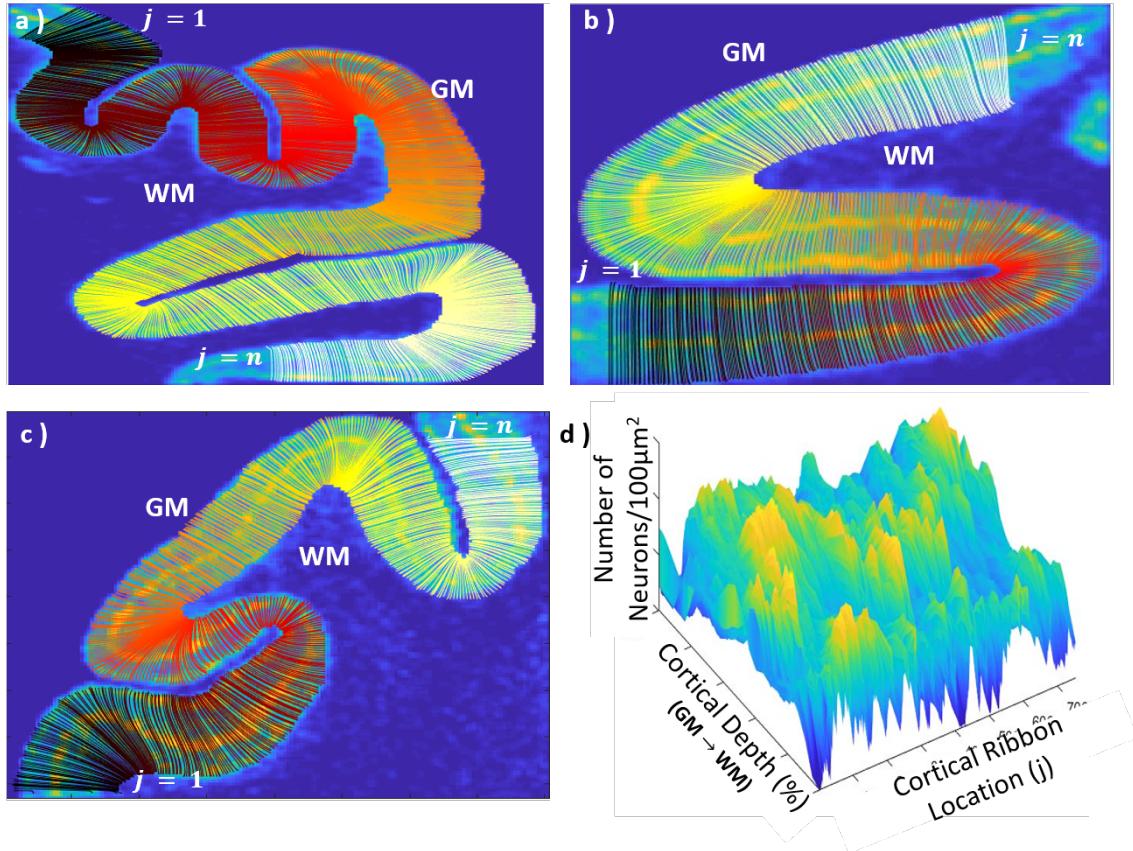
Figure 3.3: Coordinate system examples **a)-c)** show examples of equ-potential streamlines laid on-top
of feature maps across 3 subjects. The streamline colour represents the order of streamlines j=1 (black),
whereas j=N (white). **d)** Labeled coordinate system and extracted profiles from example c)

3.2.2 Sampling Cortical Lamina & Correction

From the obtained feature maps and equi-potential derived coordinate system, it was possible
to extract cortical profiles which define relevant laminar characteristics of the cortical slides.
The examples in Figure 3.4 show three individual samples with different degrees of cortical
folding. As mentioned previously, the degree of distortion seen in the extracted profiles is

dependent on the degree of cortical folding. Furthermore, Figure 3.4 shows examples of the original distorted extracted density profiles and corrected profiles using the iso-area and iterative warping correction technique. The rows in the profiles in Figure 3.4 represent cortical depth, whereas the columns represent location along the length of the tissue. In comparing the corrected profiles relative to the original profiles, it is clear from the examples in Figure 3.4 that the columns within-subjects show better agreement along the cortical profiles after performing our two step correction.
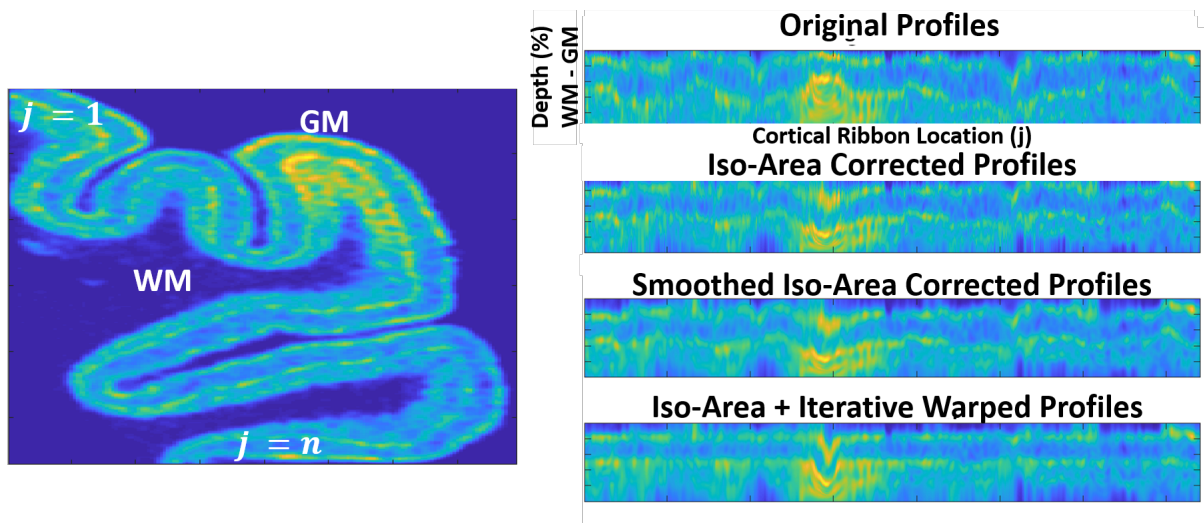
(a) Subject P085 density feature map and extracted uncorrected and corrected profiles
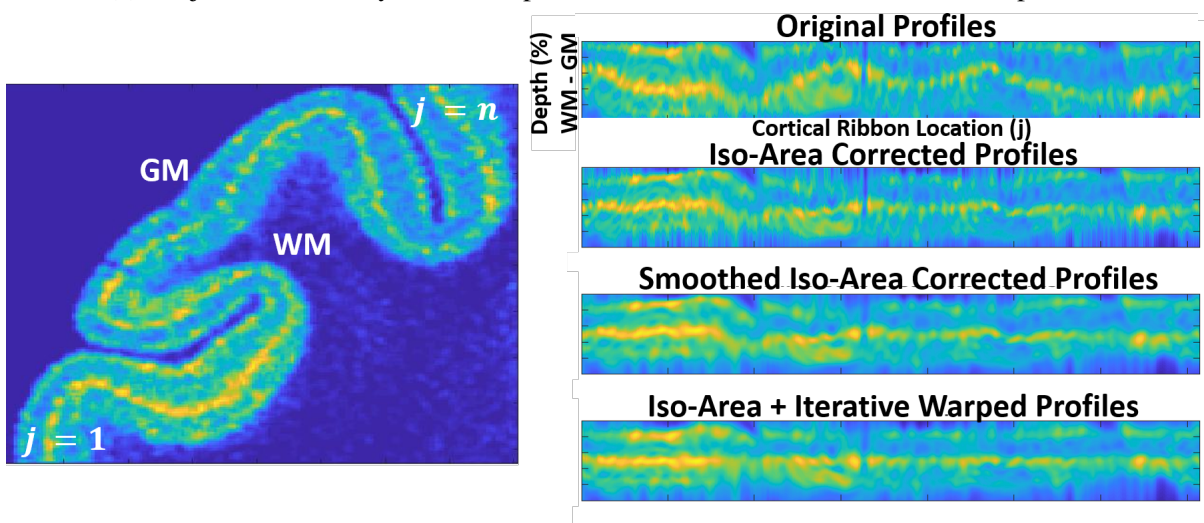
(b) Subject P040 density feature map and extracted uncorrected and corrected profiles

Figure 3.4: Examples of extracted cortical laminae before and after correction.

Profiles were also obtained from the size and eccentricity maps. To account for the distortions seen due to cortical folding, the transformations applied to the density profiles were applied to the size and eccentricity profiles. Figure 3.5 and Figure 3.6 show examples of the originally extracted profiles before applying the necessary transformations and after applying the corrective transformations for both the size and eccentricity maps.
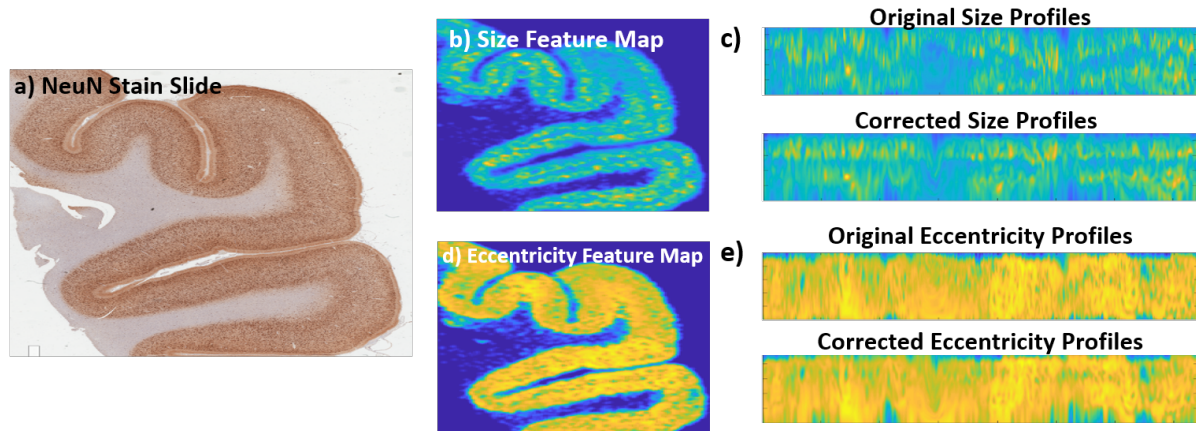
Figure 3.5: Example of cortical layer alignment for size and eccentricity feature maps. **a)** Original NeuN stained slide (Subject P085). **b)** Size feature map **c)** Original and corrected extracted neuronal size profiles **d)** eccentricity feature maps. **e)** Original and corrected extracted eccentricity profiles.
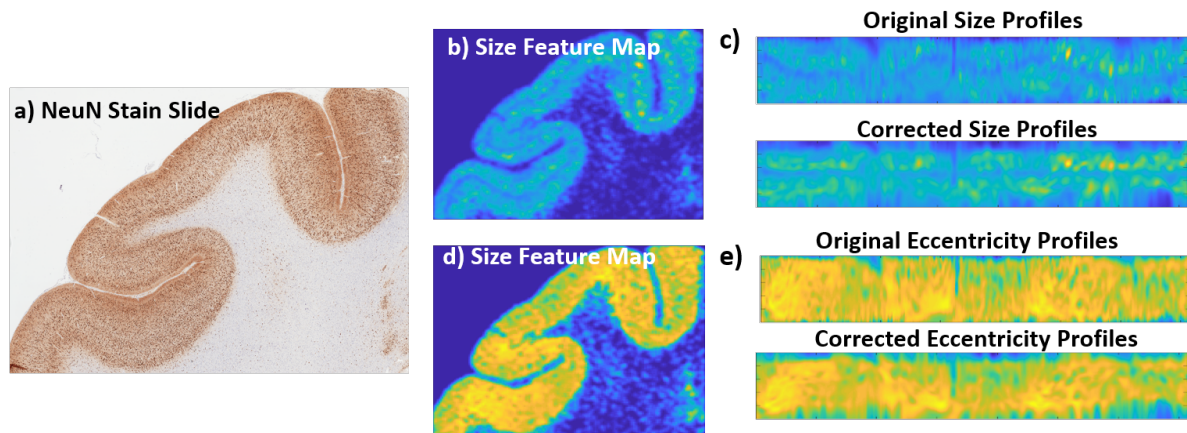
Figure 3.6: Example of cortical layer alignment for size and eccentricity feature maps. **a)** Original NeuN stained slide (Subject P040). **b)** Size feature map **c)** Original and corrected extracted neuronal size profiles **d)** eccentricity feature maps. **e)** Original and corrected extracted eccentricity profiles.

A summary figure showing the aligned profiles across subjects for the neuron density, size, and eccentricity is shown in Figure 3.7. The profiles in Figure 3.7 were normalized to a common reference across subjects and between feature maps.
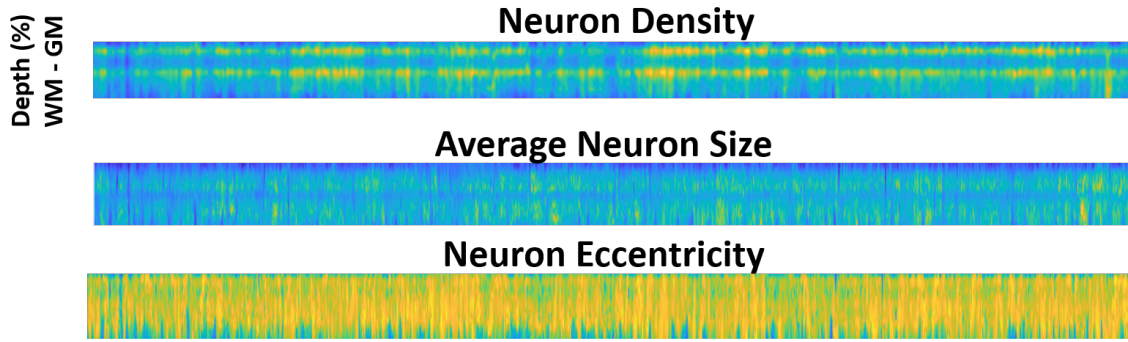
Figure 3.7: Alignment across subjects for density, size and eccentricity profiles.

3.2.3 Validation of Cortical Lamina Alignment

To validate the quality of the layer alignment, we evaluated the average profiles in the uncorrected and corrected space across 4 slide examples. Figure 3.8 shows the original density feature maps, the extracted uncorrected profiles, the corrected profiles and their respective average profiles across multiple subjects. The average profiles are shown in the black curves, and
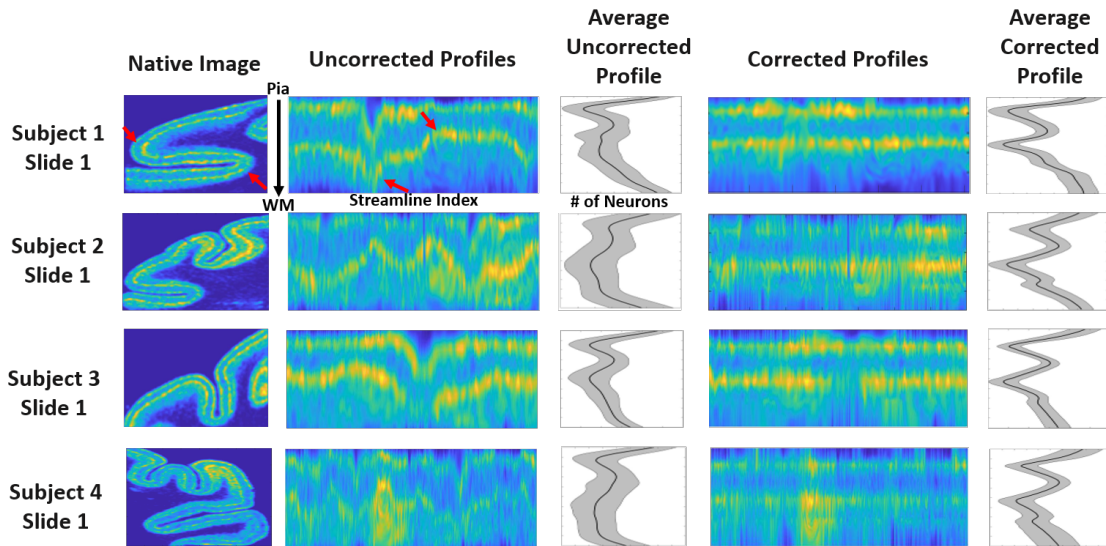
Figure 3.8: Alignment correction results across multiple slides and subjects registered to a common reference. Native Images represent neuron density feature maps. Red arrows show an example of the cortical folding distortion on the extracted profiles and density feature map.

the variation along these curves is shown in grey for each slide. It is important to note that the corrected profiles in the examples in Figure 3.8 are normalized to a common reference. This can be seen from the fact that the highly dense regions in the profiles, layers II and layer IV, occur at relatively the same location across these examples. The distortions seen in the un-

corrected space contribute to a greater variance in the average profile, this ultimately leads to smoothing of characteristic profile shape features, such as smoothing of peaks corresponding to layers with high density neurons. Ideally, the average profile from the neuron density feature map, if aligned, will have 2 peaks, which correspond to the highly dense granular neuronal layers II, IV. We can see that once the distortions are corrected, the average profile results show relatively less variation and sharper peaks in the profile shape, suggesting global agreement across individual profiles.

Figure 3.9 illustrates distributions of euclidean distances between the average profiles and individual profiles across all subjects before (red) and after corrections (blue). Notably, prior to extracting the distances, the profiles were separated based on their cortical thickness measures. Figure 3.9 shows the distribution before and after correction for profiles with low cortical thickness Figure 3.9 a), whereas the Figure 3.9 b) and Figure 3.9 c) depict distributions for profiles with medium and high cortical thickness respectively. Using a paired-sample t-test, the results within each thickness group showed a significant decrease (p <0.01) in distances between the average profile in each bin and individual profiles across subjects. This can be seen in Figure 3.9 as a shift to the left in the blue distribution corresponding to the corrected data, suggesting that there is a higher similarity between the data and the average trend within each bin after applying the correction.
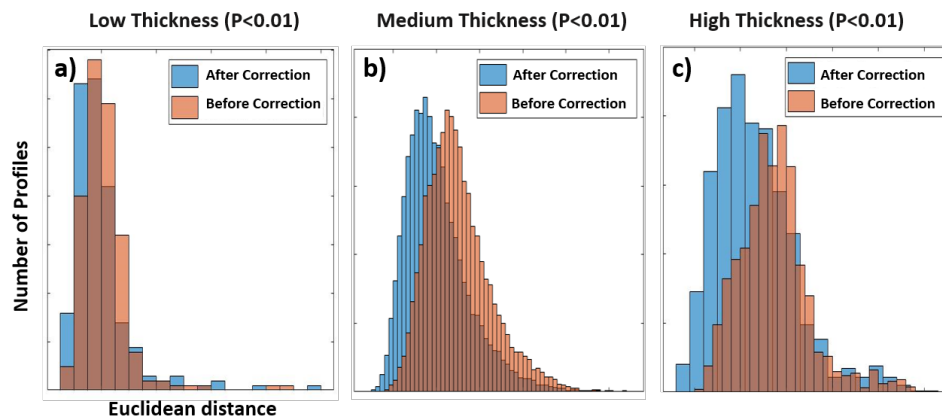
Figure 3.9: Distribution of Euclidean distances between average profile and individual profiles across all slides (n=53) with: **a)** Low, **b)** Medium, and **c)** High Thickness Before (red) and After Correction (blue).

3.3   Morphological Clustering

Cortical thickness and curvature metrics were defined for each sample and were used as features in the morphological clustering. Figure 3.10 b) and Figure 3.10 c) illustrate examples of the extracted cortical thickness and curvature measures respectively. Figure 3.10 a) illustrates the original cortical slides which the thickness and curvature metrics were extracted from. The cortical thickness was defined as the pathlength of an individual streamline, and these streamlines can be seen in the second column in Figure 3.10 b). The colour of the individual stream-
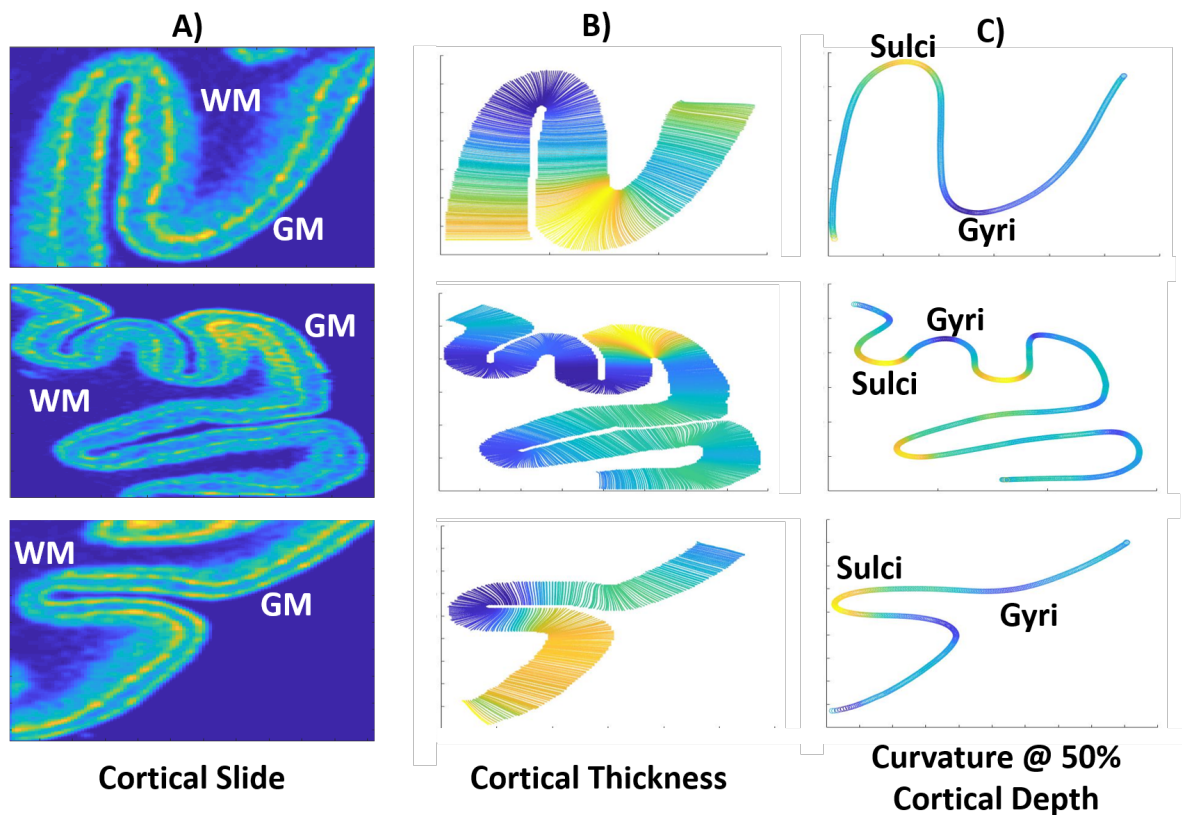
Figure 3.10: Example of cortical thickness and curvature measures across three cortical slides. **a)** Corresponding cortical slides shown as neuron density feature maps. **b)** Cortical thickness measure results displayed as a colour map on top of individual streamlines. **c)** Cortical curvature along 2D curve at 50% depth along the cortical tissue. Colour of the individual point along the 2D curve is indicative of the instantaneous curvature at the point.

lines indicate the length of the streamline, high cortical thickness is represented by the colour yellow and blue for low cortical thickness. The curvature was defined as the instantaneous curvature along the 2D curve at 50 % depth along the cortical tissue. The extracted curve is

shown in the third column in Figure 3.10 c). The colour along the curve indicates the resulting curvature, yellow indicate high positive curvature, whereas the dark blue represents negative curvature. The cortical thickness and curvature results followed expected trends as described in section 2.6.

The normalized cortical thickness and curvature across subjects were used to perform the morphological clustering using k-means (k=4). The normalized clustered data can be visualized in Figure 3.11 c). In addition, the silhouette plot for the various clusters is shown in Figure 3.11 b). The silhouette coefficient was used to interpret and validate the consistency, within clusters, of the data. In general, the silhouette coefficient ranges from -1 to 1. High values indicate points are well matched to that particular cluster and poorly matched to neighbouring clusters. The average silhouette coefficient was 0.393. Despite this value being on the lower end, the morphological clustering effectively identifies the regions of interest (Figure 3.11 a). Figure 3.11 a) illustrates the resulting segmentation from the morphological clustering, which aims to identify the gyri, sulci, straight cortex, and oblique sectioned areas.
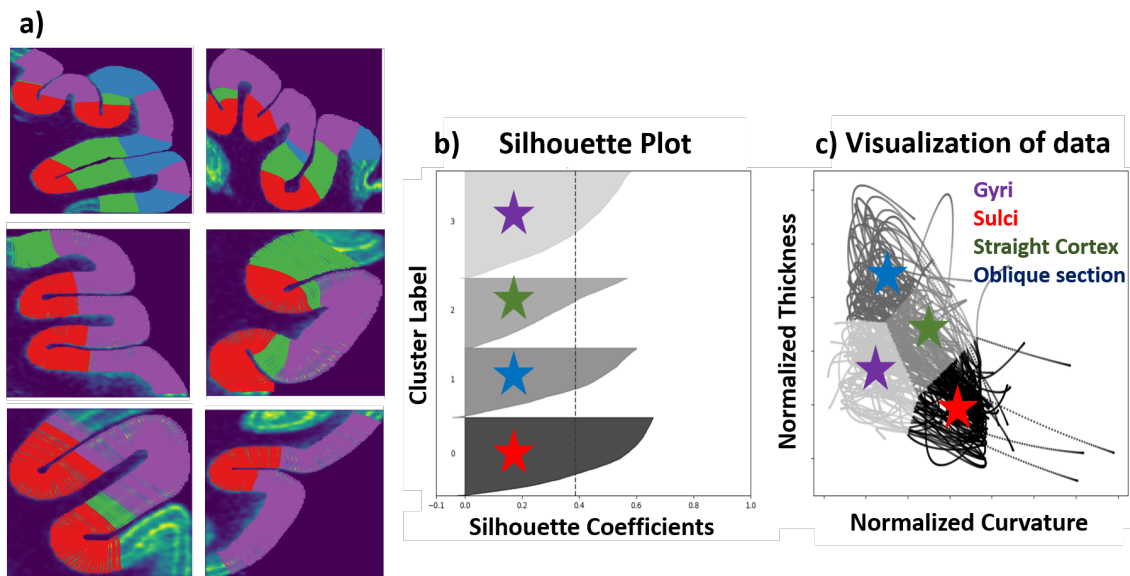
Figure 3.11: Example of morphological clustering using k-means clustering (k=4). **a)** Segmentation results across multiple cortical slides. **b)** Silhouette plot from the k-means cluster (Silhouette score = 0.393). **c)** Visualization of the normalized thickness and curvature data across all subjects. The gyri, sulci, straight cortex, and oblique section regions are illustrated by the colors purple, red, green, and blue respectively.

3.4 Dimension Reduction

3.4.1 Profile Shape Feature Extraction

We extracted laminar profiles along the Equi-potential laminar solution and then summarized these profiles using the same 10 profile shape features consistently used by Amunts et al. (1999) [85]. The resulting data is illustrated in Figure 3.12. In total there were 30 features, 10 from each feature map. Features describing density profiles are shown in red, area in green, and eccentricity in blue. The high-dimensional representation of the data in Figure 3.12 revealed a high correlation between several features describing profile shape within feature maps but also between feature maps (Figure 3.13 a). The uncolored regions of this figure illustrate the relationships of the data between the profile shape features across feature maps.
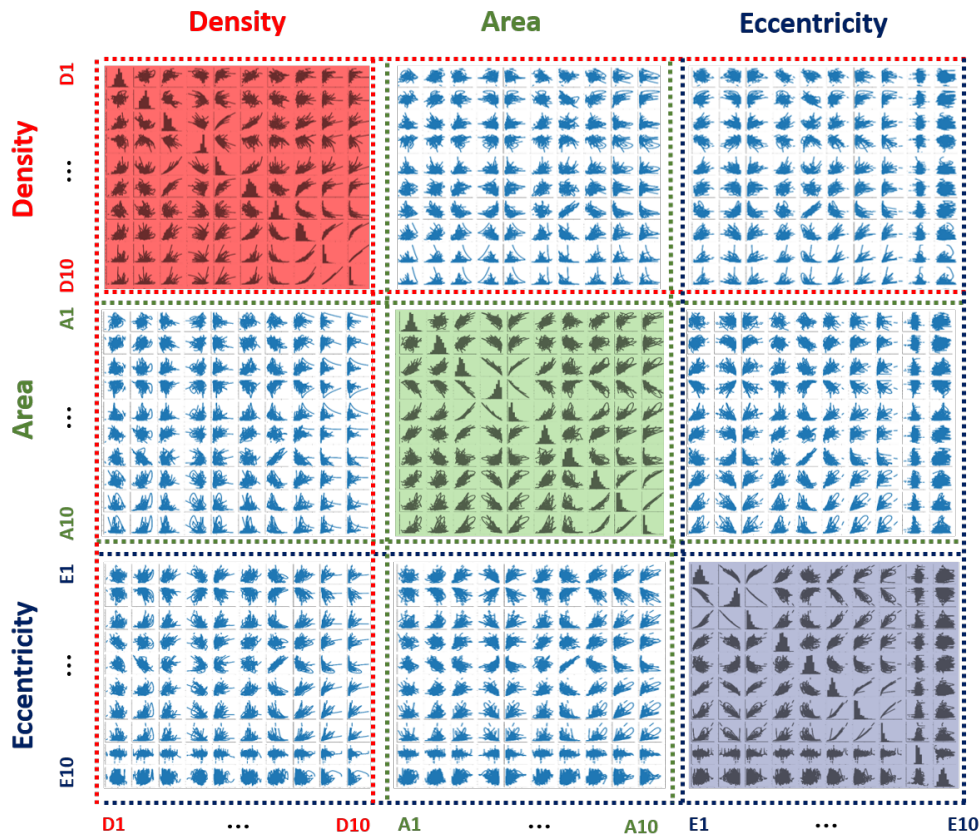
Figure 3.12: Visualization of data after profile shape feature extraction. In total there were 30 profile shape features across 3 feature maps, profile features describing density feature maps are shown in red, area in green, and eccentricity in blue.

3.4.2 Principal component analysis

Of the features used in this analysis, many were highly correlated with each other (Figure 3.13a). As a result, the data from Figure 3.12 was reduced to 10 dimensions using principal component analysis, which preserved 95% of the original data variation. Figure 3.13 b) shows the high dimensional representation of the data after applying PCA, which ultimately reduced the dimensions, noise, and redundancies in the data. The diagonal of Figure 3.13 illustrates the one-dimensional distribution of the individual components using the kernel density estimation (KDE) plots. Comparing the data from Figure 3.12 and Figure 3.13, it was evident that the resulting data showed weaker correlations and the distributions were more normally distributed.
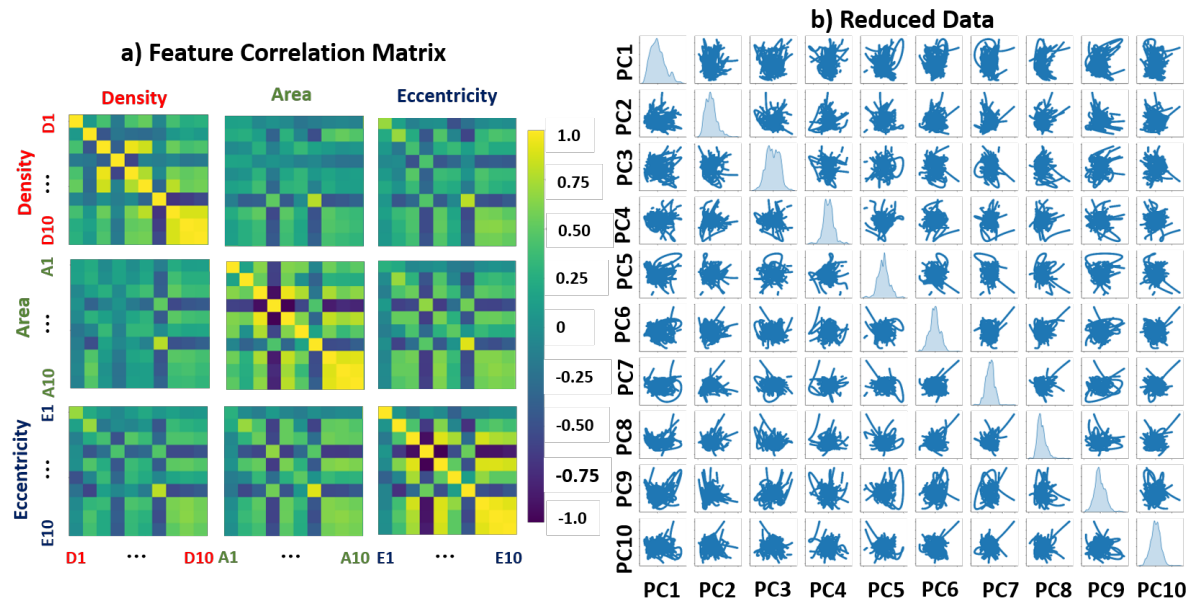
Figure 3.13: High dimensional representation of data after applying principal component analysis. The diagonal of the pair-plot illustrates the one-dimensional distribution using the kernel density estimation (KDE) plots.

In order to better understand the anatomical meaning of the principal components, we examined the average loading's of the original features for each principal component (Figure 3.14). Specifically, the absolute weighting across the features describing each feature map (i.e. density, area, eccentricity) were averaged for each principal component and plotted using a radar plot. The first and most prominent component which explained 42.6% of the data's variation

was roughly weighted equally among the metrics describing density, area, and eccentricity, with a slightly higher weight on the area and eccentricity metrics. In other principal component examples, we do not see this equal weighting, as one feature tends to dominate the weighting of the principal component. For example, principal components 2, 3, 5, and 8 seem to be dominated by features describing the density profiles. Whereas, principal components 4, 6, and 9 are dominated by features describing area and 7, and 10 are weighted more by features describing eccentricity metrics.

Figure 3.14: Principal component loadings illustrating the absolute average weightings of the profile shape features for each principal component.

3.5 Anomaly Detection

Briefly, the goal of this section was to detect abnormal profiles from the data across subjects within each sub-region and to evaluate whether the anomalies in the data resembled abnormalities in the cortical slides. In order to reduce the unwanted morphological differences in the data, the anomaly detection algorithm was applied to each parcellated region as determined from the morphological clustering. As an example, Figure 3.15 a) illustrates the data found within the straight segments of cortex, the colours represent observations grouped as either anomaly (blue) or normal (orange). As expected, the isolation forest algorithm was able to detect observations that were deviant from the dense regions of the data (Figure 3.15 a). This general trend was also observed for the data across each parcellated region (gyri, sulci, and straight cortex regions). Figure 3.15 b) illustrates and summarizes the proportion of anomalies found within each slide within straight segments of cortex. In addition, a summary of the histopathological clinical data, the percentage of anomalies detected within each sample, and the total number of profiles within each sample is summarized in table 3.1. The results revealed that the majority of the slides contained no or very few (0-10%) anomalies. However, there were a few exceptions which were further investigated.
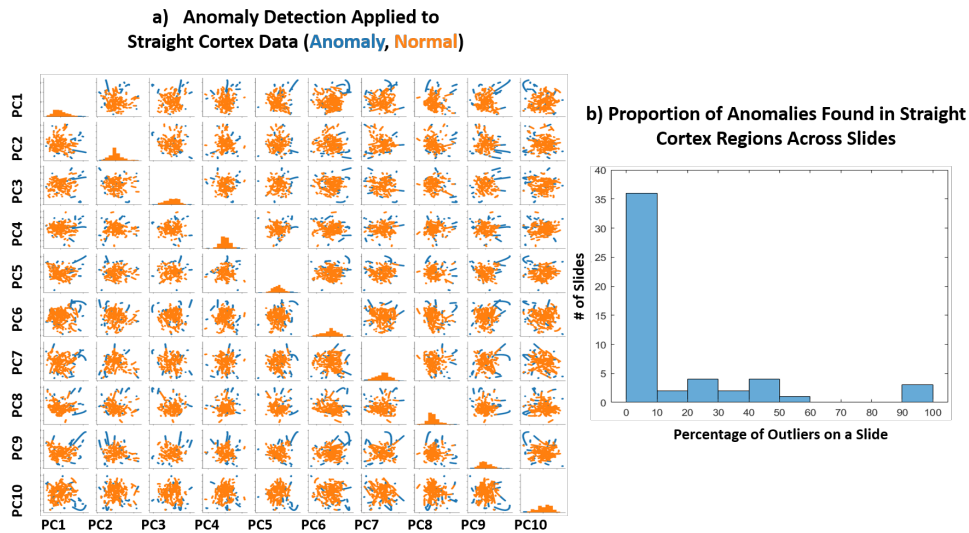
Figure 3.15: **a)** Visualization of the data after applying the anomaly detection algorithm to the parcellated region. Note blue observation represent detected anomalies in data and orange is the normal observations. **b)** Distribution of the proportion of anomalies found within straight segments of cortex.
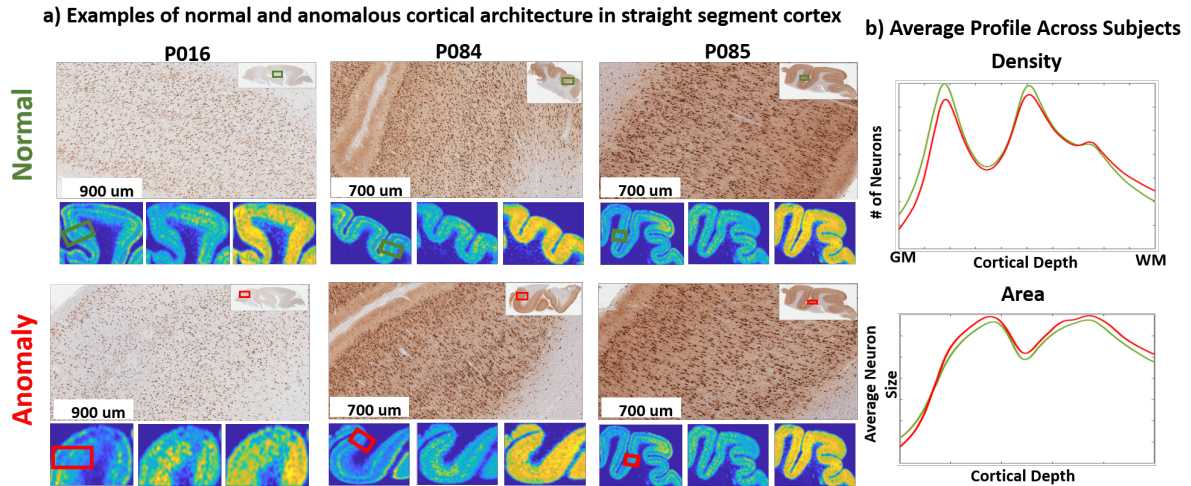
Figure 3.16: Examples of normal and anomalous cortical architecture at gyral segments.**a)** Illustrates the comparison of abnormal regions within subjects. Examples include histological slide images and the associated extracted features: neuron density, average neuron size, and eccentricity maps. **b)** Average Neuron density and size profiles for normal and abnormal cases in the sulcal cortical regions.

We investigated the histological samples in addition to the extracted features (Figure 3.16-3.18 a) for samples with a high percentage of anomalies. Figure 3.16 a) illustrates areas within cortical samples in which the algorithm detected as either a normal region (top row) or an anomaly (bottom row) within segments of straight cortex. Comparisons between normal and abnormal cortical areas were made within the same subject as shown in the columns of Figure 3.16 a). A general trend we saw from the feature maps from these examples was that regions detected as anomalous tended to have decreased neuronal density with increased average neuron size compared to the normal counterpart. Note that these trends were not obvious when visually evaluating the original histological images. Inspection of the average profiles across slides from the straight cortical segments (Figure 3.16 b) revealed similar trends as to what was shown from the visual inspections from the feature maps — a decrease in neuronal density and an increase in neuronal size. However, the profiles in Figure 3.16 b) tended to deviate from the overall observed trend near the cortical boundaries. These deviations may be due to the variability caused by the quality of our segmentations and the stretching and compressing from our iterative warping technique.

a) Examples of normal and anomalous cortical architecture at sulcal depths

b) Average Profile Across Subjects
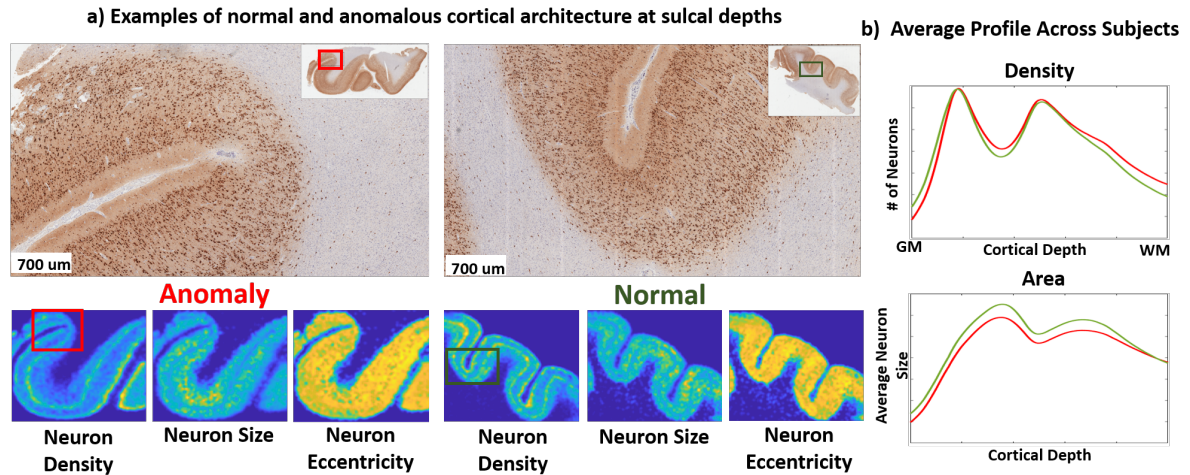
Figure 3.17: Example of normal and anomalous cortical architecture at sulcal depths. **a)** illustrates comparison of abnormal regions within subjects. Examples include histological slide images and the associated extracted features: neuron density, average neuron size, and eccentricity maps. **b)** Average Neuron density and size profiles for normal and abnormal cases in the sulcal cortical regions.

A comparison between normal and abnormal cortical areas in the sulci region is illustrated in Figure 3.17 a). The comparison is made between cortical sections within the same subject (P084), the figure depicts both the histological slide and extracted feature maps for both examples. An interesting observation that can be seen from the histological slide in the anomalous example is that there is vasculature within the sulcal region, which is not present in the normal example. The presence of the vasculature seems to affect the feature maps in this region, as shown in the neuronal density, size, and eccentricity feature maps. Ultimately, the presence of an extraneous structure, such as a vein or artery, can affect the extracted profiles in these regions, which could be a significant reason for the profiles being classified as abnormal. Furthermore, it was clear that the anomalous example had diminished neuronal density compared to the normal example, as seen in the feature maps and the histological slide. On average, the average neuron density profile showed a slight increase in density, while the average size profile showed a decrease in the anomalous observations.

a) Examples of normal and anomalous cortical architecture at gyral segments

Anomaly

Normal

Neuron Density Map

Neuron Size Map

Neuron Eccentricity

b) Average Profile Across Subjects

Density

# of Neurons

GM   Cortical Depth   WM

Area

Average Neuron Size

Cortical Depth
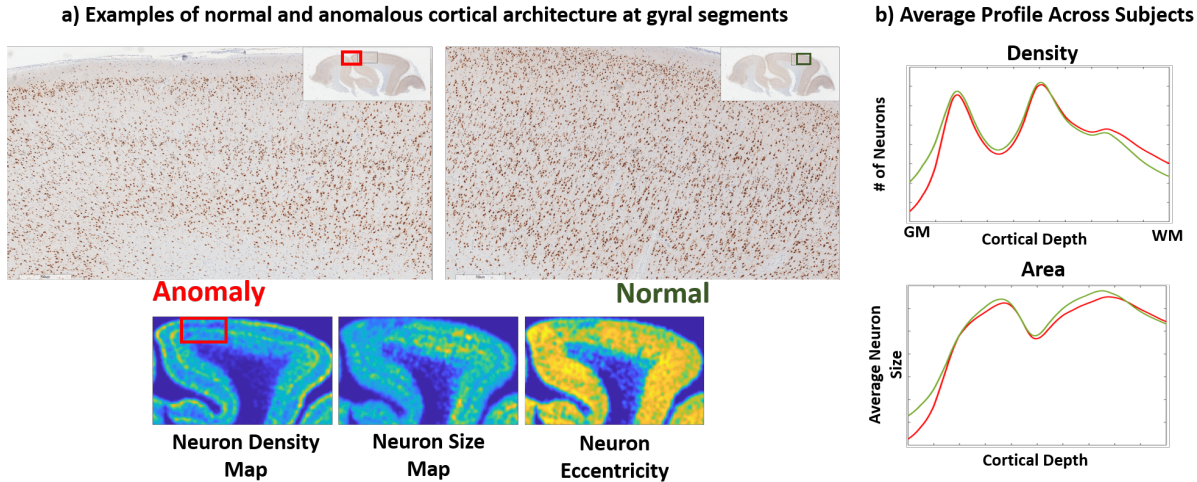
Figure 3.18: Example of anomaly detection in gyral cortical regions.**a)** Illustrates the comparison of abnormal regions within subjects. Examples contain histological slide and the following extracted features: neuron density, average neuron size, and eccentricity maps. **b)** Average neuron density and size profiles for normal and abnormal cases in the sulcal cortical regions.

The comparison of the two groups in Figure 3.18 also revealed a decrease in neuronal density in the region classified as abnormal. Interestingly, the changes in neuronal density can be visually identified when comparing the two histological images. Evidently, the corresponding feature maps showed a decrease in neuronal density, area, and eccentricity in the identified abnormal region compared to its normal counterpart. These results suggest that the extracted feature maps are sensitive to these gross changes seen visually in the histological images, and these changes can be identified as anomalies in the data. Examination of the average profiles in Figure 3.18 b) showed a slight decrease overall in the density and the average neuronal size profiles, with the exception of areas near the cortical boundaries. This trend was in agreement with what was observed in the above example.

In order to evaluate the two groups, more precisely, we compared the average principal component weight for each group and sub-region (Figure 3.19). Notably, the first and most prominent principal component, which explained 42.6% of the variance, showed the most difference between the two groups across sub-regions. The first principal component was roughly weighted equally among the metrics describing density, area, and eccentricity, with a slightly higher weight on the area and eccentricity metrics (Figure 3.14). Suggesting that all three
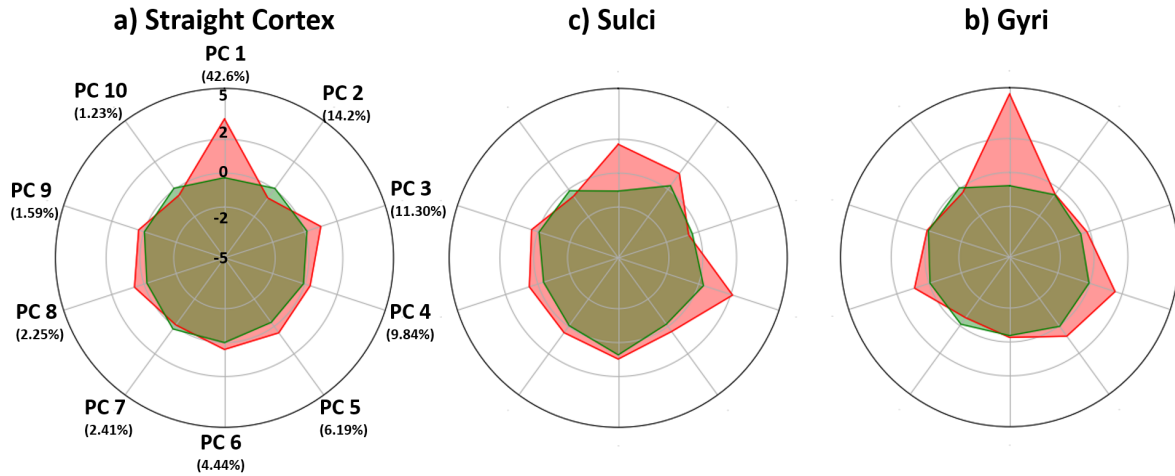
Figure 3.19: Radar plots comparing the average principal component weight for each group and for each sub-region: a) straight, b) sulcal, and c) gyral cortical regions. The normal group shown in green and red for the anomalous data

features were crucial in determining differences seen between the two groups. principal components 2 and 4 were weighted heavily on metrics describing density and area, respectively (refer to Figure 3.14), with an explained variance of 14.2% and 9.84% respectively. The principal components 2 and 4 also showed notable differences between the groups and among the sub-regions. Overall, as expected, these results indicate that there was not one anatomical feature that drove the differences between the two groups, but the amalgamation of these features.

Subject ID	No. of Slides per Subject	Histopathology	FCD	Other Pathology	Perc. of Anomalies per Slide (%)	No. Of Profiles per Slide
15	1	GM	-	-	0	368
16	1	GO	-	atypical cells in WM	69.3	659
21	3	GM	-	-	0, 0, 33.1	864, 887, 454
22	1	GM	-	-	0	270
24	1	G	-	-	12.1	214
27	2	G	-	-	24.1, 0	315, 449
31	1	GM	-	-	0	117
32	2	G	-	-	0, 12.1	213, 380
33	3	G	-	-	21.7, 0, 8.6	304, 477, 994
34	2	GO	-	arteriosclerosis	0, 0	450, 509
35	1	G	-	-	0	362
36	3	GF	FCD 1b	-	0, 30.4, 14.8	813, 880, 826
37	1	GMEF	FCD 1a	-	7.6	476
40	3	GM	-	-	36.7, 0, 0	714, 286, 972
41	2	GM	-	-	11.5, 100	305, 143
43	2	G	-	-	0, 31.4	377, 455
46	2	G	-	-	13.1, 15.1	712, 636
51	3	GO	-	cortical scar	25.2, 35.6, 0	610, 447, 483
58	3	?	-	-	0, 0, 0	829, 520, 395
66	3	G	-	-	16.1, 0, 0	442,72, 235
70	1	GM	-	-	100	161
78	2	G	-	-	0, 0	372, 316
79	3	FO	FCD 3a/b	glioneuronal tumour	8.8, 5.8, 0	725, 599, 545
81	2	GMEO	-	gangliocytoma	0, 0	304, 662
83	2	G	-	-	42.4, 0	401, 304
84	2	GMEO	-	leptomeningeal fibrosis	0, 100	622, 121
85	1	GE	-	-	35	1157

Table 3.1: Summary of histopathological clinical data, the percentage of anomalies detected within each sample, and the total number of profiles within each sample. histopathology abbreviations are as follows: **G**-gliosis, **M**-minor architectural abnormality, **E**-electrode scar, **F**-FCD, **O**-other

Chapter 4

Discussion

4.1   Thesis Contributions

In our work, we have utilized a feature extraction tool to extract relevant features associated with cortical architectural abnormalities and created a coordinate system for sampling cortical laminae in 2D histological data. The features extracted showed sensitivity to subtle changes in the cortical slides relevant to the detection of architectural abnormalities. We developed an innovative method to normalize our data across samples to reduce inherent anatomical biases affecting the detection of cortical architectural abnormalities. These artifacts include cortical layer distortions and morphological differences caused by cortical folding effects, as well as processing artifacts. This framework was then applied to detect abnormalities across multiple subjects and cortical samples using an unsupervised anomaly detection algorithm. The results suggest that the technique is able to identify anomalies that correspond to visually-identifiable histo-architectural irregularities. The frequency of abnormalities was found to differ among patients; however, the clinical significance of these findings is yet to be investigated.

4.2   Histological Quantification

High-resolution neuronal nuclei (NeuN) stained cortical slides can provide extraneous detail about the cortical architecture, which makes quantitative and qualitative evaluation of the slides challenging to interpret when determining whether a specific pathology is present within the tissue sample. Summarized features can represent the relevant cortical architectural qualities of interest; ultimately reducing the irrelevant information and making qualitative and quantitative evaluation more efficient, sensitive, and specific [96]. Prior studies have noted the importance of neuronal density, size, and morphology when evaluating focal cortical dysplasias in the neo-cortical slides [108, 109, 42]. In fact, one study has shown significant differences in the mor-phological parameters such as neuronal density, size, cortical thickness, and grey-white matter boundary clarity when evaluating the different ILAE classification of FCD [42]. However, their methodology presents a semi-quantitative approach in assessing cortical tissue slides, and further work is required to accurately measure whole slide cortical tissue in histology samples. In our study, we utilize a fully automated approach that is capable of characterizing whole sections of cortical tissue and focused on assessing the neuronal size, density, and eccentricity feature maps [101]. When evaluating the quality of the images produced in the feature maps, both neuron density and size, provide clear images of cortical architecture, as shown in the example in Figure 3.1. In particular, layer II and IV are known to have high neuronal density and small average neuronal size, while layers III and V have the inverse characteristics. These regions with contrasting neuronal density and size are more clearly seen in the feature maps compared to the original histological image (Figure 3.1 a-b). The qualitative results provide evidence that layer architecture can be more easily represented and summarized using the ex-tracted feature maps, which is an important feature when assessing most types of FCDs with abnormal cortical layering [41, 3]. In addition, the feature maps were sensitive to both gross and subtle changes in architecture such as complete loss and subtle reduction in neuronal den-sity (Figure 3.2 a-b) and the effects of extraneous structures such as penetrating vessels (Figure 3.2 c), which mimicked an area of neuronal hypo-density. As mentioned in a previous study,

density was a significant feature in assessing several FCD sub-types [42, 3]. The sensitivity to the vasculature is also an important feature, as FCD III c are classified as cortical lamination abnormalities with the presence of vascular deformations. Finally, the finding in Figure 3.2 d) suggests that the feature maps are sensitive to oblique planes of sectioned regions and for this reason excluded from analysis using the morphological clustering technique (Figure 3.11).

4.3 Anomalies in Cortical Architecture and how they Relate to Histopathology

As shown in Figure 3.16 - 3.18, we found preliminary support for our hypothesis about anomalies in the data resembling abnormalities in histopathology. Specifically, we hypothesized that cortical architectural anomalies associated with epilepsy, would be structurally distinct from the surrounding healthy tissue and the selected features can identify these differences. In our study, we tested this hypothesis by performing an unsupervised anomaly detection algorithm to the corrected and extracted data and evaluated the histological regions corresponding to the detected anomalies. Overall, the results showed gross and subtle changes that can be quantified and visualized using the selected feature maps (as discussed in the section above) and that these changes can be identified as irregularities in the data-set. These included cortical regions with subtle (Figure 3.16) and clear (Figure 3.18) neuronal density reductions as well as the identifications of regions with focal cortical disruptions by non-neuronal elements. There were several identified anomalies with no apparent visual irregularities in either the feature map or the corresponding histology slide, suggesting that the method may be overly sensitive or that it can detect abnormal cortical regions beyond visual inspection. Whether these cases are false-positive examples or subtle architectural abnormalities, is unclear and further investigation is required.

Table 3.1 summarizes the histopathological data and the percentage of anomalies detected within each sample. Overall, the number of identified anomalies found within the FCD samples

was lower than expected and showed inconsistent trends compared to the rest of the samples. However, the frequency of the abnormalities was found to differ among patients and slides, and the identified anomalies corresponded to visually-identifiable histo-architectural irregularities (Figure 3.16 - 3.18). The inconsistency found within the results may be due to the variability in the data due to the presence of multiple pathologies, and remaining artifacts and interpretation of these results should be taken with caution. It is difficult to assess the clinical significance of this tool without quantitatively evaluating the performance of this tool compared to the ground truth annotations. The current study was limited by the lack of annotations of the identified pathologies.

4.4   Remaining Challenges & Limitations of Study

Our analysis was limited by the number of available samples. The lack of samples may have limited the power to observe differences between healthy and dysplastic tissue in our study. In addition, there was a lack of control tissue from non-epilepsy cases. The assumption that our study made was that the majority of the obtained samples contained normal cortical architecture and pathologies found were limited and occurred in localized regions of the cortical slides. However, in future investigations, it would be beneficial to include control tissue from non-epilepsy cases in order to represent the histopathological characteristics of healthy tissue better and thereby increase the accuracy and prediction of detection in pathological tissue. Our data-set also included a variety of cortical pathologies, which included of gliosis, and minor architectural abnormalities. Due to the presence of multiple pathologies, the results from our method must be interpreted with caution since the detected anomalies are more likely to be associated with other pathologies. In future studies, it would be beneficial to limit cases with a limited set of confirmed pathologies, thereby limiting the noise and variability seen within the data.

As mentioned in the literature review, the architecture of the layers differs from one cortical

region to another, in ways that are related to function [110]. Individual layers exhibit distinct cellular compositions and distributions [25], developmental trajectories [26], and functional roles [27]. Therefore, it is challenging to establish a clear distinction between healthy and dysplastic tissue, due to the cytoarchitectural heterogeneity of the different subregions within the anterior portion of the temporal lobe (e.g., Brodmann area 38, 37, 34, 35, 36, 30, 28, 27, 21 and 20). Ultimately, making the differentiation between normal architecture and subtle cortical disorganization quite difficult without accounting for the variability amongst Brodmann regions [32]. According to a prior study, the granular layers (layers II and IV) of the temporal cortex were shown to be quite variable amongst the different Brodmann subregions, with the variability decreasing towards the temporal pole (Brodmann 38) [111]. Our method of normalizing profiles across subjects and slides aimed to account for differences in layer geometry due to curvature, subject variability, and variations due to the Brodmann subregions (Figure 3.7). However, the normalization does not fully account for all of the cytoarchitectural differences seen within these subregions. Future work would benefit from analysis within location-matched subregions to account for the differences in architecture amongst the Brodmann regions.

Currently, our method is limited to cell density, size, and eccentricity features; however, the incorporation of other features that can provide additional information of the cortical architecture and may improve detection of dysplasias in future formal implementation. For example, there have been other quantitative maps described by a previous investigator that can provide additional information about the cortical architecture relevant for FCD identification, such as neuron clustering, and neuron orientation [101]. Furthermore, our research focused on features primarily related to specific cortical architecture and lamination defects related to FCD, while other features related to FCD such as the presence of radial micro-columns or density of WM neurons were not included but are vital for future studies. Additionally, the effect of sex and age were not accounted for in our study, as both age and sex can affect the density and cortical thickness as described by [112]. Further research should be done to investigate the impact of

sex, age, seizure lateralization, age of seizure onset, and other variables have when differentiating FCD pathologies. An interesting and more automated method for extracting features in the future may be to incorporate auto-encoders, instead of manually hand-crafting features. Briefly, auto-encoders can decompose sets of images to thousands of relevant features that can be used to reconstruct the original sets of images fully. The main benefit of this approach is that the decomposed features are ensured to be useful and meaningful, whereas manual feature selection is limited and often selected features are redundant as seen in our approach (Figure 3.12). Sets of the autoencoder features can then be selected to train a classifier to detect epilepsy lesions, potentially improving performance. However, this proposed solution would require a very large data set to work effectively.

Our method for detecting architectural pathologies using an anomaly detection algorithm showed promising results for future implementation as a computer-assisted diagnostic tool. Because of the time constraints and limited resources (pathologist annotation), we have not yet evaluated the sensitivity or specificity of the tool. These are essential statistical metrics, especially in the medical field, for evaluating the performance of a model in machine learning. To further improve and evaluate detection of epileptogenic lesions it would be beneficial for future work to test and validate different anomaly detection models, such as robust covariance and one-class SVM, paired with accurate pathologist annotations.

4.5 Future Directions

Significant increases in computation power and improvements to image analysis algorithms have allowed the development and advancement of computer-assisted diagnosis (CAD) approaches in radiological data. As mentioned previously, digital histology has become a common practice among pathologist and has become amenable to CAD methods and machine learning techniques. Similar to the role of CAD algorithms in medical imaging to complement radiologist opinion, CAD systems in digital histology has the potential to become a tool that can complement pathologists in disease detection, diagnosis and prognosis prediction. In particular, more automated CAD tools can complement pathologists in the detection of epilepsy lesions, ultimately reducing inter-rater variability and pathology workflow. The anticipated improved detection of epilepsy lesions with CAD systems can provide accurate ground truth information for future MRI-histology studies. For example, with the increasing demand for MRI epilepsy lesion detection tools, annotations from histology can provide ground truth annotations for validating and improving performance in-vivo, ultimately providing more accurate in-vivo diagnostic tools. Furthermore, our method for detecting anomalies in patient slides can be used to predict surgical outcomes. Specifically, the proportion of anomalies found within each patient can be used as a predictive measure of likely prognosis of patient outcome, with lower proportions indicating potentially better surgical outcomes.

Appendix A

Copyright Transfers and Reprint Permissions

SPRINGER NATURE LICENSE
TERMS AND CONDITIONS

Aug 21, 2019

This Agreement between Robarts Research Institute -- Hossein Rejali ("You") and Springer Nature ("Springer Nature") consists of your license details and the terms and conditions provided by Springer Nature and Copyright Clearance Center.

License Number	4647781475576
License date	Aug 14, 2019
Licensed Content Publisher	Springer Nature
Licensed Content Publication	Zeitschrift für die gesamte Neurologie und Psychiatrie
Licensed Content Title	Der Einflu\ der in den Furchen und Windungen auftretenden Krümmungen der Gro\hirnrinde auf die Rindenarchitektur
Licensed Content Author	S. T. Bok
Licensed Content Date	Jan 1, 1929
Licensed Content Volume	121
Licensed Content Issue	1
Type of Use	Thesis/Dissertation
Requestor type	academic/university or research institute
Format	electronic
Portion	figures/tables/illustrations
Number of figures/tables/illustrations	1
Will you be translating?	no
Circulation/distribution	<501
Author of this Springer Nature content	no
Title	A Framework for Evaluating Cortical Architectural Anomalies in Histological Temporal Lobe Epilepsy Patients
Institution name	Robarts Research Institute
Expected presentation date	Oct 2019
Portions	Sketch from Bok (1929) of a cortical cross section depicting six cytoarchitectonic layers.
Requestor Location	Robarts Research Institute 1151 Richmond Street North London, ON N6A 3K7 Canada Attn: Robarts Research Institute
Total	0.00 CAD

Terms and Conditions

Bibliography

[1] R. S. Fisher, C. Acevedo, A. Arzimanoglou, A. Bogacz, J. H. Cross, C. E. Elger, J. Engel Jr, L. Forsgren, J. A. French, M. Glynn, *et al.*, "Ilae official report: a practical clinical definition of epilepsy," *Epilepsia*, vol. 55, no. 4, pp. 475–482, 2014.

[2] R. S. Fisher, J. H. Cross, C. D'Souza, J. A. French, S. R. Haut, N. Higurashi, E. Hirsch, F. E. Jansen, L. Lagae, S. L. Moshé, *et al.*, "Instruction manual for the ilae 2017 operational classification of seizure types," *Epilepsia*, vol. 58, no. 4, pp. 531–542, 2017.

[3] I. Najm, H. Sarnat, and I. Blümcke, "The international consensus classification of focal cortical dysplasia–a critical update 2018," *Neuropathology and applied neurobiology*, vol. 44, no. 1, pp. 18–31, 2018.

[4] E. Foundation, "Epilepsy statistics," 2015.

[5] J. F. Tellez-Zenteno, M. Pondal-Sordo, S. Matijevic, and S. Wiebe, "National and regional prevalence of self-reported epilepsy in canada," *Epilepsia*, vol. 45, no. 12, pp. 1623–1629, 2004.

[6] P. Kwan and M. J. Brodie, "Early identification of refractory epilepsy," *New England Journal of Medicine*, vol. 342, no. 5, pp. 314–319, 2000.

[7] J. Engel, "Etiology as a risk factor for medically refractory epilepsy," *Neurology*, vol. 51, no. 5, pp. 1243–1244, 1998.

[8] G. A. Baker, A. Jacoby, D. Buck, C. Stalgis, and D. Monnet, "Quality of life of people with epilepsy: a european study," *Epilepsia*, vol. 38, no. 3, pp. 353–362, 1997.

[9] G. S. Bell and J. W. Sander, "Suicide and epilepsy," *Current opinion in neurology*, vol. 22, no. 2, pp. 174–178, 2009.

[10] C. L. Harden, "The co-morbidity of depression and epilepsy: epidemiology, etiology, and treatment," *Neurology*, vol. 59, no. 6 suppl 4, pp. S48–S55, 2002.

[11] A. Gaitatzis, A. L. Johnson, D. W. Chadwick, S. D. Shorvon, and J. W. Sander, "Life expectancy in people with newly diagnosed epilepsy," *Brain*, vol. 127, no. 11, pp. 2427–2432, 2004.

[12] C. E. Begley, M. Famulari, J. F. Annegers, D. R. Lairson, T. F. Reynolds, S. Coan, S. Dubinsky, M. E. Newmark, C. Leibson, E. So, *et al.*, "The cost of epilepsy in the united states: an estimate from population-based clinical and survey data," *Epilepsia*, vol. 41, no. 3, pp. 342–351, 2000.

[13] H. M. De Boer, M. Mula, and J. W. Sander, "The global burden and stigma of epilepsy," *Epilepsy & behavior*, vol. 12, no. 4, pp. 540–546, 2008.

[14] J. Engel Jr, "Introduction to temporal lobe epilepsy," *Epilepsy research*, vol. 26, no. 1, pp. 141–150, 1996.

[15] F. Rosenow and H. Lüders, "Presurgical evaluation of epilepsy," *Brain*, vol. 124, no. 9, pp. 1683–1700, 2001.

[16] J. Engel Jr, M. Levesque, and W. Shields, "Surgical treatment of the epilepsies: presurgical evaluation.," *Clinical neurosurgery*, vol. 38, p. 514, 1992.

[17] L. Tassi, N. Colombo, R. Garbelli, S. Francione, G. Lo Russo, R. Mai, F. Cardinale, M. Cossu, A. Ferrario, C. Galli, *et al.*, "Focal cortical dysplasia: neuropathological subtypes, eeg, neuroimaging and surgical outcome," *Brain*, vol. 125, no. 8, pp. 1719–1732, 2002.

[18] K. Radhakrishnan, E. L. So, P. Silbert, C. Jack, G. D. Cascino, F. Sharbrough, and P. O'brien, "Predictors of outcome of anterior temporal lobectomy for intractable epilepsy: a multivariate study," *Neurology*, vol. 51, no. 2, pp. 465–471, 1998.

[19] L. Jeha, I. Najm, W. Bingaman, F. Khandwala, P. Widdess-Walsh, H. Morris, D. Dinner, D. Nair, N. Foldvary-Schaeffer, R. Prayson, *et al.*, "Predictors of outcome after temporal lobectomy for the treatment of intractable epilepsy," *Neurology*, vol. 66, no. 12, pp. 1938–1940, 2006.

[20] A. McIntosh, S. J. Wilson, and S. F. Berkovic, "Seizure outcome after temporal lobectomy: current research practice and findings," *Epilepsia*, vol. 42, no. 10, pp. 1288–1307, 2001.

[21] J. Kiernan, "Anatomy of the temporal lobe," *Epilepsy research and treatment*, vol. 2012, 2012.

[22] H. A. Cameron and L. R. Glover, "Adult neurogenesis: beyond learning and memory," *Annual review of psychology*, vol. 66, pp. 53–81, 2015.

[23] D. L. Schacter and D. R. Addis, "The cognitive neuroscience of constructive memory: remembering the past and imagining the future," *Philosophical Transactions of the Royal Society B: Biological Sciences*, vol. 362, no. 1481, pp. 773–786, 2007.

[24] A. C. Lee, L.-K. Yeung, and M. D. Barense, "The hippocampus and visual perception," *Frontiers in human neuroscience*, vol. 6, p. 91, 2012.

[25] C. F. von Economo and G. N. Koskinas, *Die cytoarchitektonik der hirnrinde des erwachsenen menschen*. J. Springer, 1925.

[26] J. L. R. Conel, "The postnatal development of the human cerebral cortex. vol. 1. the cortex of the newborn.," 1939.

[27] A. M. Bastos, W. M. Usrey, R. A. Adams, G. R. Mangun, P. Fries, and K. J. Friston, "Canonical microcircuits for predictive coding," *Neuron*, vol. 76, no. 4, pp. 695–711, 2012.

[28] J. Nolte, "The human brain: an introduction to its functional anatomy," 2002.

[29] J. K. Mai and G. Paxinos, *The human nervous system*. Academic Press, 2011.

[30] R. E. Hogan, "Quantitative measurement of longitudinal relaxation time (qt1) mapping in tle: A marker for intracortical microstructure?," *Epilepsy currents*, vol. 17, no. 6, pp. 358–360, 2017.

[31] M. D. Sacchet and I. H. Gotlib, "Myelination of the brain in major depressive disorder: An in vivo quantitative magnetic resonance imaging study," *Scientific reports*, vol. 7, no. 1, p. 2200, 2017.

[32] F. Al Sufiani and L. C. Ang, "Neuropathology of temporal lobe epilepsy," *Epilepsy research and treatment*, vol. 2012, 2012.

[33] J. Engel Jr, "Epilepsy and seizure disorder," *Epilepsia*, vol. 46, no. 8, pp. 1333–1333, 2005.

[34] A. Palmini, F. Andermann, A. Olivier, D. Tampieri, Y. Robitaille, D. Melanson, and R. Ethier, "Neuronal migration disorders: a contribution of modern neuroimaging to the etiologic diagnosis of epilepsy," *Canadian journal of neurological sciences*, vol. 18, no. S4, pp. 580–587, 1991.

[35] S. Fauser, A. Schulze-Bonhage, J. Honegger, H. Carmona, H.-J. Huppertz, G. Pantazis, S. Rona, T. Bast, K. Strobl, B. J. Steinhoff, *et al.*, "Focal cortical dysplasias: surgical outcome in 67 patients in relation to histological subtypes and dual pathology," *Brain*, vol. 127, no. 11, pp. 2406–2418, 2004.

[36] S. Fauser, T. Bast, D.-M. Altenmüller, J. Schulte-Mönting, K. Strobl, B. J. Steinhoff, J. Zentner, and A. Schulze-Bonhage, "Factors influencing surgical outcome in patients with focal cortical dysplasia," *Journal of Neurology, Neurosurgery & Psychiatry*, vol. 79, no. 1, pp. 103–105, 2008.

[37] B. Estupinan-Diaz, L. Morales-Chacon, L. Lorigados-Pedre, I. Garcia-Maeso, J. B. Bender-del, O. Trapaga-Quincoses, L. Hidalgo-Portal, M. García-Navarro, A. Sánchez-Coroneaux, and S. Orozco-Suárez, "Pathological neocortical findings in patients with medication-resistant medial temporal lobe epilepsy submitted to surgery," *Revista de neurologia*, vol. 46, no. 4, pp. 203–209, 2008.

[38] J. Lund, "Development of the cerebral cortex: an overview," *Neurodevelopment and adult psychopathology*, pp. 3–11, 1997.

[39] J. Kabat and P. Król, "Focal cortical dysplasia–review," *Polish journal of radiology*, vol. 77, no. 2, p. 35, 2012.

[40] D. Taylor, M. Falconer, C. Bruton, and J. Corsellis, "Focal dysplasia of the cerebral cortex in epilepsy," *Journal of Neurology, Neurosurgery & Psychiatry*, vol. 34, no. 4, pp. 369–387, 1971.

[41] I. Blümcke, M. Thom, E. Aronica, D. D. Armstrong, H. V. Vinters, A. Palmini, T. S. Jacques, G. Avanzini, A. J. Barkovich, G. Battaglia, *et al.*, "The clinicopathologic spectrum of focal cortical dysplasias: A consensus classification proposed by an ad hoc task force of the ilae diagnostic methods commission 1," *Epilepsia*, vol. 52, no. 1, pp. 158–174, 2011.

[42] A. Mühlebner, R. Coras, K. Kobow, M. Feucht, T. Czech, H. Stefan, D. Weigel, M. Buchfelder, H. Holthausen, T. Pieper, *et al.*, "Neuropathologic measurements in focal cortical dysplasias: validation of the ilae 2011 classification system and diagnostic implications for mri," *Acta neuropathologica*, vol. 123, no. 2, pp. 259–272, 2012.

[43] P. Olejniczak, "Neurophysiologic basis of eeg," *Journal of clinical neurophysiology*, vol. 23, no. 3, pp. 186–189, 2006.

[44] E. Niedermeyer and F. L. da Silva, *Electroencephalography: basic principles, clinical applications, and related fields*. Lippincott Williams & Wilkins, 2005.

[45] P. L. Nunez, R. Srinivasan, *et al.*, *Electric fields of the brain: the neurophysics of EEG*. Oxford University Press, USA, 2006.

[46] C. M. Michel, M. M. Murray, G. Lantz, S. Gonzalez, L. Spinelli, and R. G. de Peralta, "Eeg source imaging," *Clinical neurophysiology*, vol. 115, no. 10, pp. 2195–2222, 2004.

[47] J. C. Henry, "Electroencephalography: basic principles, clinical applications, and related fields," *Neurology*, vol. 67, no. 11, pp. 2092–2092, 2006.

[48] D. Zumsteg and H. G. Wieser, "Presurgical evaluation: current role of invasive eeg," *Epilepsia*, vol. 41, pp. S55–S60, 2000.

[49] J. Wellmer, F. von der Groeben, U. Klarmann, C. Weber, C. E. Elger, H. Urbach, H. Clusmann, and M. von Lehe, "Risks and benefits of invasive epilepsy surgery workup with implanted subdural and depth electrodes," *Epilepsia*, vol. 53, no. 8, pp. 1322–1332, 2012.

[50] V. Chavakula and G. R. Cosgrove, "Imaging for epilepsy surgery," in *Seminars in neurology*, vol. 37, pp. 580–588, Thieme Medical Publishers, 2017.

[51] F. Bloch, "Nuclear induction," *Physical review*, vol. 70, no. 7-8, p. 460, 1946.

[52] E. M. Purcell, H. C. Torrey, and R. V. Pound, "Resonance absorption by nuclear magnetic moments in a solid," *Physical review*, vol. 69, no. 1-2, p. 37, 1946.

[53] R. Damadian, "Tumor detection by nuclear magnetic resonance," *Science*, vol. 171, no. 3976, pp. 1151–1153, 1971.

[54] R. G. Henderson, "Nuclear magnetic resonance imaging: A review1," *Journal of the Royal Society of Medicine*, vol. 76, no. 3, pp. 206–212, 1983.

[55] S. F. Berkovic, A. McIntosh, R. M. Kalnins, G. D. Jackson, G. Fabinyi, G. Brazenor, P. F. Bladin, and J. L. Hopper, "Preoperative mri predicts outcome of temporal lobectomy: an actuarial analysis," *Neurology*, vol. 45, no. 7, pp. 1358–1363, 1995.

[56] R. Mosewich, E. L. So, T. O'brien, G. D. Cascino, F. Sharbrough, W. Mars, F. Meyer, C. Jack, and P. O'Brien, "Factors predictive of the outcome of frontal lobe epilepsy surgery," *Epilepsia*, vol. 41, no. 7, pp. 843–849, 2000.

[57] P. Widdess-Walsh, L. Jeha, D. Nair, P. Kotagal, W. Bingaman, and I. Najm, "Subdural electrode analysis in focal cortical dysplasia: predictors of surgical outcome," *Neurology*, vol. 69, no. 7, pp. 660–667, 2007.

[58] L. E. Jeha, I. Najm, W. Bingaman, D. Dinner, P. Widdess-Walsh, and H. Lüders, "Surgical outcome and prognostic factors of frontal lobe epilepsy surgery," *Brain*, vol. 130, no. 2, pp. 574–584, 2007.

[59] M. Cossu, G. Lo Russo, S. Francione, R. Mai, L. Nobili, I. Sartori, L. Tassi, A. Citterio, N. Colombo, M. Bramerio, *et al.*, "Epilepsy surgery in children: results and predictors of outcome on seizures," *Epilepsia*, vol. 49, no. 1, pp. 65–72, 2008.

[60] A. A. Cohen-Gadol, C. C. Bradley, A. Williamson, J. H. Kim, M. Westerveld, R. B. Duckrow, and D. D. Spencer, "Normal magnetic resonance imaging and medial temporal lobe epilepsy: the clinical syndrome of paradoxical temporal lobe epilepsy," *Journal of neurosurgery*, vol. 102, no. 5, pp. 902–909, 2005.

[61] P. Sylaja, K. Radhakrishnan, C. Kesavadas, and P. Sarma, "Seizure outcome after anterior temporal lobectomy and its predictors in patients with apparent temporal lobe epilepsy and normal mri," *Epilepsia*, vol. 45, no. 7, pp. 803–808, 2004.

[62] S. K. Lee, S. Y. Lee, K.-K. Kim, K.-S. Hong, D.-S. Lee, and C.-K. Chung, "Surgical outcome and prognostic factors of cryptogenic neocortical epilepsy," *Annals of neurology*, vol. 58, no. 4, pp. 525–532, 2005.

[63] P. Widdess-Walsh, B. Diehl, and I. Najm, "Neuroimaging of focal cortical dysplasia," *Journal of Neuroimaging*, vol. 16, no. 3, pp. 185–196, 2006.

[64] A. Bernasconi, N. Bernasconi, B. C. Bernhardt, and D. Schrader, "Advances in mri for'cryptogenic'epilepsies," *Nature reviews neurology*, vol. 7, no. 2, p. 99, 2011.

[65] D. Cantor-Rivera, A. R. Khan, M. Goubran, S. M. Mirsattari, and T. M. Peters, "Detection of temporal lobe epilepsy using support vector machines in multi-parametric quantitative mr imaging," *Computerized Medical Imaging and Graphics*, vol. 41, pp. 14–28, 2015.

[66] K. B. Dev, P. S. Jogi, S. Niyas, S. Vinayagamani, C. Kesavadas, and J. Rajan, "Automatic detection and localization of focal cortical dysplasia lesions in mri using fully convolutional neural network," *Biomedical Signal Processing and Control*, vol. 52, pp. 218–225, 2019.

[67] O. Colliot, N. Bernasconi, N. Khalili, S. B. Antel, V. Naessens, and A. Bernasconi, "Individual voxel-based analysis of gray matter in focal cortical dysplasia," *Neuroimage*, vol. 29, no. 1, pp. 162–171, 2006.

[68] M. Strandberg, E.-M. Larsson, S. Backman, and K. Källén, "Pre-surgical epilepsy evaluation using 3t mri. do surface coils provide additional information?," *Epileptic Disorders*, vol. 10, no. 2, pp. 83–92, 2008.

[69] S. Knake, C. Triantafyllou, L. Wald, G. Wiggins, G. Kirk, P. Larsson, S. Stufflebeam, M. Foley, H. Shiraishi, A. Dale, *et al.*, "3t phased array mri improves the presurgical evaluation in focal epilepsies: a prospective study," *Neurology*, vol. 65, no. 7, pp. 1026–1031, 2005.

[70] J. Annese, "The importance of combining mri and large-scale digital histology in neuroimaging studies of brain connectivity and disease," *Frontiers in neuroinformatics*, vol. 6, p. 13, 2012.

[71] J. Engel, M. P. McDermott, S. Wiebe, J. T. Langfitt, J. M. Stern, S. Dewar, M. R. Sperling, I. Gardiner, G. Erba, I. Fried, *et al.*, "Early surgical therapy for drug-resistant temporal lobe epilepsy: a randomized trial," *Jama*, vol. 307, no. 9, pp. 922–930, 2012.

[72] A. Schulze-Bonhage and J. Zentner, "The preoperative evaluation and surgical treatment of epilepsy," *Deutsches Ärzteblatt International*, vol. 111, no. 18, p. 313, 2014.

[73] S. Wiebe, W. T. Blume, J. P. Girvin, and M. Eliasziw, "A randomized, controlled trial of surgery for temporal-lobe epilepsy," *New England Journal of Medicine*, vol. 345, no. 5, pp. 311–318, 2001.

[74] I. Georgiadis, E. Z. Kapsalaki, and K. N. Fountas, "Temporal lobe resective surgery for medically intractable epilepsy: a review of complications and side effects," *Epilepsy research and treatment*, vol. 2013, 2013.

[75] B. Fisch, "Anterior temporal lobectomy–how safe is it? anterior temporal lobectomy," *Epilepsy currents*, vol. 11, no. 6, pp. 186–188, 2011.

[76] N. FoldvarySchaefer and E. Wyllie, "Chapter 52 - epilepsy," in *Textbook of Clinical Neurology (Third Edition)* (C. G. Goetz, ed.), pp. 1213 – 1244, Philadelphia: W.B. Saunders, third edition ed., 2007.

[77] F. Al-Otaibi, S. S. Baeesa, A. G. Parrent, J. P. Girvin, and D. Steven, "Surgical techniques for the treatment of temporal lobe epilepsy," *Epilepsy research and treatment*, vol. 2012, 2012.

[78] L. Tassi, A. Meroni, F. Deleo, F. Villani, R. Mai, G. L. Russo, N. Colombo, G. Avanzini, C. Falcone, M. Bramerio, *et al.*, "Temporal lobe epilepsy: neuropathological and clinical correlations in 243 surgically treated patients," *Epileptic Disorders*, vol. 11, no. 4, pp. 281–292, 2009.

[79] T. Veuthey, G. Herrera, and V. I. Dodero, "Dyes and stains: from molecular structure to histological application," *Frontiers in Bioscience*, vol. 19, no. 1, pp. 91–112, 2014.

[80] I. Jansen, M. Lucas, C. D. Savci-Heijink, S. L. Meijer, H. A. Marquering, D. M. de Bruin, and P. J. Zondervan, "Histopathology: ditch the slides, because digital and 3d are on show," *World journal of urology*, vol. 36, no. 4, pp. 549–555, 2018.

[81] S. Chatterjee, "Artefacts in histopathology," *Journal of oral and maxillofacial pathology: JOMFP*, vol. 18, no. Suppl 1, p. S111, 2014.

[82] R. S. Desikan and A. J. Barkovich, "Malformations of cortical development," *Annals of neurology*, vol. 80, no. 6, pp. 797–810, 2016.

[83] T. Pang, R. Atefy, and V. Sheen, "Malformations of cortical development," *The neurologist*, vol. 14, no. 3, p. 181, 2008.

[84] G. Bartzokis, P. H. Lu, S. B. Stewart, B. Oluwadara, A. J. Lucas, J. Pantages, E. Pratt, J. E. Sherin, L. L. Altshuler, J. Mintz, *et al.*, "In vivo evidence of differential impact of typical and atypical antipsychotics on intracortical myelin in adults with schizophrenia," *Schizophrenia research*, vol. 113, no. 2-3, pp. 322–331, 2009.

[85] A. Schleicher, K. Amunts, S. Geyer, P. Morosan, and K. Zilles, "Observer-independent method for microstructural parcellation of cerebral cortex: a quantitative approach to cytoarchitectonics," *Neuroimage*, vol. 9, no. 1, pp. 165–177, 1999.

[86] A. Schleicher, N. Palomero-Gallagher, P. Morosan, S. Eickhoff, T. Kowalski, K. De Vos, K. Amunts, and K. Zilles, "Quantitative architectural analysis: a new approach to cortical mapping," *Anatomy and embryology*, vol. 210, no. 5-6, pp. 373–386, 2005.

[87] S. B. Eickhoff, A. Schleicher, F. Scheperjans, N. Palomero-Gallagher, and K. Zilles, "Analysis of neurotransmitter receptor distribution patterns in the cerebral cortex," *Neuroimage*, vol. 34, no. 4, pp. 1317–1330, 2007.

[88] J. Annese, A. Pitiot, I. Dinov, and A. Toga, "A myelo-architectonic method for the structural classification of cortical areas," *Neuroimage*, vol. 21, no. 1, pp. 15–26, 2004.

[89] M. Waehnert, J. Dinse, M. Weiss, M. N. Streicher, P. Waehnert, S. Geyer, R. Turner, and P.-L. Bazin, "Anatomically motivated modeling of cortical laminae," *Neuroimage*, vol. 93, pp. 210–220, 2014.

[90] S. T. Bok, "Der einfluβ der in den furchen und windungen auftretenden krümmungen der groβhirnrinde auf die rindenarchitektur," *Zeitschrift für die gesamte Neurologie und Psychiatrie*, vol. 121, no. 1, pp. 682–750, 1929.

[91] M. Dyrba, M. Ewers, M. Wegrzyn, I. Kilimann, C. Plant, A. Oswald, T. Meindl, M. Pievani, A. L. Bokde, A. Fellgiebel, *et al.*, "Combining dti and mri for the automated detection of alzheimers disease using a large european multicenter dataset," in *International Workshop on Multimodal Brain Image Analysis*, pp. 18–28, Springer, 2012.

[92] B. Magnin, L. Mesrob, S. Kinkingnéhun, M. Pélégrini-Issac, O. Colliot, M. Sarazin, B. Dubois, S. Lehéricy, and H. Benali, "Support vector machine-based classification of alzheimers disease from whole-brain anatomical mri," *Neuroradiology*, vol. 51, no. 2, pp. 73–83, 2009.

[93] M. Nieuwenhuis, N. E. van Haren, H. E. H. Pol, W. Cahn, R. S. Kahn, and H. G. Schnack, "Classification of schizophrenia patients and healthy controls from structural mri scans in two large independent samples," *Neuroimage*, vol. 61, no. 3, pp. 606–612, 2012.

[94] J. Kambeitz, L. Kambeitz-Ilankovic, S. Leucht, S. Wood, C. Davatzikos, B. Malchow, P. Falkai, and N. Koutsouleris, "Detecting neuroimaging biomarkers for schizophrenia: a meta-analysis of multivariate pattern recognition studies," *Neuropsychopharmacology*, vol. 40, no. 7, p. 1742, 2015.

[95] N. K. Focke, M. Yogarajah, M. R. Symms, O. Gruber, W. Paulus, and J. S. Duncan, "Automated mr image classification in temporal lobe epilepsy," *Neuroimage*, vol. 59, no. 1, pp. 356–362, 2012.

[96] M. A. Hall and L. A. Smith, "Practical feature subset selection for machine learning," 1998.

[97] M. QUEEN, "Some methods for classification and analysis of multivariate observations(methods for classification and analysis of multivariate observations)," 1966.

[98] M. Ester, H.-P. Kriegel, J. Sander, X. Xu, *et al.*, "A density-based algorithm for discovering clusters in large spatial databases with noise.," in *Kdd*, vol. 96, pp. 226–231, 1996.

[99] G. Karypis, E.-H. S. Han, and V. Kumar, "Chameleon: Hierarchical clustering using dynamic modeling," *Computer*, no. 8, pp. 68–75, 1999.

[100] Q. Wei, Y. Ren, R. Hou, B. Shi, J. Y. Lo, and L. Carin, "Anomaly detection for medical images based on a one-class classification," in *Medical Imaging 2018: Computer-Aided Diagnosis*, vol. 10575, p. 105751M, International Society for Optics and Photonics, 2018.

[101] C. A. Blinston, "Histological quantification in temporal lobe epilepsy," 2017.

[102] A. P. Zijdenbos, B. M. Dawant, R. A. Margolin, and A. C. Palmer, "Morphometric analysis of white matter lesions in mr images: method and validation," *IEEE transactions on medical imaging*, vol. 13, no. 4, pp. 716–724, 1994.

[103] P. Bankhead, M. B. Loughrey, J. A. Fernández, Y. Dombrowski, D. G. McArt, P. D. Dunne, S. McQuaid, R. T. Gray, L. J. Murray, H. G. Coleman, *et al.*, "Qupath: Open source software for digital pathology image analysis," *Scientific reports*, vol. 7, no. 1, p. 16878, 2017.

[104] G. Schlaug, A. Schleicher, and K. Zilles, "Quantitative analysis of the columnar arrangement of neurons in the human cingulate cortex," *Journal of Comparative Neurology*, vol. 351, no. 3, pp. 441–452, 1995.

[105] S. E. Jones, B. R. Buchbinder, and I. Aharon, "Three-dimensional mapping of cortical thickness using laplace's equation," *Human brain mapping*, vol. 11, no. 1, pp. 12–32, 2000.

[106] T. Vu and K. Laukens, "Getting your peaks in line: a review of alignment methods for nmr spectral data," *Metabolites*, vol. 3, no. 2, pp. 259–276, 2013.

[107] N.-P. V. Nielsen, J. M. Carstensen, and J. Smedsgaard, "Aligning of single and multiple wavelength chromatographic profiles for chemometric data analysis using correlation optimised warping," *Journal of chromatography A*, vol. 805, no. 1-2, pp. 17–35, 1998.

[108] M. Andres, V. M. Andre, S. Nguyen, N. Salamon, C. Cepeda, M. S. Levine, J. P. Leite, L. Neder, H. V. Vinters, and G. W. Mathern, "Human cortical dysplasia and epilepsy: an ontogenetic hypothesis based on volumetric mri and neun neuronal density and size measurements," *Cerebral Cortex*, vol. 15, no. 2, pp. 194–210, 2004.

[109] I. Blümcke, T. Pieper, E. Pauli, M. Hildebrandt, M. Kudernatsch, P. Winkler, A. Karlmeier, and H. Holthausen, "A distinct variant of focal cortical dysplasia type i characterised by magnetic resonance imaging and neuropathological examination in children with severe epilepsies," *Epileptic disorders*, vol. 12, no. 3, pp. 172–180, 2010.

[110] K. Brodmann, *Vergleichende Lokalisationslehre der Grosshirnrinde in ihren Prinzipien dargestellt auf Grund des Zellenbaues.* Barth, 1909.

[111] S.-L. Ding, G. W. Van Hoesen, M. D. Cassell, and A. Poremba, "Parcellation of human temporal polar cortex: a combined analysis of multiple cytoarchitectonic, chemoarchitectonic, and pathological markers," *Journal of Comparative Neurology*, vol. 514, no. 6, pp. 595–623, 2009.

[112] B. Pakkenberg and H. J. G. Gundersen, "Neocortical neuron number in humans: effect of sex and age," *Journal of comparative neurology*, vol. 384, no. 2, pp. 312–320, 1997.

Curriculum Vitae

Hossein Rajali

August 2019

EDUCATION

Post-secondary Education and Degrees:	**The University of Western Ontario** London, ON, Canada 2019 MESc. (Biomedical Engineering) **McMaster University** Hamilton, ON, Canada 2017 BEng - Distinction. (Electrical & Biomedical Engineering)
Honours and Awards:	**Western Graduate Research Scholarship -** (Full Tuition) The University of Western Ontario 2017-2019 **Ontario Research Grant (OGS) -** $15,000 (Canadian Dollars) The University of Western Ontario 2018-2019 **Dean's Honour List** McMaster University 2012-2017 **The University Senate Scholarship -** $800 (Canadian Dollars) McMaster University 2016 **Honor Award** McMaster University 2012
Related Work Experience	**Robarts Research Assistant** *Supervisor: Dr.Ali Khan* The University of Western Ontario, London, ON 2018-2019 **Teaching Assistant -** (Programming Fundamentals C++/Java) *Supervisor: Dr.Quazi Rahman* The University of Western Ontario, London, ON 2018-2019

Teaching Assistant - (Engineering Design and Innovation)
Supervisor: Dr.Quazi Rahman
The University of Western Ontario, London, ON
2018-2019

Research Assistant
Supervisor: Dr. Micheal Noseworthy
St.Joseph Healthcare (IRC), Hamilton, ON
2016

Related Volunteer Experience:

Brain Hack Western Organizer Member
Supervisor: Dr. Ali Khan
2018

Discover Robarts Community Presenter
Supervisor: Dr. Ali Khan
2018

Canadian Hall of Fame Presenter
Supervisor: Dr. Terry Peters
2018

Conferences & Presentation:

H.Rejali.*, Jordan DeKraker, Uzair Hussain, and Ali R. Khan "*Cortical Layer Alignment in Surgically Resected Neocortex Histology*". London Health Research Day (LHRD) - 2019
2019

H.Rejali.*, Jordan DeKraker, Uzair Hussain, and Ali R. Khan "*Cortical Layer Alignment in Surgically Resected Neocortex Histology*". Imaging Network Ontario Symposium (IMNO)- 2019

H.Rejali.*, Penny Gowland, Peter Liddle, Ali Radaideh, Lena Palaniyappan, and Ali R. Khan, *Poster: Investigating anatomical regions in which myelin abnormalities occur in schizophrenia using quantitative R1 Maps.* Clinical Neurological Science Research Day (CNS) - 2018

H.Rejali.*, Penny Gowland, Peter Liddle, Ali Radaideh, Lena Palaniyappan, and Ali R. Khan, *Poster: Investigating anatomical regions in which myelin abnormalities occur in schizophrenia using quantitative R1 Maps* Imaging Network Ontario Symposium (IMNO) - 2018